

Modulation of Zeolite Composition and Its Catalytic Effect on Methanol-to-Hydrocarbons  
Reaction

by  
Thuy Thanh Dinh Le

A dissertation submitted to the Department of Chemical and Biomolecular Engineering,  
College of Engineering  
in partial fulfillment of the requirements for the degree of

Doctor of Philosophy  
in Chemical Engineering

Chair of Committee: Dr. Jeffrey D. Rimer

Committee Member: Dr. Michael P. Harold

Committee Member: Dr. Lars C. Grabow

Committee Member: Dr. Allan J. Jacobson

Committee Member: Dr. Bert M. Weckhuysen

University of Houston  
December 2020

Copyright 2020, Thuy Thanh Dinh Le

## ACKNOWLEDGMENTS

I would like to thank my advisor Dr. Jeffrey D. Rimer for his guidance and endless support of my career goal over the past five years. He has given me countless opportunities to expand my skillset and allowed me to collaborate with various world-class researchers. As a result, I am able to incorporate highly diverse and collaborative works in my dissertation. I would also like to thank my committee members for evaluating my work.

I am especially appreciative of my collaborators who help enhance the quality of my research. The collaborative experience has been an integral and invaluable part of my graduate career.

In addition, I would like to thank my group members at the University of Houston. I would especially like to Dr. Yufeng Shen, who was my mentor for my first two years, our catalysis subgroup members for their interesting research discussion and valuable feedbacks on my work, and Dr. Aseem Chawla and Dr. Madhuresh Choudhary for a wide range of interesting office conversation.

Lastly, I would like to thank my family for their unyielding support which comes in the form of delicious food.

## ABSTRACT

Zeolites, with their diverse framework topology and tunable acidity, are highly utilized as commercial catalysts with one of the most popular applications being the production of hydrocarbons from methanol (MTH). Although MTH is a commercial reaction, there are various mechanistic aspects that are not fully understood, and ongoing efforts are focused on ways to improve catalyst performance and establish fundamental understandings of structure-performance relationships. One of the critical challenges in this area of research is the inherent complexity of zeolite synthesis, which can result in catalysts with a range of compositions, morphologies, and defects. This dissertation aims to better correlate the physicochemical properties of zeolites with their catalytic performance through the development of characteristic descriptors and elucidating the effect of compositional (acid site) gradients using MTH as a benchmark reaction.

We first investigated the introduction of defects that occurs during zeolite ZSM-5 crystallization as a result of complex nonclassical crystallization mechanisms using time-resolved dissolution studies coupled with *ex situ* electron and scanning probe microscopy. Our findings reveal that ZSM-5 (**MFI** framework) undergoes multiple stages of growth (both classical and nonclassical), which can lead to catalysts with a high concentration of crystalline defects. These defects can affect mass transport properties of zeolites and consequentially catalytic performance. To quantitatively assess the impact of mass transport limitations in zeolites, we investigated the use of experimentally obtained diffusional timescales to account for the effect of diffusional

constraints, imposed by crystallite size and defects, on catalytic lifetime in MTH reaction for three zeolites/zeotypes: ZSM-5 (MFI), ZSM-11 (MEL), and SAPO-34 (CHA).

Lastly, using the developed descriptors, we focused on elucidating the impact of mesoscopic compositional gradients within zeolite catalysts on MTH catalyst performance. In recent years, improvements in the design and optimization of zeolite catalysts have shifted toward modulation of elemental composition, including the characterization and understanding of acid site speciation and distribution within zeolite particles; however, mesoscopic compositional gradients within zeolite catalysts is often overlooked. Here, we reported a one-pot synthesis of ZSM-5 with compositional gradient (i.e., zoning) and investigated its performance in MTH. We demonstrated that Si-zoned ZSM-5 exhibits improved lifetime in comparison to its homogeneous counterpart due to the reduction of diffusion limitations and the suppression of external coking as a result of its siliceous (passivated) exterior. We further expanded this study to determine the effect of siliceous shell thickness in core-shell zeolite catalysts (i.e., zoning analogues), which show similar improvement in lifetime, albeit with different trends in selectivity. Our findings suggest that there are distinct differences at the exterior-interior interface for zoned and core-shell catalysts that can influence mass transport properties and impact product selectivity.

# TABLE OF CONTENTS

<b>Acknowledgments</b> .....	<b>iii</b>
<b>Abstract</b> .....	<b>iv</b>
<b>Table of Contents</b> .....	<b>vi</b>
<b>List of Tables</b> .....	<b>viii</b>
<b>List of Figures</b> .....	<b>ix</b>
<b>Chapter 1</b> .....	<b>1</b>
1.1 Zeolite crystal size – Reduction of mass transport limitations .....	2
1.2 Aluminum siting and speciation.....	6
1.2.1 Framework aluminum siting .....	7
1.2.2 Framework-associated and extra-framework aluminum.....	18
1.3. Elemental zoning and core-shell analogues .....	25
1.5 Dissertation Outline .....	36
<b>Chapter 2</b> .....	<b>37</b>
2.1 Motivation .....	37
2.2 Experimental Methods .....	40
2.2.1 MFI Zeolite Synthesis and Dissolution Treatment .....	40
2.2.2 Characterization .....	41
2.3 Results and Discussion.....	46
2.4 Summary .....	59
<b>Chapter 3</b> .....	<b>61</b>
3.1 Prior Work on Establishing Structure-Performance Relationship for Zeolites in MTH.....	61
3.2 Motivation .....	64
3.3 Experimental Methods .....	67
3.3.1 Materials.....	67
3.3.2 Synthesis and catalyst preparation of ZSM-5 zeolites .....	68
3.3.3 Time-elapsd study of synthesis .....	70
3.3.4 Characterization of ZSM-5 zeolites .....	70
3.3.5 Characterization of zoning in ZSM-5 zeolites .....	71
3.3.6 Characterization of Al gradient in ZSM-5 zeolites .....	71
3.3.7 Measurement of shell thickness for zoning analogues.....	72
3.3.8 Characterization of Al species and acid sites .....	73

3.3.9 Reaction testing.....	74
3.3.10 Operando UV-vis spectroscopy with on-line gas chromatography	75
3.4 Results and Discussion.....	77
3.4.1 Synthesis of Zoned ZSM-5 Crystals .....	77
3.4.2 Comparison of Catalyst Performance .....	82
3.4.3 Deactivation Mechanism of H-ZSM-5 Catalysts.....	87
3.4.4 Analogues of Zoned ZSM-5 .....	91
3.5 Summary .....	93
<b>Chapter 4 .....</b>	<b>95</b>
4.1 Motivation.....	95
4.2 Experimental Methods .....	97
4.2.1 Materials.....	97
4.2.2 Synthesis and catalyst preparation of core-shell ZSM-11 .....	97
4.2.3 Characterization of ZSM-11 zeolites .....	98
4.2.4 Characterization of core and shell composition in ZSM-11 zeolites	99
4.2.5 Characterization of Al gradient in ZSM-11 zeolites.....	99
4.2.6 Characterization of Al species and acid sites .....	100
4.2.7 Reaction testing.....	101
4.3 Results and discussion .....	103
<b>Chapter 5 .....</b>	<b>112</b>
5.1 Current Research Summary .....	112
5.2 Future Outlook .....	114
5.2.1 Zeolite secondary growth.....	114
5.2.2 Bifunctional zeolite catalysts .....	115
<b>References.....</b>	<b>120</b>
<b>Appendix A Supplementary Information for Chapter 2.....</b>	<b>155</b>
<b>Appendix B Supplementary Information for Chapter 3.....</b>	<b>161</b>
<b>Appendix C Supplementary Information for Chapter 4.....</b>	<b>177</b>

## LIST OF TABLES

Table 3.1 Physicochemical properties of H-ZSM-5 samples selected for catalyst testing .....	81
Table 4.1 Physicochemical properties of H-ZSM-11 catalysts.....	103
Table B1 Synthesis conditions and properties of ZSM-5 from an OSDA-based protocol .....	161
Table B2 Properties of ZSM-5 from an OSDA-free method where Na <sup>+</sup> is replaced with TPA <sup>+</sup> .....	162
Table B3 Properties of ZSM-5 from an OSDA-free method where NaOH is replaced with TPAOH and amount of alkali metal is replenished with NaCl or KCl salt .....	162
Table B4 Synthesis conditions and properties of selected ZSM-5 samples for catalysis study .....	163
Table B5 Summary of R <sup>2</sup> /D, turnover numbers, and E/2MBu ratios .....	164
Table B6 Summary of local maxima (in wavenumbers) in each UV-vis spectral region for all samples. Specific association of species with wavelengths is summarized by Fu et al., [1] .....	164

## LIST OF FIGURES

Figure 1.1 Examples of synthesized zeolites with reduced diffusion pathlengths and enhanced mass transports. Adapted from [2-7] .....	4
Figure 1.2 (a) Scheme of Al in <b>CHA</b> [8]. (b) Scheme of different Al siting in ZSM-5 channels and intersection [9]. (c) Effects of Al source on the proportion of paired Al sites ZSM-5 [10]. (d) Cobalt ion exchange isotherms for SSZ-13 [11]. (e) Schemes of unpaired and paired Al [10] .....	11
Figure 1.3 (a) Pathways for cracking of 1-hexene in ZSM-5 [12]. (b) Impact of Al proximity on the cracking of 1-hexene over ZSM-5 [13]. (c) 0 <sup>th</sup> (circles) and 1 <sup>st</sup> rate constants (squares) for MeOH dehydration increase with increased proportion of paired Al sites in the <b>CHA</b> [14] .....	15
Figure 1.4 Variation of the transition-state Gibbs free energy for four distinct Al sitings .....	17
Figure 1.5 Scheme of EFAl and FAI site proximity in ZSM-5 framework to demonstrate Brønsted/Lewis acid synergy. (b) Al DQ-MAS NMR spectra of parent H-ZSM-5 (left) and dealuminated H-ZSM-5 (right). Adapted from [15] .....	22
Figure 1.6 (a) Isobutane cracking rate constants as a function of Na <sup>+</sup> titrated sites-to-total Al ratio for HUSY [16]. (b) Conversion and selectivity for glucose isomerization reaction of Y zeolites with different tri-coordinated EFAl. Adapted from [17] .....	23
Figure 1.7 (a) Scheme of Al-zoning and Si-zoning. (b) Elemental mapping in ZSM-5 using SEM-EDX [18]. (c) Cross-sectional EDX mapping of Al-zoned ZSM-5 [19]. (d) Percentages of Al and Si in a Si-zoned ZSM-5 crystal (inset) from XPS and Ar <sup>+</sup> sputtering [20] .....	27
Figure 1.8 (a) Xylene yields and p-xylene selectivity (open and closed symbols) for methanol to aromatics reactions. (b) Coke amounts as a function of time on stream [21]. (c) EDX mapping, (d) HRTEM image and SAED pattern of ZSM-5@silicalite-1 [22] .....	32
Scheme 1.1 Proposed reaction pathways. Species A and E are methyl acetate and acetic acid from the proposed Koch carbonylation pathways. Adsorbed species F and G initiate formation of C <sub>2</sub> -C <sub>4</sub> olefins, leading to the autocatalytic mechanism. Z-H denotes the zeolite [23] .....	35
Figure 2.1 Scanning electron micrographs of (a) parent crystals; (b) after 30 min dissolution; (c, d) after 60 min treatment; (e, f) after 120 min treatment .....	47
Figure 2.2 (a – c) Time-elapsd images (10 – 40 min of treatment). (c) 3D rendering of overlapping height and amplitude images. (d) Height profiles along the green lines (data are normalized to the baseline). (e – j) Height images of a different surface (5 – 60 min of treatment) .....	49
Figure 2.3 Dissolution uncovers the history of ZSM-5 (a, b, c) and silicalite-1 (d, e, f) crystallization .....	50

Figure 2.4 (a, b) HRTEM images down the <i>c</i> -axis from a foil from the periphery (I) and the central part (II) of the crystal. (c, f) FFTs from the lattice images in (I) and (II), marked (020) reflections. (d,e) Low magnification TEM dark-field image from the foil (I) and (II).....	52
Figure 2.5 (a – d) AFM height images of a fixed area on a silicalite-1 (010) surface (10 – 25 min treatment), (g – l) another area (10 – 60 min treatment) (e) Height profiles of a feature in AFM. (f) A distribution of spheroidal feature diameters (n = 17 measurements).....	54
Figure 2.6 Interpreted scheme of (a) 2 steps incubation process: (1) formation of proto-particles with MFI structure; (2) fusion to form nuclei. (b) The growth process has 3 distinct stages: (1) skeletal growth, (2) sectorial growth, and (3) final zonal overgrowth .....	57
Figure 3.1 (a) Plot showing the apparent correlation between the characteristic diffusion timescale $D/R^2$ and catalyst lifetime. The dashed line is interpolated to guide the eye [24]. (b) Total turnovers versus a descriptor that accounts for diffusional constraints [25]. .....	63
Figure 3.2 (a) Idealized depiction of Al- and Si-zoning in zeolite ZSM-5. (b) Ratio of $Al_{\text{surface}}/Al_{\text{bulk}}$ as a function of organic SDA fraction ( $TPA^+$ ) in the growth mixture. Compositions of each sample are provided in Tables B1, B2, and B3 .....	78
Figure 3.3 SEM images of (a) Al-zoned sample A-4, (b and c) homogeneous samples H1-3 and H2-6, and (d – f) Si-zoned samples S1-1, S2-1, and S3-2. All syntheses were performed at 190°C, with the exception of sample A-4 (100°C).....	79
Figure 3.4 (a) Raw VKE-XPS spectra for sample S2-1 for other samples (Figures B11 and B12). (b) Si/Al from XPS depth analysis for 5 samples. (c) Parity plot in log scale of $R_E$ against $R_A$ . (d) Conversion of MeOH and DME versus cumulative turnovers....	83
Figure 3.5 (a) Turnover number for H-ZSM-5 catalysts calculated from conversion vs. time on stream data (Figure B14) and (b) $E/2MBu$ as function of the descriptor $R_E C_{H^+} S_A^{-1}$ . Zoned trend line is qualitatively consistent with that reported in literature (Figure B13).....	86
Figure 3.6 (a) UV-Vis bands corresponding to species during the MTH reaction [1]. (b) Operando UV-Vis spectra of selected samples. Changes of the intensity ratio of (c) internal coke-to-HP species as a function of TOS and (d) of the intensity ratio of external-to-internal coke species.....	87
Figure 3.7 (a) Spectra in the range of 3900-3400 $cm^{-1}$ for H-form samples before pyridine adsorption. (b) Spectra in the range of 1600-1400 $cm^{-1}$ after pyridine adsorption .....	90
Figure 3.8 (a) Illustrations of core-shell (left) and inverse core-shell (right) catalysts with thin (10 – 15 nm) shells. (b) Conversion of MeOH and DME as a function of cumulative turnovers. (c) Comparison of turnover number (TON, left y-axis) and $E/2MBu$ ratio (right y-axis).....	92

Figure 4.1 (a) Scheme of a ZSM-11@silicalite-2 core-shell particle. (b-f) Scanning electron micrographs of the (b) core C-30, (c) core-shell CS-60, (d) core-shell CS-91, (e) core-shell C-133, and (f) homogeneous ZSM-11 H-60. Scale bars equal 200 nm. ....	104
Figure 4.2 Comparison of Si/Al from XPS depth analysis (VKE-XPS) as a function of photon energy (bottom x-axis) and corresponding information depth (top x-axis). ...	106
Figure 4.3 (a) Fractional conversion of MeOH and DME plotted as a function of time-on-stream $t$ . (b) Initial conversion (at $t = 20$ min) plotted as a function of contact time $\tau$ ( $\text{s mol}_{\text{H}^+} \text{mol}_{\text{C}}^{-1}$ ).....	107
Figure 4.4 Initial E/2MB at sub-conversion for MTH reactions over H-ZSM-11 plotted as a function of descriptor $C_{\text{H}^+} S_{\text{A}}^{-1} R^2 / D$ . Green side triangles marked data of homogeneous and zoned ZSM-5 in Chapter 3. Light yellow shaded area highlights general trend.....	109
Figure A1 Powder XRD pattern of ZSM-5 (MFI framework) synthesized in a fluoride medium.....	155
Figure A2 Scanning electron micrograph of representative ZSM-5 crystals synthesized in a fluoride medium .....	155
Figure A3 Nitrogen adsorption-desorption isotherm of ZSM-5 .....	156
Figure A4 Merged AFM height images of a silicalite-1 sample treated <i>ex situ</i> in 40 wt% $\text{NH}_4\text{F}$ solution for up to 60 min (shown here in 5 min intervals) .....	156
Figure A5 AFM height images of an MFI crystal after 10 min of treatment used as a template to mark areas of analyses of figures in the main text .....	157
Figure A6 Scanning electron micrograph of a ZSM-5 crystal after $\text{NH}_4\text{F}$ etching for 60 min .....	157
Figure A7 Histogram of measured widths of etch pits ( $n = 50$ measurements) over two different crystals. Widths listed in the $x$ -axis are median values .....	158
Figure A8 Corresponding amplitude images of Figure 5g-l in the main text. The circle (labelled <i>i</i> ) highlights a fixed area where the topography alternates. The dashed lines (labelled <i>ii</i> ) highlight a crevice .....	158
Figure A9 Chemical mapping of surface of two crystals from ToF-SIMS for parent MFI (a-d) and the acid-treated sample (e-h). Total chemical images (a and e), and mapping of (b and f) $\text{C}_3\text{H}_8\text{N}^+$ , fragment of TPA ion, (c and g) $\text{SiO}^+$ , (d-h) $\text{Si}_2\text{OH}^+$ .....	159
Figure A10 TEM imaging of a thin FIB lamellae cut of an untreated ZSM-5 crystal. (a) FI-FFT image from the [001] FFT pattern (c, central part), and (b) from the [001] FFT pattern image shown in d, peripheral part.....	159
Scheme A1 (left) Atomic force microscopy (AFM) images of an entire MFI (010) crystal surface (ca. $14 \mu\text{m}$ in length) compiled from the merging and overlapping of individual scans (size $2 \times 2 \mu\text{m}^2$ ) .....	160

Scheme A2 Scheme illustrating AFM tip geometry effect. The geometric factor is accounted for in diameter measurements of spheroidal features ( <b>Figure 2.5f</b> ). Adapted from [26] .....	160
Figure B1 Powder XRD patterns for the set of samples shown in Table B1. The patterns for all samples display typical peaks indicative of the MFI framework .....	165
Figure B2 XRD patterns for the set of samples shown in Table B2. The patterns for all samples display typical peaks indicative of the MFI framework.....	166
Figure B3 XRD patterns for the set of samples shown in Table B2. The patterns for all samples display typical peaks indicative of the MFI framework.....	167
Figure B4 Si and Al concentration in the supernatant, analyzed with ICP-MS, as a function of time for homogeneous sample (H1-3, purple circles) and Si-zoned sample (S2-1, red inverted triangles). Error bars span two standard deviations .....	168
Figure B5 (a) XRD patterns of homogeneous sample synthesized with mixed SDAs (H1-3) and of (b) a Si-zone sample (S2-1) after 3, 6, 12, and 24 h of synthesis. The patterns display typical MFI peaks, except for S2-1 - 3h which shows partially amorphous phase.....	169
Figure B6 SEM micrographs of (a – d) homogeneous sample (H1-3) and (e – h) Si-zone sample (S2-1) collected from time-elapsd study after 3, 6, 12, and 24 h.....	170
Figure B7 Results of transient sorption of 2,3-dimethylbutane, plotted as the normalized adsorption with respect to time. The experimental curves are shown with red circles, and the weighted curves are shown in blue.....	170
Figure B8 Physisorption curves plotted as quantity of N <sub>2</sub> adsorbed/desorbed versus relative pressure for samples A-4 to S3-2 listed in Table 3.1 .....	171
Figure B9 NH <sub>3</sub> – TPD curves plotted as TCD concentration versus desorption temperature for (a) Al-zoned sample (blue), homogeneous sample from an inorganic synthesis (dark purple), and homogeneous sample from mixed SDAs (lavender); (b) Si-zoned samples .....	171
Figure B10 <sup>27</sup> Al MAS NMR spectra for H-ZSM-5 catalyst samples with Al-zoning (A-4), Si-zoning (S1-1, S2-1, and S3-2), and homogeneous Al distribution (H1-3, H2-6) .....	172
Figure B11 Raw VKE-XPS spectra for (a) sample A-4 and (b) H1-3. The binding energy (E <sub>B</sub> , x-axis) is plotted relative to the binding energy of spectra collected at a photon energy of 3003 eV .....	172
Figure B12 Raw VKE-XPS spectra for (a) sample S1-1, (b) sample S3-2. The binding energy (E <sub>B</sub> , x-axis) is plotted relative to the binding energy of spectra collected at a photon energy of 3003 eV.....	173
Figure B13 Ethene (filled symbols) and 2MBu (open symbols) selectivities as a function of a descriptor (N <sub>H+</sub> ), which is a ratio of crystallite size (from 2,2-dimethylbutane	

adsorption uptake measurements) and the Si/Al ratio. Figure taken from Figure S4 of reference [27] .....	174
Figure B14 Conversion of MeOH and DME as a function of TOS for the Al-zoned (blue), homogeneous (purple), and Si-zoned samples (red). All reactions were performed at 350 °C using a space velocity of 0.18 - 0.30 mol MeOH mol <sup>-1</sup> H <sup>+</sup> s <sup>-1</sup> ..	174
Figure B15 UV-vis spectra collected under operando condition for methanol-to-hydrocarbon reaction.....	175
Figure B16 (a) Temporal changes of the intensity ratio of internal coke species (416-425 nm) to HP species 350-375 nm) for Si-zoned sample S3-2. (b) Corresponding changes of the intensity ratio of external coke species (560-575 nm) to internal coke species .....	175
Figure B17 SEM images of the homogeneous ZSM-5 core (C-0.2), ZSM-5@silicalite-1 core-shell (CS-0.2), and inverse core-shell silicalite-1@ZSM-5 (ES-0.3) samples.	176
Figure B18 Physisorption curves plotted as quantity of N <sub>2</sub> adsorbed/desorbed versus relative pressure for samples C-0.2, CS-0.2, and ES-0.3 listed in Table 3.1 .....	176
Figure C1 Physisorption curves plotted as quantity of N <sub>2</sub> adsorbed/desorbed versus relative pressure for all samples listed in Table 4.1 .....	177
Figure C2 Spectra in the range of 3800-3300 cm <sup>-1</sup> for H-form samples before pyridine adsorption.....	177
Figure C3 Results of transient sorption of 2,3-dimethylbutane, plotted as the normalized adsorption with respect to time. The experimental curves are shown with red circles, and the fitted curves are shown in blue.....	178
Figure C4 Initial effluent hydrocarbon selectivity (left axis) and ethene/2MBu (black circles, right axis) at iso-conversion (39-61%) for methanol-to-hydrocarbons reactions over H-ZSM-11 catalysts at 350 °C and P <sub>MeOH</sub> = 11.5 kPa .....	178

## CHAPTER 1

Synthetic zeolites are crystalline nanoporous aluminosilicates with a variety of pore sizes (0.3 to 0.8 nm), dimensions (1D, 2D, and 3D), compositions (Si, Al, and other heteroatoms), and active sites for heterogeneous catalysis (Brønsted and Lewis acids). There are more than 240 known zeolite structures according to the International Zeolites Association (IZA). The high thermal stability, tunable acidity, and shape selectivity of zeolite catalysts make them ideal candidates for commercial catalytic processes [28]; however, there are ca. 20 zeolites used as commercial catalysts (with less than 10 used in large quantity) owing to factors associated with the cost and complexity of large-scale synthesis [29]. Typical challenges of these syntheses include low yield, the required use of expensive organics, post-synthesis aggregation, and issues with scale up [30]. A survey of zeolite literature shows that changes in synthesis conditions can have a significant impact on the properties of zeolite crystals. These parameters include (but are not limited to) the selection of silicon and aluminum sources, the use of inorganic and/or organic structure-directing agents (SDAs), reaction temperature, and the molar composition of reagents. Despite its long history, zeolite synthesis remains more of an art than a science, with synthesis guidelines informed by a variety of trends derived from literature or empirically determined through experimentation. As such, there are continual efforts from multiple groups to propel the field toward scientific understanding. To this end, this active area of research presents many opportunities to develop new synthesis methods and elucidate structure-property relationships.

## 1.1 Zeolite crystal size – Reduction of mass transport limitations

A majority of zeolite studies has focused on a common objective of reducing mass transport limitations, which is a nontrivial task given the complexity of zeolite crystallization [31] and that fewer than 20 framework types have been synthesized as isolated crystallites with sizes less than 100 nm [32]. This objective can be achieved through the design of either nano-sized or hierarchical materials using a range of (post-) synthesis approaches to reduce the internal diffusion path length [5, 33-41].

One method to produce relatively monodisperse zeolite crystals is hard templating. Colloidal crystal templating is utilized to synthesize 3-dimensional ordered macroporous/mesoporous (3Dom) materials, also known as inverse opals. Design strategies for a range of 3Dom materials and their use in catalytic applications is highlighted in a review article by Stein [42]. Challenges in 3Dom synthesis involve defect minimization, morphology control, and the identification of templates that can be removed efficiently and/or supplement additional functionality. The interconnected network of pores and adaptable functionalization of 3Dom materials make them attractive structures for catalytic applications. Tsapatsis and coworkers used this approach to synthesize uniform silicalite-1 (MFI) crystals with tunable size (< 50 nm) in carbon templates (**Figure 1.1a**) [36]. This approach has been used by others to synthesize a broader set of zeolite structures, which have been tested in a range of catalytic reactions [2, 43].

A versatile method to tailor the anisotropic rates of zeolite crystallization is through the use of growth modifiers (ZGMs), which are economically beneficial in that they can

be recovered and potentially recycled. Rimer and coworkers introduced ZGMs [44] by posing a classical mode of action wherein modifiers bind to sites (kinks, steps, terraces) on specific crystal surfaces and impede the addition of solute to adjacent sites; however, the fact that zeolites grow via a combination of classical (i.e., monomer-by-monomer addition) and nonclassical pathways involving a wide variety of precursors calls into question the exact role(s) of ZGMs in zeolite nucleation and growth [45]. Rimer [3, 34, 46] and others [47-50] have demonstrated the impact of modifiers on a range of zeolite frameworks that include **LTL**, **MFI**, **MOR**, **MTW**, **TON**, and **CHA**. Studies of silicalite-1 (**MFI**) revealed that polyamines reduce the [010] dimension of crystals, which is the principal direction for internal diffusion [34]. Effective modifiers of **LTL** include alcohols, which are capable of reducing the diffusion path length by more than a factor of three (**Figure 1.1b, c**) [3]. Studies of **CHA** (SSZ-13) reveal that ZGMs operate as colloidal stabilizers to either suppress or promote the aggregation of amorphous precursors, thus allowing for crystal size to be selectively tuned over three orders of magnitude (0.1 – 10  $\mu\text{m}$ ) [46]. A general rule of thumb for selecting modifiers in crystallization is that macromolecules, such as polymers, tend to be more effective than smaller molecules (e.g., their respective monomers).

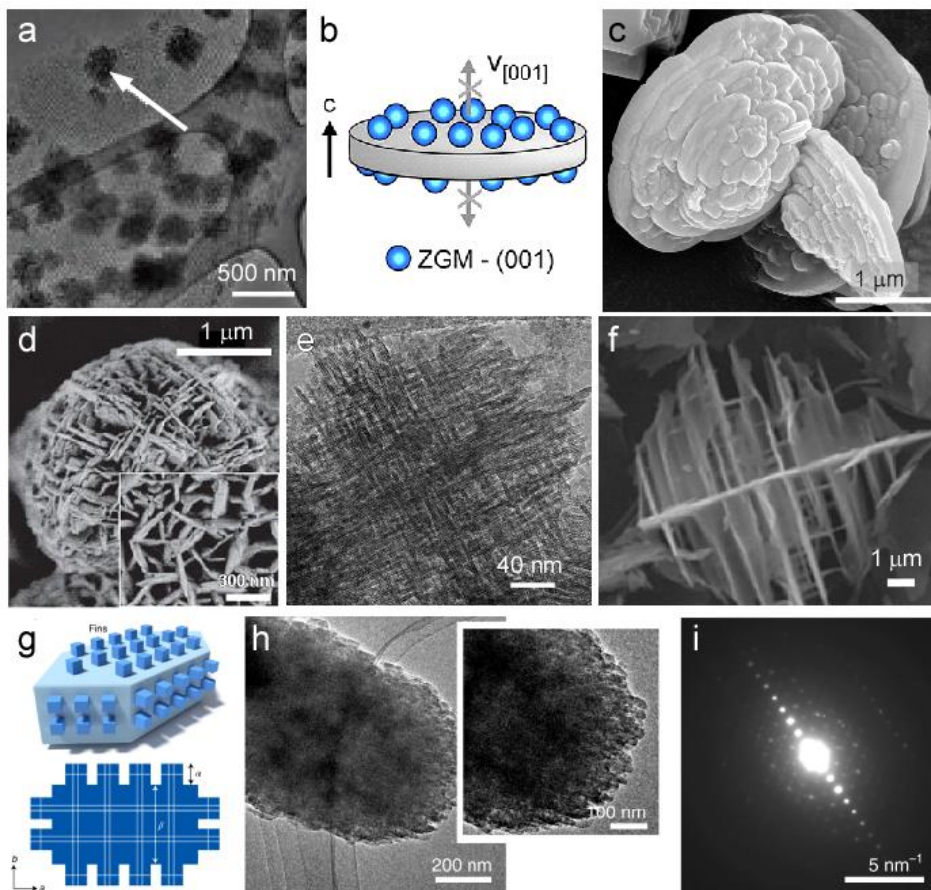


**Figure 1.1.** Examples of synthesized zeolites with reduced diffusion pathlengths and enhanced mass transports. Adapted from [2-7].

The most common use of organics in zeolite synthesis is as SDAs, which are molecules with a size and shape that is commensurate with the geometry of zeolite channels/pores. SDAs facilitate the formation of pores to which they are occluded during crystallization. In addition to directing the formation of the crystal structure, organic SDAs can also have a significant impact on crystal morphology [51, 52]. Ryoo and coworkers [4] introduced the use of surfactant-like SDAs (e.g., di- and triquaternary ammonium-type surfactants) to generate unilamellar ZSM-5 comprised of randomly-stacked 2-dimensional (2D) nanosheets that exhibit mesoporosity (**Figure 1.1d**). Novel

SDAs have been used by Ryoo and others to generate a wide range of 2D zeolite structures (e.g., **MFI**, **MWW**, **BEA**, **MTW**, and **MRE**) [4, 53, 54]. It has been shown that phosphonium-based SDAs and molecular analogues of tetrapropylammonium, a common SDA for zeolite **MFI**, can generate **MFI**-type crystals as self-pillared nanosheets with mesoporosity (**Figure 1.1e**) [5], crystals with sequential intergrowths (**Figure 1.1f**) [38], and other unique morphologies with reduced internal diffusion path length [55]. There has been a recent surge in research efforts to design 2D materials; however, this topic dates back 30 years beginning with the delamination of layered zeolites. Materials such as **MWW** (or MCM-22, ERB-1, UCB-1) [56, 57] can be delaminated to thin sheets of ca. 2.5nm thickness with extremely high external surface area. This process involves the swelling of layers with an organic (e.g., surfactant) followed by sonication to disperse individual sheets. Recently, Rimer and coworkers developed a one-pot synthesis of **MWW** nanosheets (bypassing the need for post-synthesis delamination) using a commercial surfactant (cetyltrimethylammonium, CTA<sup>+</sup>) [58]. Zeolite nanosheets have been demonstrated to exhibit higher selectivity [59] and markedly longer lifetime [4] than their commercial analogues. Prior studies have shown that unilamellar ZSM-5 can be exfoliated into single sheets via a top down approach [60] using a similar methodology as **MWW**. In addition, a study of siliceous **MFI** (silicalite-1) introduced a bottom up approach to generate 2D nanosheets using ca. 30nm **MFI** seeds in the presence of bis 1,5 (tripropyl ammonium) pentamethylene diiodide as the SDA [61]. More recently, Rimer and coworkers have demonstrated a facile method to generate nano-crystallite domains (< 50 nm) to overcome diffusion

limitation. Through secondary growth of ZSM-5 and ZSM-11 nano-crystallites (< 50 nm) on seeds of corresponding frameworks, we were able to produce finned zeolite catalysts with improved diffusion and accessibility (**Figure 1.1g - i**) [7].

## **1.2 Aluminum siting and speciation**

There has been resurgent interest in characterizing and controlling the spatial distribution of acid sites in zeolites. One of the limiting factors of large-scale zeolite synthesis is control over aluminum incorporation, including the number, spatial location at distinct crystallographic sites, mesoscopic gradients in distribution, and speciation (or local coordination) of acid sites. The synthesis of zeolites with controlled Al density and siting often necessitates the use of organic structure-directing agents (OSDAs). In the absence of OSDAs, the majority of syntheses produce zeolites with excessively high Al content (i.e., low Si/Al ratio), which compromises hydrothermal stability. Increasing the Si/Al ratio to optimal levels for catalysis often requires OSDAs, which can have negative economic and environmental impacts [62]. Many computational and experimental studies have focused on understanding (or controlling) Al incorporation, including the ability to tailor the spatial distribution and types of active sites.

Direct synthesis or post-synthesis modifications to zeolites can result in a wide array of aluminum species. Brønsted acids sites are typically associated with framework Al sites (i.e., tetrahedral coordination); however, these species can be distorted within the framework or exhibit alternative coordination numbers (e.g., penta-coordination). Moreover, extra-framework Al species (e.g., octahedral coordination) can act as Lewis acids and impose additional mass transport restrictions and confinement effects,

whereas combinations of framework and extra-framework species can act in tandem in bifunctional catalysis. Here, we summarize the various types of Al siting and speciation and discuss how these sites influence catalytic performance. The following subsections will focus at the microscopic level to discuss framework Al siting and the range of Al speciation that can exist within a zeolite crystal, and to establish the difference between siting and mesoscopic compositional gradients known as zoning.

### **1.2.1 Framework aluminum siting**

The trajectory of zeolite catalyst design has shifted over the past decades from the macroscopic level, where emphasis has been placed on controlling properties such as crystal size [63] and morphology [64], to the microscopic (or atomic) level, where biased insertion of Al at specific tetrahedral sites has emerged as an area of significant interest in heterogeneous catalysis [65]. Advancements in this area are the result of rapid progress in high precision synthesis [11], development of computation models [66] to validate and/or guide experiments, and the use of state-of-the-art characterization methods to investigate Al siting and proximity. Early studies probing the impact of aluminum content on zeolite catalysis proposed that protons compensating Al atoms located at different lattice sites behave similarly in catalytic reactions, thereby suggesting that zeolites catalyze reactions predominantly by their shape selective properties [67]. One subject that is widely debated is the degree to which intrinsic Brønsted acid strength differs among discrete tetrahedral (T) sites. Zeolites can broadly be categorized as having either identical or distinctly different T sites. Differences in experimentally measured  $\text{NH}_3$  adsorption enthalpies or calculated O-H stretching

frequencies are often used as indicators of acid strength [68]. It has been proposed that intrinsic acid strength is independent of Al siting, and cannot be inferred from adsorption measurements with probe molecules owing to contributions of H-bonding and van der Waals (vdW) interactions. Several groups have employed density functional theory (DFT) calculations (cluster models or periodic structures) to estimate Brønsted acid strength using the deprotonation energy (DPE). Iglesia and coworkers [69] have examined DPE for six different zeolite structures with varying T site locations and showed a spread of 20 kJ/mol. Hibbitts and coworkers [70] expanded these studies to examine paired Al sites in SSZ-13 (**CHA**), calculating differences in DPE values >20 kJ/mol depending on paired combinations. Alternatively, Grabow and coworkers [71] examined O-H vibrational frequencies for all twelve T sites in ZSM-5 (**MFI**) and showed three distinct regimes, suggesting differences in acidity. While all of these studies do not definitively assess intrinsic activity, the majority indicate differences among T sites. The argument that Al acid strength is equivalent independent of siting is based on the assumption that vdW interactions are dominant, which is backed by DFT calculations showing that vdW contributions as a result of confinement are significant (>> 20 kJ/mol). For example, DFT analysis of probe molecule adsorption (CO, NH<sub>3</sub>, CH<sub>4</sub>, and pyridine) on ZSM-5 revealed a strong influence of vdW interactions [66]. A theoretical study by Corma and coworkers [72] using similar probe molecules to assess interaction energies on distinct T sites of **MFI** and mordenite (**MOR**) frameworks also implied that confinement can substantially impact experimental measurements of Brønsted acidity. In view of these collective findings, it is apparent that Brønsted acid

strength among different T sites is not equivalent, but their relative contribution to kinetics is overshadowed by factors such as vdW interactions; however, in cases where barriers of 20 kJ/mol become significant (e.g., low reaction temperatures), it may be possible to discern subtle differences in reaction rates among zeolites with distinct acid siting.

Aluminum siting in zeolite frameworks is not always random, but can be manipulated by the judicious control of synthesis conditions that include (but are not limited to) SDAs, silicon or aluminum sources, heteroatom incorporation (e.g., B, Ge, Ga, etc.), seeding (or accompanying interzeolite transformations), and gel composition. SDAs typically contain positively-charged functional groups, which can interact with anionic  $[\text{AlO}_2]^-$  sites, thereby impacting Al siting in zeolite frameworks. Several groups have explored the possibility of altering both proximity and siting of Al by varying the charge-density of SDAs. For example, Gounder and coworkers [8] have reported on the effects of relative ratios of organic (N,N,N-trimethyl-1-admantylammonium) and inorganic ( $\text{Na}^+$ ) cations to influence the arrangement of paired and isolated Al (**Figure 1.2a**) in SSZ-13 (**CHA**). Rimer and coworkers [9] demonstrated that cooperative effects of organic molecules, such as  $\text{CTA}^+$  or tetrapropylammonium ( $\text{TPA}^+$ ), and inorganic cations (e.g.,  $\text{Na}^+$  or  $\text{K}^+$ ) can be exploited to direct Al positioning in ZSM-5 (**MFI**) to either channel (straight and sinusoidal) or their intersections (**Figure 1.2b**). One method to tailor Al siting among different lattice sites is through the selected combination of silicon and aluminum sources. Dědeček and coworkers [13] employed this approach to show that the use of colloidal silica can enrich acid sites in sinusoidal and straight

channels of ZSM-5, whereas switching the silicon source to tetraethyl orthosilicate (TEOS) selectively places Al at channel intersections. The same group also hypothesized that the choice of aluminum source (**Figure 1.2c**) can impact the fraction of paired Al sites in the following order:  $\text{Al(OH)}_3 > \text{AlCl}_3 > \text{AlPO}_4 > \text{Al(NO}_3)_3$  [10]. Aluminum siting can also be regulated by introducing heteroatoms (e.g., B, Ge), where it has been demonstrated that the variation of heteroatom-to-Al ratio in synthesis mixtures can impart unique acid siting. An alternative strategy involving interzeolite transformations was reported by Yokoi and coworkers [73] who showed that **CHA**-type zeolites crystallized from faujasite (**FAU**) as a parent zeolite results in a higher proportion of  $\text{Q}^4(2\text{Al})$  compared to **CHA** synthesized directly from amorphous reagents. Analogous approaches have been used by Dusselier and coworkers [74] to alter paired Al sites in **CHA**, whereas others have reported synthesis temperature can bias Al positioning [75]. Similar effects were demonstrated by Rimer and Okubo [76], who synthesized a highly siliceous FAU zeolite (HOU-3) with biased Al siting by simultaneously varying the alkalinity and water content of the starting gel. Using a combination of solid-state NMR and theoretical calculations, this study verified that Al incorporation is biased, leading to  $\text{Q}^4(n\text{Al})\text{Si}$  species with low energy configurations. Despite these and other examples, the control of Al siting via manipulation of synthesis parameters still remains more of an art than a science. Moreover, a limited number of examples makes it difficult to generalize trends among a broad class of zeolite structures.

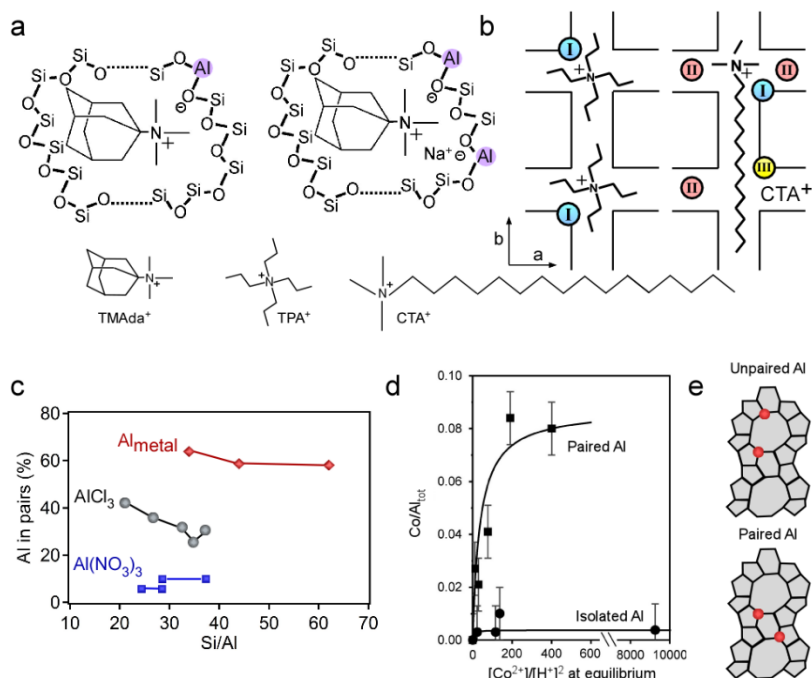


**Figure 1.2.** (a) Scheme of Al in **CHA** [8]. (b) Scheme of different Al siting in ZSM-5 channels and intersection [9]. (c) Effects of Al source on the proportion of paired Al sites ZSM-5 [10]. (d) Cobalt ion exchange isotherms for SSZ-13 [11]. (e) Schemes of unpaired and paired Al [10].

Strategies for selecting synthesis conditions *a priori* to tailor Al siting and coordination are generally deficient owing in large part to the complexity of zeolite crystallization [26]. Indeed, zeolite growth mixtures are sol gels containing a wide variety of precursors ranging from monomer and oligomers to nanocrystals and amorphous particles [77]. Knowledge of these nonclassical growth pathways is limited due in large part to the lack of available techniques [78] that can capture the dynamics of crystallization with sufficient spatiotemporal resolution; therefore, this area of research presents opportunities to further develop novel *in situ* techniques to shift current trial-and-error methods to more predictive approaches in zeolite synthesis. The rational design of zeolite catalysts would benefit from increased efforts to address

knowledge gaps in growth mechanisms with parallel efforts to advance materials characterization towards improved control of Al incorporation.

A long-standing challenge to develop structure-performance relationships in zeolite catalysis is the inability to spatially resolve Al siting. In recent years, there have been a number of advancements in the development of analytical tools to quantify Al siting and proximity with greater accuracy. Magic angle spinning nuclear magnetic resonance (MAS-NMR) spectroscopy of both  $^{29}\text{Si}$  and  $^{27}\text{Al}$  in combination with DFT calculations [79] has been employed to probe  $\text{Q}^4(\text{nAl})\text{Si}$  speciation and averaged Al-O-Si bond angles, respectively. These synergistic analyses have enabled the identification of Al sites in a number of zeolites, such as ferrierite, ZSM-5, MCM-22, and ZSM-11; however, recent studies have shown that it is often nontrivial to obtain quantitative information solely from NMR data. For instance, Dědeček and coworkers [80] report Al proximity can lead to  $^{27}\text{Al}$  isotropic chemical shifts up to 4 ppm, which can be misinterpreted as distinct crystallographic sites leading to controversial interpretations. Alternative techniques employing X-rays can be particularly useful owing to their large penetration depth for atomic level characterization. For example, Lercher and coworkers [81] used extended X-ray absorption fine structure (EXAFS) analysis in combination with DFT-trained molecular dynamics simulations to demonstrate the preferential occupancy of Al in zeolite beta (\***BEA**). Moreover, van Bokhoven and coworkers used an X-ray standing wave technique [82] and X-ray emission spectroscopy [83] to determine the diversity of Al sites (with atomic level resolution) in a natural zeolite (scolecite) and synthetic ferrierite, respectively. In general, X-ray

diffraction (XRD) methods lack the sensitivity to distinguish aluminum from silicon in the framework due to their similar scattering length density; however, it is possible to identify the location of organic SDAs in zeolite pores, which are extra-framework counterions that can also form hydrogen bonds with framework oxygen atoms to influence Al occupancy. Pérez-Pariente and coworkers [84] demonstrated that Rietveld refinement of synchrotron XRD patterns can elucidate the location of SDAs within the channels/cages of zeolites. Rimer and coworkers [85] used synchrotron XRD in combination with molecular modeling and solid-state two-dimensional NMR to show that SDAs influence Al siting in **MOR**. Additional methods to examine Al siting include atom probe tomography [86] where three-dimensional element distribution maps of thin needle-shaped samples (ca. 100 nm) are generated with exceptional spatial resolution (0.1 to 1 nm) using focused ion beam (FIB) milling. Alternatively, titration methods have been adopted in numerous studies to quantitatively characterize the proportion of paired and isolated sites in zeolite frameworks. Several groups [10, 12, 14, 87] have proposed that paired aluminum arrangements can be titrated by divalent metal cations (e.g.,  $\text{Co}^{2+}$  or  $\text{Cu}^{2+}$ ), whereas isolated sites compensate monovalent cations (e.g.,  $\text{H}^+$  or  $\text{Na}^+$ ). The adsorption of divalent metal cations is often quantified by UV-visible spectroscopy. An analogous approach involves the use of a probe reaction, such as methanol dehydration or alkane cracking (i.e., constraint index) to deduce Al arrangements [79].

Among these techniques,  $\text{Co}^{2+}$  titration is a common and facile approach to characterize the proximity and mutual arrangement of Al atoms. Prior studies have used

this technique on a limited set of zeolites (ca. 7) to categorize the local arrangement of framework Al atoms as: (i) paired Al representing two Al atoms in a single ring separated by two or three Si atoms (**Figure 1.2d,e**); (ii) unpaired Al in reference to Al atoms that are either close enough to bridge hydrated  $\text{Co}^{2+}$  ions (**Figure 1.2e**) or are located at sites that orient Brønsted acids in different pores; and (iii) isolated Al separated by more than three Si atoms (Figure 1d). The quantification of proximal Al is accomplished using  $\text{Co}^{2+}$  ion-exchange isotherms (**Figure 1.2d**) in combination with UV-Vis spectroscopy. It has been shown that both bare  $\text{Co}^{2+}$  ions and  $\text{Co}^{2+}\cdot 6\text{H}_2\text{O}$  can titrate Al pairs, whereas unpaired Al are able to accommodate  $\text{Co}^{2+}\cdot 6\text{H}_2\text{O}$  [80]. In contrast, isolated Al are not detected by this technique (i.e., they are compensated by monovalent cations, such as  $\text{H}^+$  or  $\text{Na}^+$ ). Dědeček and coworkers [88] used  $\text{Co}^{2+}$  titrations in combination with UV-Vis and  $^{29}\text{Si}$  MAS NMR spectroscopy to show a unique arrangement of Al atoms in Si-rich ( $\text{Si}/\text{Al} < 18$ ) zeolite beta wherein the majority of proximal Al configurations are either paired Al or unpaired Al (analogous to **Figure 1.2e**); however, the latter have not been observed for all zeolites (e.g., **MOR**) [89]. Recent studies have demonstrated that it is often nontrivial to obtain quantitative information solely from titrations. For instance, during dehydration of zeolites the  $\text{Co}^{2+}\cdot 6\text{H}_2\text{O}$  complex can form Co-oxo species [80], which are challenging to distinguish from bare  $\text{Co}^{2+}$  ions, and can lead to controversial results.

Despite limited control of Al siting, studies have demonstrated placement of acids at specific locations in zeolite catalysts can significantly impact activity, stability, and/or selectivity for reactions that include methanol dehydration, carbonylation, methanol-to-

hydrocarbons (MTH), oligomerization, cracking, and methane oxidation. For example, Iglesia and coworkers [90] observed a direct correlation between carbonylation rates and Al sites within the 8-membered ring side pockets of **MOR**. A similar study by Davis and coworkers [91] revealed that the selective placement of Al in 8-MR channels of ferrierite (**FER**) using a combination of SDAs can markedly influence the rate of carbonylation. Framework Al siting can also decidedly alter the dual cycle mechanism of MTH reactions. For example, it has been proposed [92, 93] that acid sites located at the channel intersections of ZSM-5 promote the aromatic cycle, whereas it is suggested that Al in the narrower channels favors the olefin cycle. Thus, it is possible to markedly enhance catalyst selectivity and/or stability if zeolites can be synthesized with well-defined Al siting.

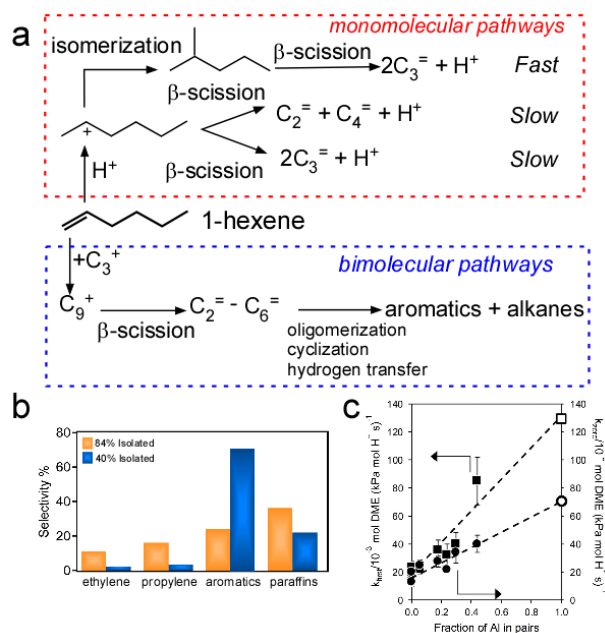


**Figure 1.3.** (a) Pathways for cracking of 1-hexene in ZSM-5 [12]. (b) Impact of Al proximity on the cracking of 1-hexene over ZSM-5 [13]. (c) 0<sup>th</sup> (circles) and 1<sup>st</sup> rate constants (squares) for MeOH dehydration increase with increased proportion of paired Al sites in the **CHA** [14].

The impact of Al location extends to sites in close proximity owing to their unique properties and ability to stabilize multivalent extra-framework species. Dědeček and coworkers [13] determined the effect of Al proximity in ZSM-5 on product yields in 1-hexene cracking (**Figure 1.3a and b**), showing a higher fraction of paired Al atoms enhances the hydrogen transfer reaction to produce more aromatics (**Figure 1.3a**) in comparison to ZSM-5 with isolated Al that promotes cracking to enhance light olefins selectivity. Similar effects have been observed in methanol dehydration to dimethyl ether (DME), which is the first step in the MTH reaction. For example, Gounder and coworkers [14] showed that both zero-order and first-order rate constants increase with increasing proportion of paired Al sites (**Figure 1.3c**). They attributed the increase in rate constants to a transition in the mechanism from an associative to dissociative adsorption pathway. Grabow and coworkers [66] employed periodic DFT to show that the location of Brønsted acids at different tetrahedral (T) sites within ZSM-5 channels (straight, sinusoidal, and intersections) can significantly influence the kinetics of DME formation, resulting in a broad temperature range (ca. 300 K) where the dominant pathway switches from associative (**Figure 1.4**, black lines) to dissociative (**Figure 1.4**, red lines). Thus, the potential for ZSM-5 catalysts used in different studies to exhibit distributions in Al siting may explain why there are conflicting claims in the literature regarding the dominant mechanism for this reaction [94]. When Brønsted acids are located in close proximity, there is the potential to stabilize Lewis acids (i.e., ions, metals, or oxides) [95]. Among the more widely studied materials are Cu- and Fe-exchanged SSZ-13 zeolites that have attracted significant interest over the years for

either emission catalysis or methane activation applications. The speciation of extra-framework Cu or Fe [95] can be manipulated by altering the proportion of paired/isolated Al sites in the zeolite framework. Specifically, paired Al sites can accommodate  $\text{Cu}^{2+}$  ions while isolated Al sites exchange  $[\text{CuOH}]^+$  ions [96]. It has also been shown by Román-Leshkov and coworkers [97] that paired Al sites can stabilize the dimeric motif  $[\text{Cu-O-Cu}]^{2+}$ .

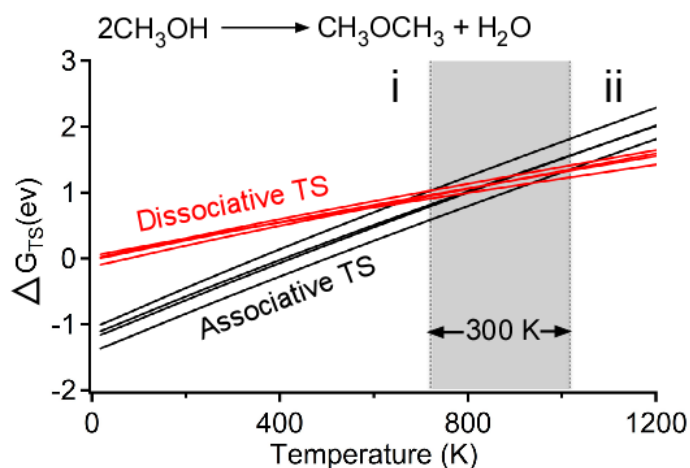


**Figure 1.4.** Thermal contributions to the Gibbs free energy change the reaction mechanism from the associative route (black lines, region i) to the dissociative route (red lines, region ii). Dual mechanisms are possible in a temperature window (gray zone) [66].

Synthesizing zeolites with precisely-controlled placement of Al at specific T sites is highly nontrivial. In order to validate Al siting, proper characterization necessitates a combination of multiple techniques, yet even the most sophisticated tools available have bottlenecks. Common techniques such as solid-state NMR offer limited ability to differentiate T site occupancy. For zeolites with only one unique T site,  $^{29}\text{Si}$  MAS NMR can provide general insight into the relative percentages of  $\text{Si}(\text{OAl})_n$  species; however, for zeolites with multiple (distinct) T sites, quantifying Al siting is more challenging and data can be subject to over-interpretation, such as the deconvolution of a single

broad peak in  $^{27}\text{Al}$  MAS NMR spectra into numerous individual peaks. Improved capabilities of  $^{27}\text{Al}$  triple quantum magic angle spinning (3Q MAS) and ultrahigh field  $^{27}\text{Al}\{^1\text{H}\}$  2D correlation NMR experiments have led to unique insights with respect to isolated and paired Al siting. For example, Sauer and coworkers [98] employed  $^{27}\text{Al}$  3Q MAS NMR spectroscopy combined with theoretical DFT calculations to accurately resolve 12 out of 24 distinct resonances for of ZSM-5 zeolite corresponding to Al located at different T sites. Advanced characterization techniques, such as 3Q MAS NMR, have the potential to provide atomic-level descriptions of acid siting, which is essential for developing structure-performance relationships in zeolite catalysis.

### **1.2.2 Framework-associated and extra-framework aluminum**

Here we extend our discussion beyond framework Al (FAI, tetrahedral coordination) to highlight the broad range of framework-associated aluminum, distorted tetrahedral Al, and extra-framework aluminum (EFAl), which include partially uncoordinated Al (tri-coordination and penta-coordination), and fully uncoordinated octahedral Al [99]. This diversity of Al speciation adds complexity to zeolite catalysis based on uncertainties of how non-framework sites are generated, where they are located, how their acidity may differ from FAI, and to what extent their unique properties influence catalyst performance. Many of these questions are unanswered, although some progress has been made. For instance, Rosenbach and coworkers [100] theoretically posit that EFAl exists in one of two forms: cations (e.g.,  $\text{Al}^{3+}$ ,  $\text{AlO}^+$ ,  $\text{Al}(\text{OH})^{2+}$ ,  $\text{Al}(\text{OH})_2^+$ ) or neutral species (e.g.,  $\text{AlO}(\text{OH})$ ,  $\text{Al}(\text{OH})_3$ ,  $\text{Al}_2\text{O}_3$ ). EFAl is present in as-synthesized zeolites but is frequently generated via hydrolysis of Si-O-Al bonds during post-

synthesis treatments, such as ion exchange, steaming, and acid leaching, or *in situ* under certain reaction conditions. Dealumination can be an intentional step in catalyst design for the purpose of creating mesopores, regulating acid site density (i.e., increasing Si/Al ratios), and/or modifying hydrothermal stability. The putative mechanism(s) of dealumination differ depending on the composition and type of zeolite framework. It has been shown for several zeolites that there is an unexplained hierarchy for the extent of dealumination [101], where particular T-sites can be more susceptible [102]. For ZSM-5 it has been demonstrated with DFT calculations [103] and FIB-SEM tomography [104] that EFAl species can migrate to preferred locations (i.e., straight channels) where they prevent further localized dealumination, but allow continued dealumination in other regions (i.e., sinusoidal channels).

The identity and corresponding role(s) of EFAl species in zeolite catalysis are subjects of ongoing debate, stemming in part from variabilities in synthesis methods as well as limitations for characterizing Al speciation (*vide supra*). Resolving Al speciation by NMR is highly sensitive to the degree of hydration and sample pretreatment, where more uniform testing protocols need to be established, including careful attention to pretreatment steps that can modify zeolite structure and/or composition. Characterization of EFAl species is also challenging owing to their interaction with proximal framework and non-framework species [105]. For example, quadrupolar broadening effects in the  $^{27}\text{Al}$ -NMR spectra of dehydrated zeolites often leads to reduced spectral resolution or renders some features invisible. To address these limitations, various solid state NMR techniques can be used to analyze EFAl, such as

controlled hydration treatment, high field/multinuclear NMR, and the use of adsorbed probe molecules. Most notably, Deng and coworkers [106] utilized select organic molecules (e.g., acetone or trimethylphosphine) to determine EFAl speciation, quantify Lewis acidity, and identify their local environment(s). One complexity of  $^{27}\text{Al}$  MAS NMR analysis is the assignment of chemical shifts for distorted tetrahedral Al or penta-coordinated EFAl species that is highly sensitive to the degree of zeolite hydration [107] and post-synthesis treatments (e.g., penta-coordinated EFAl species can be removed when exposed to basic media) [108].

A third class of Al speciation is so-called framework-associated species, which are unique in their ability to change coordination in response to local environments, and thus can be categorized as either FAI or EFAl depending on temporal changes in their speciation. The identification of these species can prove to be challenging owing to their ability to reversibly switch from octahedral to tetrahedral speciation. For instance, the octahedral form  $\text{AlOH}$ , which is generated from the partial hydrolysis of framework Al-O bonds [58], can reverse to a tetrahedral coordination upon ion-exchange, adsorption of ammonia, or thermal treatment. These sites were identified in **MOR** by van Bokhoven and coworkers [59] who assigned them as Lewis acid sites and extended this classification to all zeolites. They proposed that the Lewis acidity from these species can be transient owing to their propensity to change coordination. Furthermore, their formation depends on proximal (or paired) Al sites, which are more prevalent in zeolites with low Si/Al ratios.

Identification of Al species is critical to establishing structure-performance

relationships in zeolite catalysis. The majority of studies reporting the effects of EFAl species focus on alkane cracking reactions. While there is general agreement that EFAl influences catalytic cracking activity, there are multiple explanations for its origins. For instance, Bartholomeuf [109] and others suggested a synergistic effect of EFAl on neighboring Brønsted acid sites, leading to stronger intrinsic acidity; however, claims of enhanced intrinsic acidity in early studies were based on rate normalization by total Al content, which lends itself to evaluation of “apparent” acid strength. A more accurate method of rate normalization is the use of Brønsted acid concentration [16], which typically does not correlate exactly with total Al content (i.e., Si/Al ratio). This highlights the importance of resolving the identity and properties of Al species to establish an improved understanding of individual contributions to the overall (apparent) acid strength. Explicating the impact of EFAl on catalyst performance is often complicated by the inability to differentiate the contributions of local confinement, Al speciation, and cooperative effects of multiple site proximity. One example demonstrating the impact of proximal FAl and EFAl sites is the work of Deng and coworkers [15] who used  $^{13}\text{C}$ -labelled acetone as a probe molecule in NMR to measure Brønsted acid strength in ZSM-5, mordenite, and dealuminated HY zeolites. They observed that hexa-coordinated  $\text{Al}(\text{OH})_3$  and penta-coordinated  $\text{Al}(\text{OH})^{2+}$  in proximity to FAl (**Figure 1.5a and b**) enhances Brønsted acidity (based on the assumption that chemical shifts in  $^{13}\text{C}$  NMR spectra attributed to acetone-proton interactions can be used as a measure of Brønsted acid strength). However, it is important to note these measurements reflect apparent acid strength due to probe molecule interactions with the

confined pores of the zeolite.

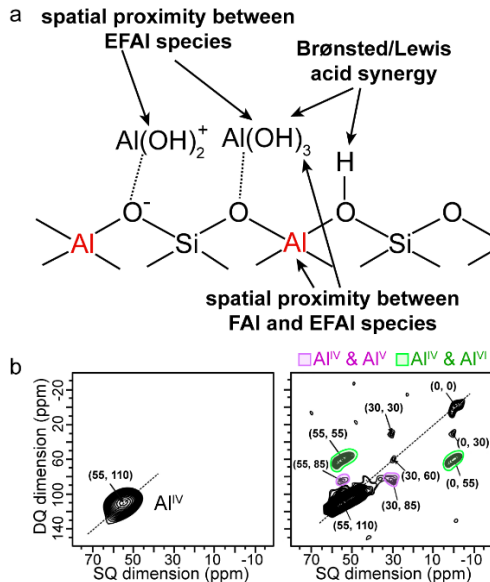


**Figure 1.5** (a) Scheme of EFAI and FAI site proximity in ZSM-5 framework to demonstrate Brønsted/Lewis acid synergy. (b) Al DQ-MAS NMR spectra of parent H-ZSM-5 (left) and dealuminated H-ZSM-5 (right). Adapted from [15].

Alternative explanations have been proposed to explain the effect of vicinal EFAI species on enhanced cracking activity. Some studies have used techniques such as calorimetry to suggest that EFAI improves catalyst activity by altering reactant heat of adsorption [110], while others posit dispersion forces (i.e., confinement effects) or charge delocalization (i.e., entropic stabilization of transition states) stabilize transition states and enhance alkane cracking activity. For instance, Iglesia and coworkers [16] performed isobutane cracking and on-stream acid site titration over zeolite Y (**Figure 1.6a**) and showed no correlation between reaction rate and available Al acid sites; and hence they concluded that enhanced reaction rates are not due to an intrinsic increase in Brønsted acidity, but rather a stabilization of intermediates via dispersion forces [111] (e.g., additional confinement effects imposed by EFAI partially blocking cages/pores).

Lercher and coworkers [112] offered a similar explanation based on kinetic studies of paraffin (n-butane and n-pentane) cracking over ZSM-5 catalysts with different steam treatment to vary EFAl concentration. They hypothesized that enhanced cracking activity was attributed to the proximity of EFAl and strong Brønsted acid sites, which induces steric constraints and increases activation entropies of transition states.

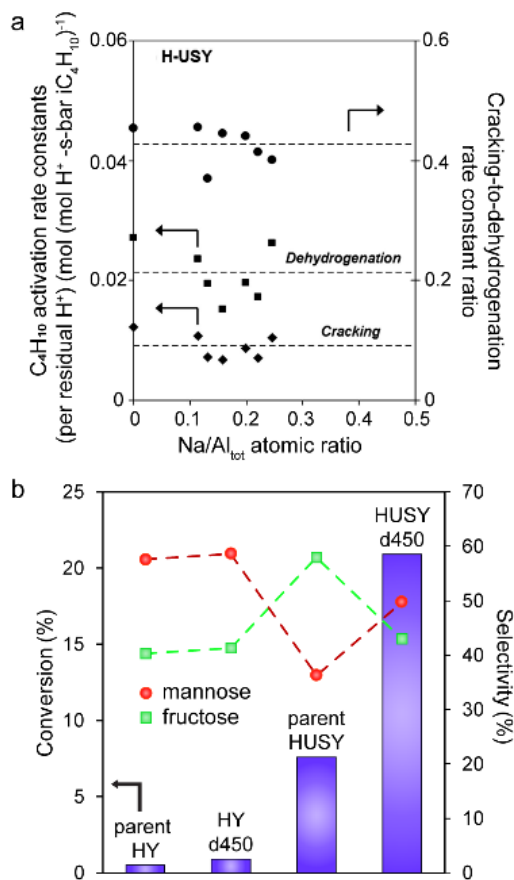


**Figure 1.6** (a) Isobutane cracking rate constants as a function of Na<sup>+</sup> titrated sites-to-total Al ratio for HUSY [16]. (b) Conversion and selectivity for glucose isomerization reaction of Y zeolites with different tri-coordinated EFAl. Adapted from [17].

From these collective studies, it is evident that vdW contributions and/or cooperative interactions between EFAl and Brønsted acids can lead to the reported

enhancement of activity; however, the contribution of each is clearly dependent upon EFAl properties (i.e., concentration, speciation, and distribution). More insight into the impact of EFAl could be achieved by adopting similar methods as those previously described for the systematic analysis of isolated and paired FAI sites. For instance, the ability to selectively control EFAl properties to vary the number of isolated EFAl sites versus paired sites (i.e., EFAl – EFAl and EFAl – FAI) could offer ways of determining which effects (dispersion or proximal site interactions) are most dominant.

The influence of EFAl species on catalyst performance can also be attributed to the introduction of Lewis acidity, which benefits certain reactions (e.g., biomass conversion) and is detrimental to others. For example, tri-coordinated EFAl  $\text{Al}^{3+}$  species, often referred to as “invisible Al” due to its undetectability in 1D or 2D  $^1\text{H}$  and  $^{27}\text{Al}$  NMR spectra, can exhibit strong Lewis acidity. Evidence to support this claim has been gleaned from solid state  $^{31}\text{P}$  NMR using chemical shifts of adsorbed TMP (trimethyl phosphine, probe molecule) in dealuminated HY and HUSY to ascertain Lewis acid strength [17]. The enhanced Lewis acidity of tri-coordinated EFAl species (e.g., HUSY and dealuminated HUSY) promotes higher conversion in liquid-phase glucose isomerization (**Figure 1.6b**) compared to catalysts with little to no tri-coordinated EFAl (e.g., HY and dealuminated HY). Another study evaluating EFAl  $\text{Al}^{3+}$  in the ethanol-to-hydrocarbons reaction also reports high Lewis acidity; and shows that when these species are present in equal concentration as Brønsted acid sites, there is noticeably higher ethylene selectivity [113]. Lercher and coworkers [114] investigated MTH reactions where they showed that increased concentration of Lewis acid sites

associated with EFAl enhanced product selectivity from hydride transfer. They proposed that these sites catalyze the formation of formaldehyde as an intermediate responsible for the propagation of light alkanes and aromatics, which leads to accelerated catalyst deactivation. Recently, there has been increased interest in the initial C-C bond formation in the MTH reaction leading to the formation of ethylene (i.e., before the autocatalytic cycle) [115]. Mechanistic arguments have been proposed from combined DFT and NMR studies where the coupling is initiated by surface-bound methoxy [116] or formaldehyde [117] species on EFAl. Many studies focusing on the characterization of framework-associated species and/or EFAl have led to various interpretations regarding their putative role(s) in acid catalysis. Given the large diversity of Al species in zeolite catalysts, there are many opportunities to expand mechanistic understandings of their impact on heterogeneous catalysis.

### **1.3. Elemental zoning and core-shell analogues**

A topic that has received relatively little attention is the effect of zoning in zeolite synthesis and its impact on catalyst performance. This phenomenon produces either Al-zoning where the exterior surface is Al-rich or Si-zoning where the exterior surface is Si-rich (**Figure 1.7a**). Zoning has been reported for only a few zeolites and zeotypes (e.g., **MFI**, **AFI**, **CHA**, **MOR**, **LTA**, and **FAU** frameworks), yet we believe this phenomenon is more pervasive because it often goes undetected. Various groups have attributed zoning to the selection of synthesis conditions, such as the use of organic and/or inorganic SDAs [118] and the starting Si/Al gel ratio [119]. Post-synthesis dealumination processes can also lead to zoning due to Al migration (e.g., steaming) or

Si deposition (e.g., when using HCl or ammonium hexafluorosilicate) [120]. The most frequently reported case is Al-zoning [121], which can be present in as-synthesized materials or generated by selective desilication. Perez-Ramirez and coworkers [18] have used energy-dispersive X-ray spectroscopy (EDX) mapping to confirm Al-zoning in ZSM-5 crystals (**Figure 1.7b**). Likewise, van Bokhoven and coworkers [19] used FIB/EDX to map cross-sections of large ZSM-5 crystals, revealing 1-3  $\mu\text{m}$  thick Al-zoned regions (**Figure 1.7c**). Some studies exploring the origin of Al zoning have suggested it is a consequence of continuous Al migration to the surface of the growing crystals during synthesis [19] or a result of late-stage deposition of Al-rich crystals via oriented attachment [122]. Moreover, the observation of a sharp change in aluminum concentration from inner core to exterior regions of Al-zoned crystals suggests possible Al deposition on the surface during the isolation of solids (i.e., post-synthesis quenching) [123]. Examples of the counter configuration, Si-zoning, are relatively scarce. One notable exception is a study by Weckhuysen and coworkers [20] confirming Si-zoning in large ZSM-5 crystals (**Figure 1.7d**) via combined  $\text{Ar}^+$  sputtering and X-ray photoelectron spectroscopy (XPS).

Despite progress made in the identification of zoned zeolites, the fundamental mechanisms of formation and methods to selectively control this phenomenon are not well understood. Progress along these lines is tied to the development and/or application of tools to analyze samples at periodic stages of synthesis. Elemental mapping allows for coarse visualization of zoned regions; however, the change in Si/Al ratio as a function of crystal depth is difficult to spatially resolve. Weckhuysen and coworkers

have employed advanced characterization techniques to improve the resolution of single-particle elemental analysis. For instance, they correlated mesoscopic regions of Al-zoning to catalyst performance using scanning transmission X-ray microscopy (STXM) to non-destructively map the 3D distribution of Al (and its local coordination environment) with nanoscale resolution [124]. To our knowledge, there are few examples of new analytical tools being applied to progress the state-of-the-art; however, in the future we anticipate a growing list of *in situ* techniques will afford greater opportunities for resolving molecular (or atomic) details of zoned materials.

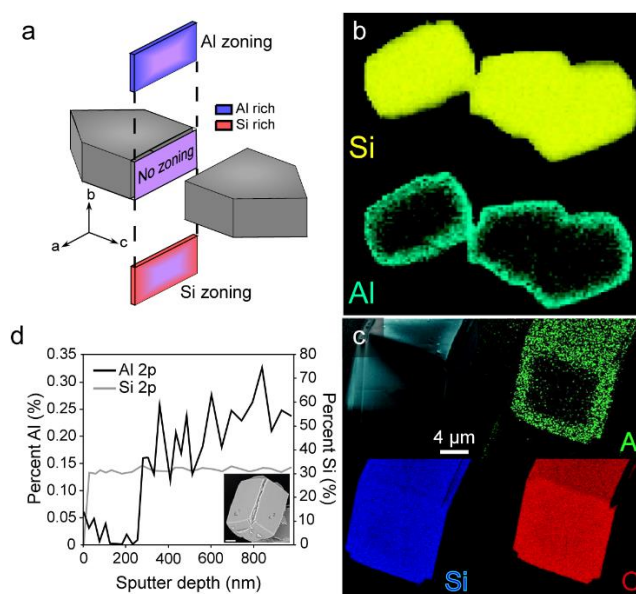


**Figure 1.7.** (a) Scheme of Al-zoning and Si-zoning. (b) Elemental mapping in ZSM-5 using SEM-EDX [18]. (c) Cross-sectional EDX mapping of Al-zoned ZSM-5 [19]. (d) Percentages of Al and Si in a Si-zoned ZSM-5 crystal (inset) from XPS and Ar<sup>+</sup> sputtering [20].

When expanding beyond single sites to assess the impact of spatial gradients in elemental composition throughout a catalyst particle, we posit zoning is more prevalent than reported in literature; however, the paucity of examples obfuscates the establishment of direct correlations between zoning and catalyst performance. Indeed,

the activity of Al sites tends to be averaged across the entire catalyst without consideration of spatial gradients in acid density (or variants in Al speciation, as discussed in Section 2.2). We speculate that zoning goes unidentified due to a lack of surface characterization (e.g., XPS) in favor of bulk measurements (e.g., EDX or ICP) that provide average values of the Si/Al ratio. A limited number of Al-zoned zeolite studies suggest a detrimental effect on catalyst performance, such as a higher rate of coking in MTH reactions [125] or reduced p-xylene selectivity in toluene disproportionation [126]. Rimer and coworkers [127] reported that Al-zoning in ZSM-5 samples prepared at low temperature (100°C) exhibit poorer activity in MTH reactions compared to catalysts with homogenous Al distribution (synthesized at higher temperature), which was attributed to an increased percentage of non-framework Al sites in the former. On the contrary, studies of Si-zoned zeolites tend to reveal a positive impact on catalyst performance. For instance, Si-zoned ZSM-5 in n-butane dimerization can lead to high octane components [128] as well as improved dimethyl ether selectivity in methanol dehydration [129]. Weckhuysen and coworkers [130] assessed the coking of Si-zoned ZSM-5 crystals in three different reactions using UV-Vis and confocal fluorescence micro-spectroscopy. For styrene oligomerization, they concluded that there is no observable pore blockage at the boundary between the inner core and Si-zoned regions; for MTH reactions they demonstrated that Si-zoning reduces graphitic coke accumulation on the external surfaces of catalysts; and for the aromatization of light naphtha (LNA) they report a rapid reaction of olefins at the zoning boundary that can limit reaction diffusion within the catalyst interior. Recently, Ma and coworkers

[131] reported that Si-zoned ZSM-5 crystals are shape selective for p-xylene and exhibit improved stability in methanol-toluene alkylation due in part to their hydrophobic Si-rich external surface. In the future, it is imperative to gather more data of zoned catalysts in order to further develop understanding of its impact on catalytic performance. It would be equally advantageous if academics and industrial practitioners put into common practice surface characterization of zeolite catalysts as a way of identifying zoning.

Direct preparation of zeolites with mesoscopic gradients in elemental composition (Si/Al ratio) is currently an empirical endeavor. Synthesis of such materials typically involves multi-step or post-synthesis processes to generate core-shell or surface-passivated materials, which are analogues to Si-zoned zeolites. Surface passivation involves the functionalization of zeolite surfaces to yield relatively thin layers of distinctly different composition. This technique was commercialized by DuPont and Mobil in the 1980's and has been used by many groups to prepare zeolites with a thin siliceous exterior layer using either chemical vapor or liquid deposition (CVD or CLD) with silanes. The overarching motivation for surface passivation is to eliminate reactions on the external surface, thus imposing shape selectivity within the interior pores. Several groups have cited improvements in light olefins and/or para-selectivity (and separation) for methanol conversion, cracking, methanol-toluene alkylation, and toluene disproportionation; however, the origins of enhanced catalytic performance can be convoluted, often attributed to alternative factors such as pore-narrowing as a result of the passivating layer, which can improve selectivity at the expense of activity.

The concept of core-shell design has been applied to a multitude of catalytic materials for diverse applications. For zeolites, there are many types of core-shell structures that include variants of Si- or Al-zoning, the encapsulation of metal or metal-oxides, and mixtures of two different frameworks [132]. For example, Martens [133] and Valtchev [134] developed distinct synthesis methods for the preparation of zeolite core-shell composites of different structures, such as beta@silicalite-1, in order to capitalize on their disparate pore networks in catalytic reactions. Indeed, core-shell composites have demonstrated enhanced selectivity in fluid catalytic cracking (FCC), hydrocracking, n-butylene cracking, cellulose hydrolysis, and enantioselectivity in racemic reactions. Herein, we focus our discussion on core-shell zeolites where the core and shell are of identical framework type. Mobil provided one of the earliest examples of zeolite core-shells by showing that a silicalite-1 shell can be grown over ZSM-5 (its aluminosilicate isostructure), similar to surface passivation. In most core-shell syntheses where the shell is a siliceous zeolite (e.g., **MFI**, **TON**, **MTT**, **MWW**, or **LTA**), it is often observed that the shells are polycrystalline with thicknesses in the hundred nanometers to microns range [132] with few exceptions [22, 135]. When the core and shell are not in perfect crystallographic registry, or when the shell thickness is prohibitively large, these factors can introduce additional mass transport limitations. Some groups [135, 136] have examined methods to lessen these effects via the generation of mesoporous cores prior to encapsulation with the shell.

There is consensus that both surface passivation and core-shell zeolites with siliceous shells have positive effects on catalysis, such as higher light olefins and/or p-

xylene selectivity and enhanced conversion capacity. For example, Nishiyama and coworkers [21] showed that the core-shell catalyst Zn/ZSM-5@silicalite-1 improved xylene isomer selectivity (**Figure 1.8a**) and reduced the rate of coke formation (**Figure 1.8b**) in methanol to aromatics; however, studies such as these are subject to various mechanistic interpretation of enhanced core-shell performance since the observed effects can be attributed to one or more factors, such as diffusion limitations, surface passivation, or the presence of extra-framework species (e.g., EFAl or metal oxides). Siliceous shells can also increase the hydrophobicity of a catalyst, which has proven to be beneficial in applications such as NH<sub>3</sub>-SCR reactions and volatile organic compounds (VOC) capture. Rimer and coworkers [22] developed a synthetic route to prepare nano-sized ZSM-5@silicalite-1 catalysts (**Figure 1.8c**) where the epitaxial growth of the silicalite-1 shell can be controlled to yield thicknesses of 5-20 nm with crystallographic registry equal to the underlying ZSM-5 core (**Figure 1.8d**). Similar core-shell configurations (with larger shell thickness) can be rapidly synthesized (e.g., order of minutes) using tubular reactions [137]; however, the broad difficulty of synthesizing well-defined core-shell zeolites via facile methods poses a significant hurdle to develop fundamental understandings of reaction pathways for this class of catalytic materials.

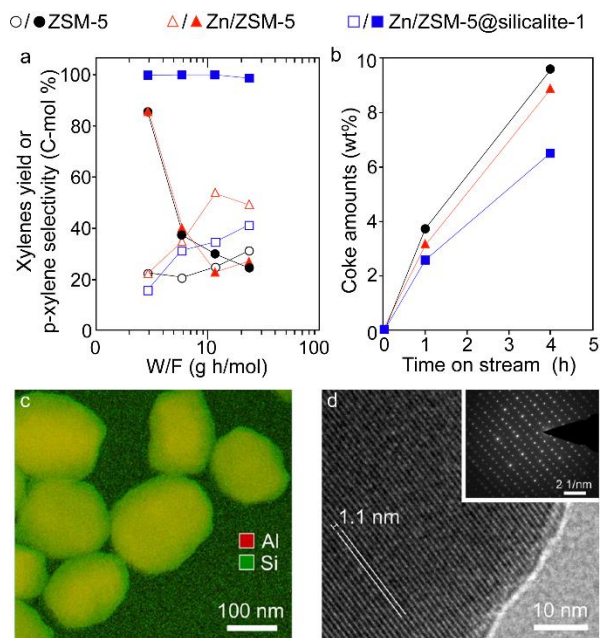


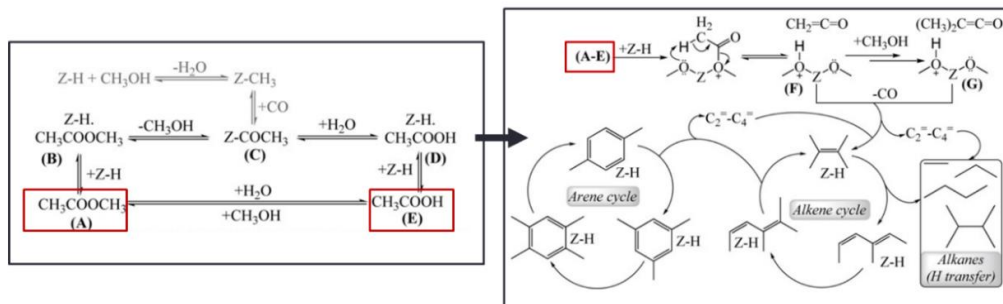
**Figure 1.8.** (a) Xylene yields and p-xylene selectivity (open and closed symbols) for methanol to aromatics reactions. (b) Coke amounts as a function of time on stream [21]. (c) EDX mapping, (d) HRTEM image and SAED pattern of ZSM-5@silicalite-1 [22].

In summary, the synthesis of core-shell materials is nontrivial owing to the challenges of epitaxial shell growth to ensure the continuity of pores between core and shell, as well as the ability to selectively tailor shell thickness to minimize mass transport limitations. Most examples in literature do not sufficiently meet these criteria, whereas those that do report uniform, thin ( $< 10$  nm) shells are restricted to **MFI**. Epitaxial growth of core-shell catalysts with tunable shell thickness has demonstrated how advanced knowledge of zeolite growth aids in the design of novel catalysts. A major obstacle for the generalization of this approach to other framework types is the difficulty of preparing purely siliceous zeolites; however, recent progress in the development of organic structure-directing agents holds considerable promise for expanding the list of core-shell zeolites.

#### 1.4 Recent Development of methanol-to-hydrocarbons reaction

Methanol to hydrocarbons (MTH) is a technology of high interest in the energy industry because it is a key step to gasoline-rich and olefin-rich products from alternative carbon sources, such as natural gas, CO<sub>2</sub>, coal, and biomass [138]. A recent scientific review of MTH reveals that several zeolites are effective catalysts for upgrading methanol to gasoline derivatives [139]. As such, major research initiatives in both industry and academia have been focused on improving the efficiency of MTH processes, with one critical optimization parameter being catalyst design. Although extensively researched, the MTH mechanism is still not fully understood, especially the lesser discussed process, known as the direct mechanism, responsible for the formation of the first C-C bond during the induction period which in turn feeds into the more well-known autocatalytic dual cycle mechanism [115]. Advancement in computational and experimental techniques has spurred various research efforts to identify and validate specific pathways and species associating with direct-coupling mechanism and linking it to the hydrocarbon pool mechanism. One such pathway, proposed concurrently by the Weckhuysen and Lercher independently, is Koch-type carbonylation, which is now a widely acknowledged route (**Scheme 1.1**) [140, 141]. It has been shown that the existence of CO (from decomposition of methanol) in the initial period of reaction helps catalyze the carbonylation of a surface methoxy group to generate a surface acetyl group, which eventually dissociates into methyl acetate or acetic acid. A recent study combining NMR and operando UV-vis diffuse reflectance spectroscopy further provides evidence for zeotype SAPO-34 of methyl acetate continuing to transform on

zeolite Brønsted acid site to form a highly reactive ketene, which subsequently forms C<sub>2</sub>-C<sub>4</sub> olefins via decarbonylation, with CO coproduct [23]. The key C<sub>2</sub>-C<sub>4</sub> olefins species [139] undergo further oligomerization and aromatization to form larger olefins and aromatic species that become part of the hydrocarbon pool and concomitantly transform into alkanes via hydrogen transfer reactions. The direct mechanism is a subject of on-going study with relatively few established structure-mechanism relationships. A few studies [115] have demonstrated the influence of various EFAL species in facilitating the formation of key species in the direct mechanism. On the other hand, the autocatalytic cycles, also known as the dual cycle mechanism, is relatively more established. The dual cycle mechanism involves an aromatic (arene) cycle and an olefins (alkene) cycle [142] which are connected via hydrogen transfer reaction. The relative propagation of the two cycles can be described with a selectivity ratio of ethene, the primary product of aromatic cycle, and the sum of 2-methylbutane and 2-methyl-2butene (2MB), the primary products of the olefin cycle [143]. More recently, various studies have also revealed the importance of formaldehyde in the dual cycle mechanism, which can accelerate the formation of bulky aromatic species (i.e., coke). Indeed, the dual cycle mechanism has been modified to include this critical species, formaldehyde [144-146].



**Scheme 1.1.** Proposed reaction pathways. Species A and E are methyl acetate and acetic acid from the proposed Koch carbonylation pathways. Adsorbed species F and G initiate formation of C<sub>2</sub>-C<sub>4</sub> olefins, leading to the autocatalytic mechanism. Z-H denotes the zeolite [23].

Improving the MTH process involves two main factors: reaction lifetime and product selectivity. The primary cause of reduced on-stream catalyst stability is zeolite deactivation due to coking, which involves the formation of bulkier products that obstruct pores and catalytically active sites [147]. Furthermore, even though zeolites possess excellent shape selectivity, controlling product selectivity in MTH presents challenges due to its intertwining reaction chemistry. Addressing these problems requires bridging of two approaches: physical alteration of zeolites (rational design) and fundamental reaction mechanistic studies. When tailoring the physicochemical properties of zeolites, conventional synthesis methods coupled with underdeveloped understanding of zeolite growth mechanism are often insufficient to achieve target properties. Although it is established that the physicochemical properties of zeolites (e.g., size, morphology, topology, and acid site concentration, or Si/Al) influence MTH reaction performance (lifetime, selectivity, etc.) [148], property-performance relationships are not well understood. In comparative studies of zeolite catalysts, multiple physicochemical properties of the catalysts or reaction conditions are oftentimes varied at once, and this leads to difficulties in deciphering the direct effect

of a particular parameter on catalytic performance. Controlling zeolite properties, in conjunction with reaction studies, will help elucidate the relationship between a zeolite's physicochemical properties and its catalytic performance.

### **1.5 Dissertation Outline**

With the multitude of zeolite properties, it is unreasonable to correlate catalytic performance to a single physicochemical property; a practice that can lead to conflicting trend. Furthermore, besides commonly characterized properties, zeolites can have unobservable defects which are detrimental to catalytic performance. A significant percentage of my dissertation is focused on understanding defects in zeolites through their characterization and integration in descriptors that can be used to account for their influence on catalytic performance, predominantly using MTH as a model reaction for extracting structure-performance relationships. Chapter 2 of this dissertation addresses techniques for probing crystalline defects in **MFI**-type zeolites with time-resolved dissolution study. These defects are not always observable, but can greatly influence catalytic performance. Subsequently, Chapter 3 summarizes comparative studies of zeolite ZSM-5 and zeotype SAPO-34 that establish structure-performance relationships in MTH wherein catalytically relevant descriptors are established as a basis for elucidating the effects of mesoscopic compositional distribution on MTH reaction performance for zoned ZSM-5 (Chapter 3). We further expand on the study of compositional gradient with core-shell ZSM-11 (Chapter 4). Chapter 5 will be designated to discussion of preliminary result and future work in the rational design of bifunctional zeolite catalysts informed by prior mechanistic studies.

## CHAPTER 2

### Time-resolved Dissolution Elucidates the Mechanism of Zeolite MFI

#### Crystallization

The materials discussed in this chapter will be published in a peer reviewed journal. Figure and table labels are reformatted to be consistent with dissertation formatting requirement. The work was in collaboration with Dr. Krassimir N. Bozhilov from University of California, Riverside, Dr. Zhengxin Qin from China University of Petroleum (East China), Dr. Tanguy Terlier from Rice University, Dr. Ana Palcic from the Ruđer Bošković Institute, and Dr. Valtchev from ENSICAEN.

#### 2.1 Motivation

Zeolites are a family of crystalline microporous tectosilicates that are extensively used as heterogeneous catalysts, molecular sieves, sorbents, and ion exchangers. The large-scale production of synthetic zeolites already has more than a half-century history. At present, the annual production is above 3 million tons per year [149]. About ten different types of zeolites are being used on a large industrial scale, and the number of zeolites used in niche markets is larger. These figures demonstrate the maturity of large-scale production of zeolites. Nevertheless, there are certain aspects of zeolite formation mechanism(s) that remain to be clarified.

The difficulty in understanding zeolite crystallization is mainly due to the heterogeneity of the growth mixtures containing solid and liquid components, and the presence of a myriad of different species (i.e., precursors) [150]. The complex interactions between these species and condensation steps leading to the formation of aluminosilicate frameworks around the inorganic and/or organic structure-directing agent is also difficult to be traced and unambiguously determined. The difficulty also stems from the fact that the formation of a particular zeolite could occur by more than

one crystallization pathway [26, 151, 152]. Different methods providing information for the short and long-range order in aluminosilicates, their chemical composition, and molecular interactions have been employed to shed light on the events preceding zeolite nucleation and the subsequent growth process [153-158]. Thus, the zeolite formation has been studied by a variety of scientific approaches to gain a comprehensive picture of the factors guiding the growth of a particular zeolite. For instance, snapshots of a particular stage of zeolite formation obtained by an *ex-situ* method or combination of methods was completed with *in situ* analysis using specially designed equipment [26, 151, 159-161]. Molecular modeling has also been used to decode zeolite formation in combination with experimental analyses [159, 162]. These continuous efforts have resulted in a generally accepted mechanism that describes the major stages of crystallization without, however, being able to provide a basis for zeolite synthesis by design [157, 163].

Studies focused on characterizing local zeolite structure have allowed for the identification of the nucleation and growth of specific crystal forms. Still, even these studies have not provided detailed highlights on the intimate stages of zeolite crystal growth [26, 151, 153, 154]. Understanding the growth history and establishing a detailed picture of each stage of zeolite formation would advance efforts to obtain a product with desired physicochemical properties; however, such a thorough, comprehensive analysis of the growth process for a single crystal is difficult to acquire by the currently available methods.

In this study, we employ a non-traditional approach to study crystallization

mechanisms: dissolution in an ammonium fluoride medium. Dissolution offers a route to identify defects or irregularities in crystals that form during growth, allowing us to observe where the weak bonds are located within zeolites and temporally track the progressive breaking of these bonds. Following the critical aspects of aluminosilicate dissolution, as summarized in detail by Crundwell [164-167], it is considered that during dissolution experiments, domains corresponding to stable, viable nuclei should dissolve last. Hence, the dissolution of the zeolite structure can be utilized to resolve the hydrothermal crystal growth mechanism by *ex situ* methods and to reveal information about the critical steps in their nucleation and growth. Such an approach allows for valuable insights of the growth process to be disclosed by identifying regions with high densities of defects in the crystal and their role in various stages of crystallization, i.e., the temporal trajectory of zeolite formation. The above presumption could be correct only when the etching agent is not chemically selective and will not react preferentially with the chemically inhomogeneous zones in the crystal (i.e., preferential removal of Si or Al). This differs from the vast majority of processes employing dissolution reported in literature. For instance, etching is largely used for the post-synthesis modification of zeolite properties [168-170]. Steaming is a commercial method for increasing the Si/Al ratio in zeolites [171, 172]. Mineral acids are also used to extract Al from zeolite frameworks, while caustic solutions are employed to preferentially remove Si [173-176]. However, these chemically selective etchants cannot be used to study the crystal growth of a zeolite.

Here we examine the unbiased dissolution of MFI-type zeolite crystals in a fluoride

medium at both a macroscopic and molecular level. Our recent results have shown that upon dual hydrolysis, the compound  $\text{NH}_4\text{F}$  provides species that dissolve Si and Al with similar rates [177]. Etching by  $\text{NH}_4\text{F}$  was used to obtain hierarchical materials with retained framework composition [178]. In the present study, we have employed unbiased chemical etching to reveal evidence of the zeolite crystallization mechanism. This process also provides insights into the intimate structure of a crystal since the weak bonds break first, and the stable, coherent domains dissolve last, which allows for the facile detection of defects within the structure. This study is performed on large crystals of ZSM-5 (MFI) and its siliceous isostructure silicalite-1 grown in a fluoride medium, which allows for clearer visualization of any particularity in the growth process.

## **2.2 Experimental Methods**

### **2.2.1 MFI Zeolite Synthesis and Dissolution Treatment**

*MFI Zeolite Synthesis:* ZSM-5 was synthesized from a gel with molar composition 0.13 TPABr : 1.12  $\text{NH}_4\text{F}$  : 0.015 $\text{Al}_2\text{O}_3$  : 1.0  $\text{SiO}_2$  : 57.87  $\text{H}_2\text{O}$ . First, aluminum sulfate octadecahydrate (98 wt%, Sigma-Aldrich), tetrapropylammonium bromide (98 wt%, Sigma-Aldrich) was dissolved in half of the above molar amount of deionized water to get a clear solution. After that tetraethyl orthosilicate (98 wt%, Sigma-Aldrich) was added under stirring. The resultant mixture was hydrolyzed overnight at room temperature to get a clear monophasic solution. Then the  $\text{NH}_4\text{F}$  was dissolved in another half of the molar amount of the deionized distilled water, and the resultant solution was added slowly into the monophasic solution under mechanic stirring. The resultant gel was vigorously stirred for 1 h, and transferred to a 1000 mL Teflon-lined stainless steel

autoclave. The synthesis was conducted at 150 °C under static conditions. After 7 days of heating, the autoclave was taken out from the oven and quenched immediately in cool tap water. The solids were recovered by vacuum filtration and subsequently washed with deionized water. The solid cake was then recovered and dried at 100 °C overnight. The template was removed by calcination at 550 °C for 12 h with a ramp of 6 °C / min.

Silicalite-1 was synthesized using the same initial reactants and preparation procedure. The molar composition of the initial system was 0.13 TPABr : 0.94 NH<sub>4</sub>F : 1.0 SiO<sub>2</sub> : 19.29 H<sub>2</sub>O. The synthesis was performed at 170°C for 10 days. A post-synthesis treatment similar with the one applied to ZSM-5 was applied.

*Dissolution treatment:* Fluoride medium etching of MFI-type material was carried out in NH<sub>4</sub>F (98.0%, Sigma-Aldrich) aqueous solution using the following procedure: 7.5 g of the parent, calcined ZSM-5 zeolite was dispersed in 200 g of 40 wt.% NH<sub>4</sub>F aqueous solution and was allowed to react at 50 °C for up to 60 min under mechanical stirring and ultrasonic radiation (USC 600 TH, 45 kHz, VWR). Intermediate samples were taken out after set period of reaction time. The etched products were thoroughly washed with deionized water after the fluoride medium treatment. The samples treated by NH<sub>4</sub>F aqueous solution for 20, 40 and 60 min were denoted ZSM-5-20 (568-1), ZSM-5-40 (568-2), and ZSM-5-60 (568-3), respectively.

### **2.2.2 Characterization**

*Powder X-ray diffraction (PXRD):* Measurements were performed on an X'pert Pro PANalytical Diffractometer using Cu K $\alpha$  radiation ( $\lambda = 1.5418 \text{ \AA}$ , 45 kV, 40mA). The samples were studied in the 5-50° 2 $\theta$  range with a scanning step of 0.0167° s<sup>-1</sup>. Nitrogen

adsorption-desorption experiments were performed with a Micromeritics ASAP 2020 automated gas adsorption analyzer. Prior to analysis, the samples were outgassed at 100 °C for 1 h and 300 °C for 12 h. The Si and Al contents are determined by inductively coupled plasma optic emission spectroscopy (ICP-OES) on an OES 5100 VDV ICP from Agilent; all samples are digested in aqua regia and HF prior to the analysis.

*Ex situ scanning probe microscopy:* Atomic force microscopy (AFM) measurements of a ZSM-5 sample was performed on an Asylum Research Cypher ES Environmental instrument (Santa Barbara, CA) equipped with a liquid sample cell. The silicalite-1 crystals were dispersed on quickset Loctite Epoxy (Henkel Corporation), which was affixed on a 15 mm specimen disc (Ted Pella, Inc.). The epoxy was cured in an oven at 50 °C, and after 24 h, the sample disc was removed, cooled to room temperature, and sonicated in DI water to remove loosely bound crystals. The sample disc was then placed in a closed liquid cell. A drop of DI water was deposited on the sample substrate, which in contact with the AFM cantilever (Oxford Instrument, non-coated silicon nitride), generates an aqueous interface for scanning zeolite surfaces. Images of selected untreated crystals were first collected. The sample disc was then treated in 40 wt% NH<sub>4</sub>F solution (NH<sub>4</sub>F salt, Sigma-Aldrich 98%) at room temperature. At 5 min intervals, the sample disc was removed from the NH<sub>4</sub>F solution, washed with DI water, and scanned by AFM. Due to possible debris on crystal surfaces after each treatment, the selected crystals were cleaned in contact mode before the cantilever was exchanged with a new one for actual imaging. Between treatment intervals, the sample disc was kept submerged in DI water. As initially tracked crystals became unbound from the epoxy

after a sequence of treatments, multiple crystals were tracked during the first 60 min of treatment. Images ( $2 \times 2 \mu\text{m}^2$  or  $3 \times 3 \mu\text{m}^2$ ) were collected by moving the cantilever in the x and y-direction on the crystal at set increment. The obtained images were reassembled by overlapping segments to compose an image of a significant portion of the crystal (**Scheme A1**), which allows for *ex-situ* tracking of feature changes as treatment progressed.

*ToF-SIMS*: Sample preparation – The top mount holder is typically used to handle samples that are very thick (few mm) or large (few cm). Samples are held in place using double-face carbon. The sample holder was attached to the transfer arm by means of a bayonet fitting, and then the latter is introduced in the load lock chamber until the vacuum pumping reaches a vacuum of  $5.0 \times 10^{-5}$  mbar, ensuring an appropriate detection limit (few ppm).

Mass Spectroscopy – Positive and negative high mass resolution spectra were performed using a TOF-SIMS NCS instrument, which combines a TOF-SIMS instrument (ION-TOF GmbH, Münster, Germany) and an *in situ* scanning probe microscope (NanoScan, Switzerland) at Shared Equipment Authority from Rice University. A bunched 30 keV  $\text{Bi}_3^+$  ions (with a measured current of 0.15 pA) was used as a primary probe for analysis (scanned area  $300 \times 300 \mu\text{m}^2$ ) with a raster of  $128 \times 128$  pixels. A charge compensation with an electron flood gun has been applied during the analysis. An adjustment of the charge effects has been operated using a surface potential of -120V and an extraction bias of 0 V for the positive polarity and a surface potential of 90V and an extraction bias of -20 V for the negative polarity. The cycle time was

fixed to 90  $\mu\text{s}$  (corresponding to  $m/z = 0 - 737$  a.m.u mass range).

2D imaging – A bunched 60 keV  $\text{Bi}_3^{++}$  ions (with a measured current of 0.3 pA) was used as primary probe for analysis (scanned area  $50 \times 50 \mu\text{m}^2$ ) with a raster of 2048 x 2048 pixels and then binned to enhance the signal-to-noise ratio. Same conditions of charge compensation have been applied in imaging and in spectroscopy. The number of scans has been limited to 5 for preventing the damage induced by a high dose of bismuth ions.

The same areas have been analyzed before and after treatment. Each localized regions of interest have been marked by reference points to provide the highest analysis accuracy in the comparison.

*Electron microscopy:* TEM sample preparation – For the S/TEM analyses, a small amount of dry reaction powder samples were dispersed in distilled water and ultrasonicated for 5 mins to break apart any formed aggregates. A droplet of the resulting suspension was deposited on a TEM grid covered with a thin holey carbon support film.

Using ion milling thin foils for S/TEM imaging were prepared from individual MFI crystals by cutting thin sections perpendicular the  $c$ -axis, following established procedures with a scanning electron microscope/focused ion beam (SEM/FIB) instrument using Ga ion source (Quanta 200i 3D, ThermoFisher Scientific). First, a strap of 5  $\mu\text{m}$  thick protective Carbon layer was deposited over a region of interest using the ion beam. Subsequently, approximately 80 nm thin lamella was cut and polished at 30 kV and attached to a TEM grid using *in situ* Oxford Instrument Autoprobe200

manipulator. To reduce surface amorphization and Gallium implantation final milling at 5 kV and 0.5 nA was used to thin the sample to electron transparency.

Scanning/transmission electron microscopy (S/TEM) – Electron microscopy imaging and analysis were performed at the Central Facility for Advanced Microscopy and Microanalysis at the University of California at Riverside. Scanning/transmission electron microscopy (S/TEM) imaging was performed at 80 and 300 kV accelerating voltages in a ThermoFisher Scientific Titan Themis 300 instrument, fitted with X-FEG electron source, 3 lens condenser system and S-Twin objective lens. High-resolution TEM images were recorded at a resolution of 2048x2048 pixels with a ThermoFisher CETA-16M CMOS digital camera with beam convergence semi-angle of about 0.08 mrad. STEM imaging was performed at 300 kV accelerating voltage in the Titan Themis 300 instrument. STEM images were recorded at probe convergence of 10 mrad with a probe current of 150 pA, using Fischione Instruments Inc. Model 3000 High Angle Annular Dark Field (HAADF) detector at a frame size of 2048 x 2048 pixels, dwell time of 15  $\mu$ sec/pixel, and camera length of 245 mm.

Energy dispersive X-ray Spectroscopy (EDS) analyzes and elemental mapping were obtained in the STEM at 300 kV, utilizing ThermoFisher Scientific SuperX system equipped with 4x30mm<sup>2</sup> window-less SDD detectors symmetrically surrounding the specimen with a total collection angle of 0.68 srad, by scanning the thin foil specimens. Elemental mapping was performed with an electron beam probe current of 550 pA at 1024 x1024 frame resolution.

Scanning electron microscopy (SEM) – SEM and energy-dispersive X-ray

spectroscopy (EDS) was used to characterize the morphology and elemental composition of each sample using a ThermoFisher Scientific Co. NovaNano SEM450 equipped with Oxford Instruments Inc, Aztec Synergy energy dispersive X-ray spectrometer (EDS) fitted with a X-Max50 50 mm<sup>2</sup> SDD detector with an energy resolution of 129 eV at MnK $\alpha$ . SEM images were acquired using the secondary and backscattered electron mode with a dedicated detector at 2, 5, and 15 kV accelerating voltages.

### 2.3 Results and Discussion

Powder XRD analysis showed that both ZSM-5 and silicalite-1 are highly crystalline (**Figure A1**). Inspection by SEM revealed that the ZSM-5 crystals are uniform in size and approximately 100  $\mu\text{m}$  in length (**Figure A2**). The majority of crystals have well-defined morphology with the typical coffin shape (**Figure 2.1a**), and a few agglomerates can be observed. The N<sub>2</sub> adsorption-desorption isotherm is type I, which is characteristic of microporous materials. The micropore volume of zeolite ZSM-5 is 0.16 cm<sup>3</sup>/g (**Figure A3**), a value typical for a highly crystalline MFI-type material.

A close view presenting the surface features of ZSM-5 crystals is shown in Figure 1D. Different levels of crystal etching, from the as-synthesized sample until later times when the initial crystal morphology is indiscernible, are presented on Figure 1C-F, where one can see that the changes due to dissolution. Thus, after 30 min treatment, only the interface between well-defined intergrowths composing one zeolite crystal is dissolved. For instance, **Figure 2.1b** shows the dissolved interface between two contact twins oriented 180° relative to each other. **Figure 2.1c** shows the dissolution of the

interface between the parent crystal and the surface twins turned at 90°. After 60 min treatment, deeper dissolution reveals interior elements building the “single” crystals (**Figure 2.1d**); and after 120 min etching, only fragments of the crystal remain where cavities with rectangular morphology can be seen (**Figures 2.1 e, f**). These observations show that the dissolution process is guided by distinct crystallographic zones, namely the interface between the twin crystals if one considers the macro morphological features of the zeolite (**Figures 2.1b-d**). At a local level, the dissolution still follows particular crystallographic directions since dissolution pits exhibit rectangular parallel borders. It should be noted that the crystal core is more extensively dissolved than the peripheral regions of the crystals. In order to better understand the phenomenon controlling the dissolution process, complementary imaging methods were employed.

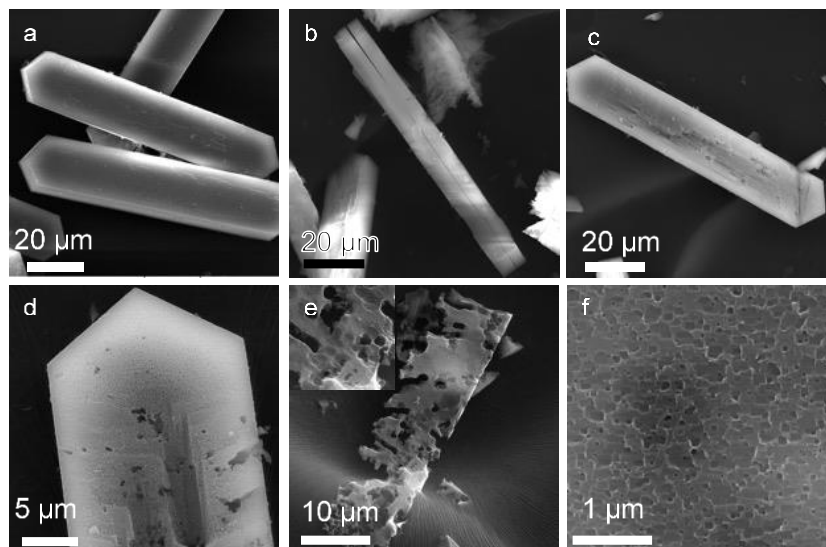


**Figure 2.1.** Scanning electron micrographs of (a) parent crystals; (b) after 30 min dissolution; (c, d) after 60 min treatment; (e, f) after 120 min treatment.

Atomic force microscopy (AFM) was used to examine time-resolved changes in surface topography during crystal dissolution. Conducting *in situ* measurements was

challenging due to the debris generated at the interface; therefore, we employed an *ex situ* protocol (**Scheme A1**) wherein the same surface of a zeolite crystal was imaged after various intervals of  $\text{NH}_4\text{F}$  treatment (**Figure A4**). After each interval of acid treatment, a series of AFM images were taken over an entire (010) surface and combined into a composite figure (**Figures A4 and A5**), where specific regions could be evaluated to track distinct changes in surface features with time. There were three general types of features observed in AFM images: crevices, etch pits, and spheroidal domains. The generation of crevices (**Figures 2.2a – c**) seem to originate at (100) edges of the crystal and propagate inward with temporal increases in crevice width and depth (s). Multiple *ex situ* images of the crystal surface were compiled in Movie S1 where periodic snapshots during 60 min of treatment (**Figures 2.2e – j**) reveal significant changes in surface topography. The initially rough surface of the untreated crystal becomes relatively smooth after 10 min of treatment due to the removal of large features; and with prolonged treatment, AFM images reveal the emergence of crevices and etch pits. Similar to FE-SEM images in Figure 1, we observe heterogeneous surface topographies with prolonged dissolution time. Some regions remain relatively smooth with less evidence of dissolution, whereas other regions develop highly roughened or pitted surfaces (**Figure A6**). Images after 45 min of treatment (**Figure 2.2i**) show the presence of spheroidal domains and etch pits that become enlarged with further treatment (**Figure 2.2j**). The size distribution of etch pits after 60 min of acid treatment is shown in **Figure A7**. The AFM analysis demonstrates inequivalent spatial dissolution of the zeolite crystal surface, which is not related with the framework composition since this series of

experiments was performed on silicalite-1 crystals. Thus, surfaces exhibiting disproportionately high rates of dissolution is attributed to zeolite crystal imperfections (i.e., defect zones present on crystal facets).

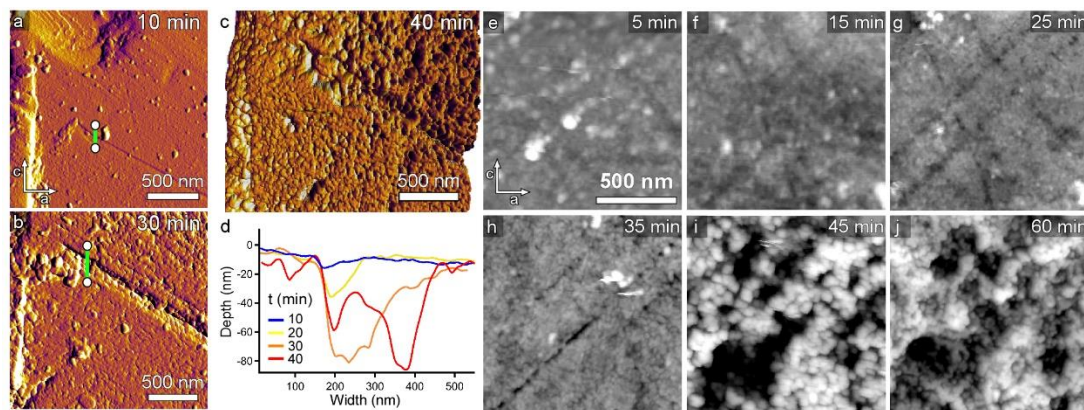


**Figure 2.2.** (a – c) Time-elased images (10 – 40 min of treatment). (c) 3D rendering of overlapping height and amplitude images. (d) Height profiles along the green lines (data are normalized to the baseline). (e – j) Height images of a different surface (5 – 60 min of treatment).

Later stages of dissolution, when etch pits became too deep for analysis by AFM, were studied using a combination of SEM, TEM, and STEM. Representative images of ZSM-5 and silicalite-1 crystal dissolution after 30 and 60 min are shown in Figures 3a-c and 3d-f, respectively. The backscattered-electron (BSE) image of ZSM-5 (**Figure 2.3a**) and TEM bright field image of silicalite-1 (**Figure 2.3d**) both reveal zonal growth patterns. In particular, the hour-glass feature suggests sectorial growth starting from the center of the crystal. Electron microscopy (**Figure 2.1b**) showed that the dissolution along the interface between the 90° and contact twin in MFI crystals is due to the presence of highly defected zones between the individual crystals; however, the origin of small etch pits with pseudo-hexagonal shape formed deep within the core of the crystals from SEM images of {010} surface (**Figures 2.3b,e**) is not immediately obvious. HAADF HR-STEM image along the <010> axis (**Figure 2.3c, f**) shows the

dark spots in the structural images correspond to the channels in the structure, and the bright lines are the SiO<sub>4</sub> tetrahedral chains. The orientation of the traces of the {001} and {101} planes are marked with red lines.

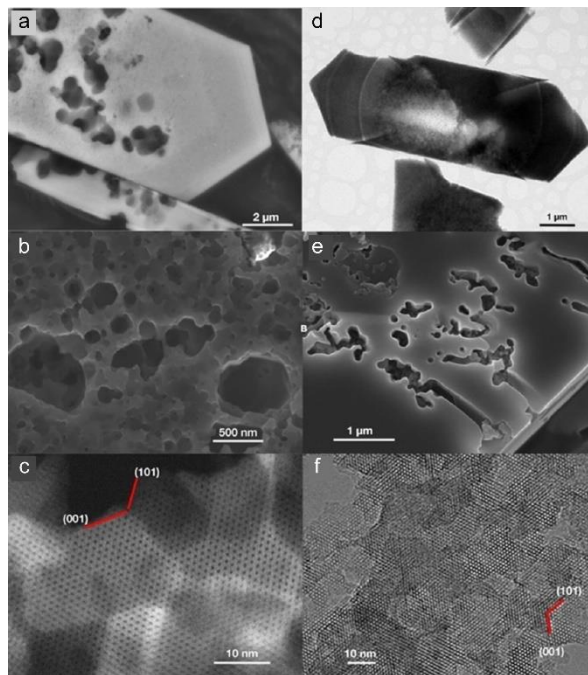


**Figure 2.3.** Dissolution uncovers the history of ZSM-5 (a, b, c) and silicalite-1 (d, e, f) crystallization.

In a previous study, we suggested that the mosaic of etch pits might be due to the dissolution of misoriented crystalline domains. Here, this hypothesis is verified by HRTEM imaging down the *c*-axis of ZSM-5 crystal. As shown in Figure 4, thin electron transparent lamellas were cut perpendicular to the *c*-axis by focused ion milling from two different parts of the same crystal. The first lamella was cut from the peripheral region of the crystal close to the apical tip (**Figures 2.4a, c, e**), labeled as lamella “I” in the inset of **Figure 2.4**. The second, was cut from the central part of the crystal (**Figure 2.4d, f**) and is labeled as lamella “II”. The crystal structure and order in lamella I appears

perfect with no significant defects or distortions (**Figure 2.4a**), confirmed also by the sharp bright spots in the corresponding fast Fourier transform (FFT) pattern (**Figure 2.4c**). In contrast, closer inspection of HR-TEM images of lamella II reveals the existence of a mosaic structure in the center of the crystal that is comprised of fine domains slightly misoriented with respect to each other by minor mutual rotation within the plane of imaging. The fine domains are confirmed by both dark-field contrast imaging (**Figure 2.4e**) utilizing (020) reflections as well by the shape and size of the (010), (020) and (200) reflections in the FFT pattern (**Figure 2.4f**). The diffuse character of the spots in **Figure 2.4f** can be attributed to misorientation between the fine domains in this region of the crystal. A comparison between the same type of reflections (marked by white arrows in **Figure 2.4c and f**, respectively) demonstrates the difference in crystalline ordering of the peripheral and central parts of the crystal. The sharp character of the FFT spots in **Figure 2.4c** is clear evidence of a defect-free structure as opposed to the mosaic domain structure revealed in **Figure 2.4f**.

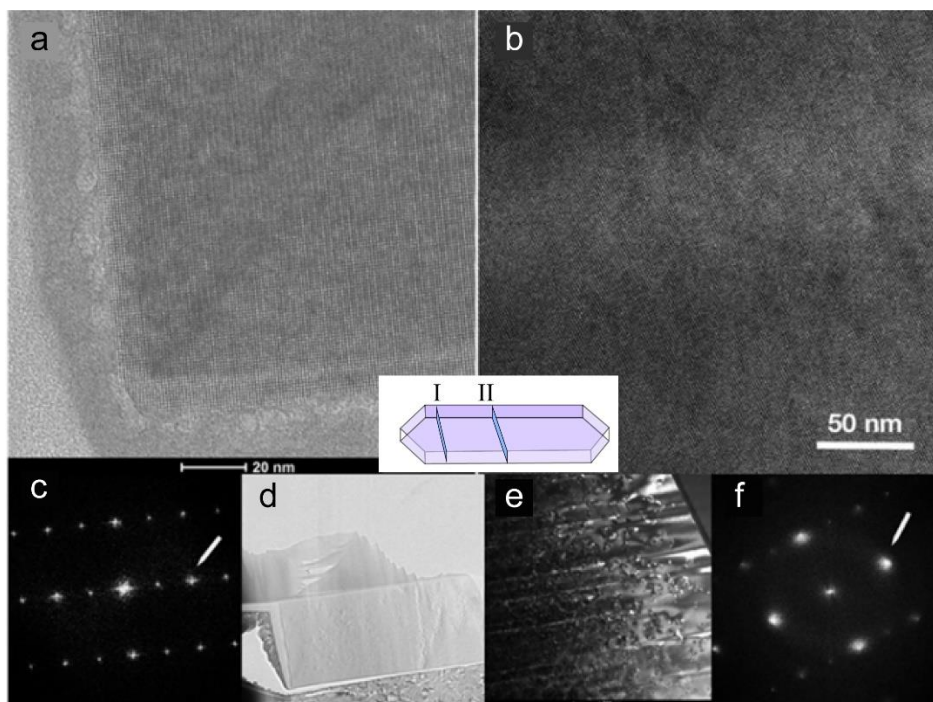


**Figure 2.4.** (a, b) HRTEM images down the  $c$ -axis from a foil from the periphery (I) and the central part (II) of the crystal. (c, f) FFTs from the lattice images in (I) and (II), marked (020) reflections. (d,e) Low magnification TEM dark-field image from the foil (I) and (II).

The above interpretation is further corroborated by cutting a thin FIB section perpendicular to the  $c$ -axis from the middle of another ZSM-5 crystal (**Figure A10**) The mis-orientation between adjacent domains is minor and difficult to discern directly from HRTEM images. As such, the same digital processing was applied to the images of the middle and the periphery of the foil (cut from central part of untreated ZSM-5 crystal) to enhance the contrast. First, FFT was applied to the HRTEM images to obtain the patterns shown in **Figures A10c and d**, then a circular filter was applied to select only the reflections up to (200) and (020) in the FFT patterns (insets in **Figures A10c and d**). Inverse FFT processing of the aforementioned filters resulted in the images shown in **Figures A10a and b**. The uniform appearance of the filtered inverse-FFT image in

**Figure A10b** (i.e., the lack of contrast variation across the lattice fringes), in comparison to the nonuniformity of the image of the central part (**Figure A10a**), confirms the defect-free nature of the peripheral parts of the ZSM-5 crystals. This is consistent with the sharp reflections seen in the FFT pattern from the periphery (**Figure A10d**) compared to the more diffused appearance of the FFT reflections (**Figure A10c**) from HRTEM image of the central region. Fine domains between 10 and 25 nm in diameter are visualized by HRTEM imaging after processing in the central part of the thin foil (**Figures A10a and c**), revealing the mosaic structure of the central region of ZSM-5 zeolite crystals due to minor mis-orientation of neighboring domains. Such domains are missing in the periphery of the foil (**Figures A10b and d**), showing perfect structure.

The difference in dissolution of the peripheral and central parts of the crystal is also observed by chemical mapping via time-of-flight secondary ion mass spectrometry (ToF-SIMS) of untreated silicalite-1 crystals (**Figures A9a-d**) compared to those after 60 min of treatment (**Figures A9e-h**). The trace quantity of the organic structure-directing agent (tetrapropylammonium, TPA) provides a high contrast wherein the tracking of TPA ion fragments in the crystal before and after treatment (**Figures A9b and f**, respectively) reveals regions of dissolution. Similar information with less sensitivity can be gleaned from ToF-SIMS mapping of  $\text{SiO}^+$  (**Figures A9c and g**) and  $\text{Si}_2\text{OH}^+$  (**Figures A9d and h**) ions, which reveal a difference in Si-O bonds and terminal silanol groups between the peripheral and central regions of the silicalite-1 crystals. In addition, we used *ex-situ* AFM to monitor the evolution of spheroidal domains during acid treatment of a silicalite-1 (010) surface. High-resolution images of a fixed area on

the crystal surface (**Figures 2.5a-d**) reveals the progressive appearance of small spheroidal domains that seemingly dissolve at a much slower rate than the surrounding regions (**Figure 2.5g**). Similar features were observed in multiple regions of several crystals during AFM measurements (e.g., **Figure 2.2i**). Analysis of height images for several crystals in a single dissolution experiment reveals a distribution of spheroidal feature sizes (**Figure 2.5i**) with an average diameter of 15 nm. This is consistent with the domain sizes determined by HRTEM imaging (**Figure A10**) corresponding to interior regions of the crystal where more defects are observed.

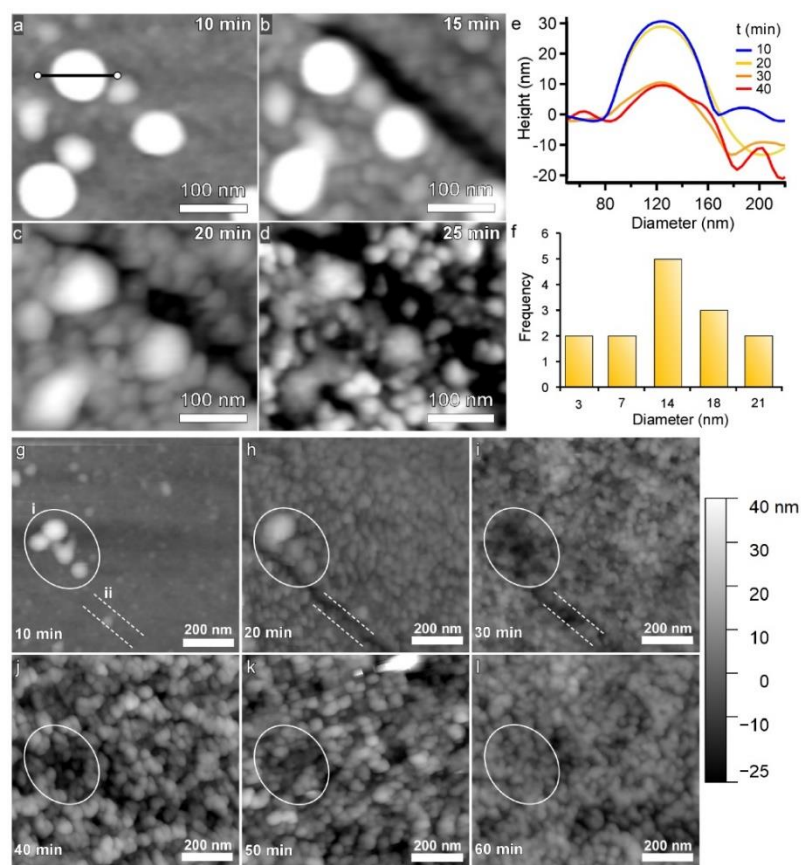


**Figure 2.5.** (a – d) AFM height images of a fixed area on a silicalite-1 (010) surface (10 – 25 min treatment), (g – l) another area (10 – 60 min treatment) (e) Height profiles of a feature in AFM. (f) A distribution of spheroidal feature diameters (n = 17 measurements).

The MFI zeolite crystal growth pattern is clearly revealed by the dissolution experiments. As shown in **Figures 2.3 and A9**, the interior regions of the crystal dissolve much more rapidly than the periphery. Furthermore, TEM imaging clearly reveals an “hour-glass” feature in the center of majority of partially-dissolved crystals. This hour-glass zone is overgrown by zonal features (**Figure 2.3a and b**). The above observations are evidence of two-stage crystal growth where the growth mechanism has changed from sectorial to zonal growth over the course of crystallization.

AFM imaging (**Figure A4**) also confirms the presence of non-uniform regions (micron-size areas) where dissolution is more prevalent in some locations, whereas others are less affected by acid treatment. Time-resolved analysis of the silicalite-1 (010) surface during dissolution also reveals dynamic sequences of emerging and disappearing features leading to either smooth or rough surface topography. For example, AFM height images of a fixed area over a 60-min period of dissolution (**Figures 2.5g-l**) and corresponding amplitude images (**Figure A8**) reveal the initial presence of large protrusions (highlighted by the dashed oval) that disappear with treatment time to yield an interface with either flat regions or spheroidal features.

The applied approach has allowed us to reveal critical details about the dissolution process and in turn about the structure of the studied MFI zeolites as well as the crystal growth mechanism. The following conclusions can be drawn regarding the dissolution process. Dissolution is selective for regions with higher densities of defects, which are non-uniformly distributed throughout the crystal. Ammonium fluoride attacks predominantly the central parts of the MFI-crystals and affects the periphery of crystals

at a significantly lesser extent. Our analyses have shown that the crystals are chemically homogeneous and structurally, on a micron-scale level, are faceted crystals with some degree of twinning.

The studied silicalite-1 samples are essentially built up of tetrahedral  $\text{TO}_4$  sites (T = Si), where all oxygen atoms are shared by adjacent tetrahedra. Hence, there is relatively no structural anisotropy in the bond strength across individual tetrahedra, which can affect the dissolution process [164-167]. The main factor that would affect Si-O bond strength is protonation, although since it is structurally homogeneously distributed across the structure, it should not affect the dissolution process selectively. Consequently, the presence of defects on atomic and unit cell levels though, can introduce inhomogeneity and affect selective bonding among the  $\text{SiO}_4$  tetrahedral framework. Our observations suggest that the dissolution starts at defect sites with strained Si-O bonding, such as point defects, dislocations, twin boundaries, and low-angle grain boundaries. It proceeds by expanding around initially formed dissolution pits. The dissolution advances parallel to low-index atomic planes with small reticular density, which seemingly follows a reverse Bravais-Friedel-Donnay-Harker growth law at a localized level. The crystal periphery appears to be the most stable, which accounts for our observation that this region dissolves at a much slower rate. In the late stages of zeolite formation, the growth rate is relatively slow and likely accounts for the presence of fewer defects in peripheral crystal zones, thereby leading to higher structural order in these regions (**Figures 2.3, 2.4, and 2.5**).

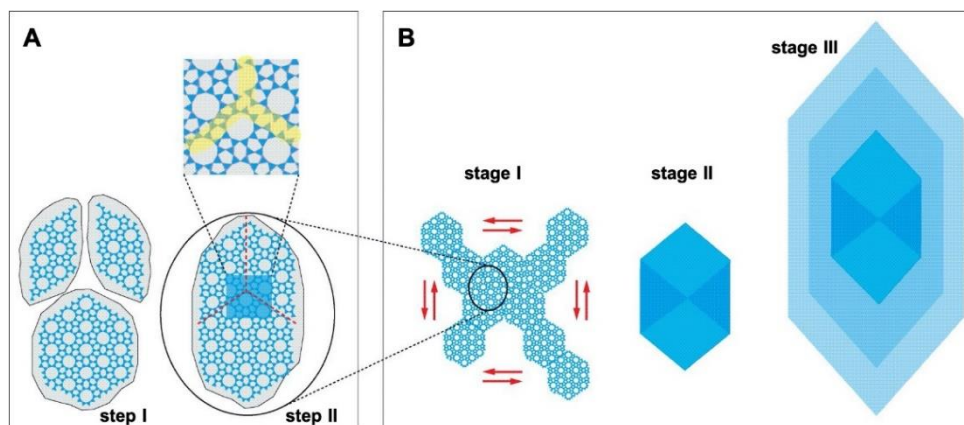


**Figure 2.6.** Interpreted scheme of (a) 2 steps incubation process: (1) formation of proto-particles with MFI structure; (2) fusion to form nuclei. (b) The growth process has 3 distinct stages: (1) skeletal growth, (2) sectorial growth, and (3) final zonal overgrowth.

Our previous study of zeolite LTA showed that nucleation occurs within agglomerates of amorphous (alumino)silicate precursors [153]. The latter coalescence with synthesis time into larger particles with a crystalline structure and an overall size of a few to tens of nanometers, forming stable nuclei that can interact and fuse with other nuclei throughout the crystallization process (**Figure 2.6a**). A similar process for MFI-type zeolite was reported [179] using cryo-TEM to track various stages of nucleation to confirm growth by a nonclassical multi-step mechanism [180]. During the coalescence of crystals, the formation of domain boundaries (marked by red dashed lines in **Figure 2.6a**) is proposed where the fast fusion between nanocrystals creates a mismatch between the crystalline structure of each particle. The process is statistical in nature; some of the discrepancies and distortions that have higher interface energy are eliminated by minor re-arrangements; others are sealed and preserved as fine-size domains through the subsequent stages of crystal growth. Some of these intergrowing domains give rise to twin relationships and likely serves as a starting point for twin

growth; others have mismatch that leads to low-angle domain boundaries, dislocations, and point defects. The vacancies between crystalline domains can be sealed by the addition of low molecular weight (alumino)silicates (i.e., monomer or oligomers) through crystallization by particle attachment involving the addition of amorphous precursors. The central region of the zeolite crystal forms fast due to a high initial supersaturation (including amorphous precursors and soluble species) and a large number of crystallites present, which tends to concentrate a high level of defects. Crystallization by particle attachment is prone to defect incorporation, particularly when the added particles must subsequently undergo structural rearrangement, which may be incomplete. Moreover, nonclassical pathways involving the addition of amorphous precursors can also lead to defects if the disorder-to-order transition is either incomplete or results in misoriented crystalline domains.

Many of the observations from our study of MFI dissolution are consistent with the processes of zeolite crystallization outlined above. Preferential dissolution at the center of the crystal agrees with the higher number of defective zones created during the early stages of zeolite formation via the agglomeration of MFI nanocrystallites. Consequently, the central part of the crystal is more vulnerable to etching and dissolves more rapidly. The zeolite formation in the studied system is a complex multistage process, as the mechanism of growth is a function of the supersaturation, which differs in the early and late stages. It can be speculated that the initially formed nuclei rapidly form skeletal structure along the  $\langle 101 \rangle$  directions (stage 1 in **Figure 2.6b**), setting up the growth process of the subsequent stage 2 that proceeds by sectorial growth

originating from the skeletal structures formed in stage 1 (stage 2 in **Figures 2.6b and 2.3d**). This is facilitated further by the high concentration of nuclei present in the solution. The final stage is marked by a lower concentration of reactive species and a slower growth rate, leading to peripheral regions with fewer defects that exhibit slower rates of dissolution. The large size of the crystallites formed already predetermines zonal layer-by-layer growth [181] following rapid nucleation and growth in the crystal core. The participation of the pre-formed particles, which we evaluated to be in the range of 5 to 25 nm (**Figure 2.5f**), is limited during the late stage of zeolite growth. The growth and dissolution are competing processes resulting in the final crystal form faceted by low index slow-growing faces.

#### **2.4 Summary**

There are different types of defects in a zeolite crystal. For instance, the zones between the individual crystals in twin crystals or an agglomerate of intergrown crystals are rich in defects since the crystal faces are not terminated and contain a large number of surface hydroxyls (not all of which form Si-O-Si bonds during coalescence). The mismatch between crystal planes of intergrown crystals also generates strain on the crystal lattice, making these regions more vulnerable to chemical attack. The present study shows that zeolite MFI crystals contain small (several tens of nm), misoriented domains with low-angle grain boundaries, which represents defect zones that are more susceptible to dissolution. Finally, zeolite MFI crystals contain point defects (i.e., missing T atoms) that can serve as initiation sites for dissolution. Zeolite MFI crystals may contain all defect types; however, the dominant type of defects and its

corresponding concentration and spatial distribution are highly dependent upon the “history” of the growing crystals. The stochastic nature of zeolite nucleation and crystal growth lead to particles containing disparate populations of structural defects. The initial period of rapid nucleation in highly supersaturated media generally increases the probability of high defect density within the interior of zeolite crystals, whereas slower growth rates occurring by classical crystallization at later stages of synthesis (i.e., when the nutrient pool is depleted) leads to fewer defects. Thus, the memory of the growth process is coded in the crystal, and the method employed in this study using dissolution enables the recovery of a zeolite’s growth history.

This study has shown that studying dissolution reactions can be used successfully as a powerful tool that can shed light on the processes of nucleation and growth down to atomic scale level, which in hydrothermal systems are difficult to assess by the presently available *in situ* methods. Furthermore, the available *in situ* methods are in principle either of bulk nature or only capable of providing resolution at essentially micron or larger scale which prevents direct assessment of the growth process. In addition, more general implication of our observations concerns the mosaic structure in crystals that has been known for long time [182], but no direct correlation of its effect on the growth mechanism of microcrystals has been demonstrated up until now.

## CHAPTER 3

### Engineering Silicon-zoned Zeolite Catalysts to Address Intrinsic Mass

#### Transport Limitations

The materials discussed in this chapter will be published in a peer reviewed journal. Figure and table labels are reformatted to be consistent with dissertation formatting requirement. The work was done in collaboration with Dr. Wei Qin from the University of Houston, Dr. Conan Weiland from Brookhaven National Laboratory, Dr. Simon R. Bare from SLAC National Accelerator Laboratory, and Nikolaos Nikolopoulos, Dr. Donglong Fu, and Prof. Bert Weckhuysen from Utrecht University.

#### 3.1 Prior Work on Establishing Structure-Performance Relationship for Zeolites in MTH

The materials discussed in this section have been published in peer reviewed journals. Figure and table labels are reformatted to be consistent with dissertation formatting requirement. The work on ZSM-5 and ZSM-11 is initiated by former group member Dr. Yufeng Shen in collaboration with Dr. Donglong Fu, Dr. Joel E. Schmidt, and Prof. Bert Weckhuysen from Utrecht University. The work on SAPO-34 was done in collaboration with Dr. Andrew Hwang and Dr. Aditya Bhan from the University of Minnesota.

Regarding the development of structure-performance relationships, it is critical to properly account for (and ideally control) the physicochemical properties of zeolite catalysts. For instance, it is difficult to evaluate the effect of one property (e.g., Si/Al ratio) when others (e.g., crystal size, shape, mesoporosity, or percentages of Al species) are not fixed. Preparing a set of zeolite catalysts where one property is systematically varied while keeping all others constant is nontrivial, yet subtle variations in zeolite properties can have a significant impact on catalyst performance. In order to facilitate comparison among different data sets, it would be advantageous to develop a descriptor that can account for a broad set of physicochemical properties, many of which are correlated with mass transport. However, initial establishment of these descriptors still

necessitates generation of model zeolites with well-controlled properties to facilitate derivation of trends (or lack thereof). As such, in the two separate studies briefly summarized here, we have utilized a set of zeolite catalysts with well-controlled properties to deconvolute the contributions of different framework topology and crystallite size to diffusional constraint and its effect in MTH reaction on (i) ZSM-5 (**MFI**) and ZSM-11 (**MEL**) and (ii) SAPO-34 (**CHA**).

The first work is a systematic study of mass transport limitations imposed by the zeolite pore topology and diffusion pathlength. These two factors are independently assessed via MTH reactions and operando UV-vis study for a set of ZSM-11 and ZSM-5 zeolites with carefully controlled properties. The set of ZSM-11 catalysts have consistent physicochemical properties, but with increasingly smaller crystallite size, whereas the ZSM-5 crystal has similar SEM measured size to that of a ZSM-11, but with different pore topography. The direct comparison of ZSM-5 and ZSM-11 of similar crystal size (from SEM measurements) show a 2-fold increase in catalytic lifetime (from conversion versus time-on-stream data) owing to the straight channels of the **MEL** framework which can better facilitate molecular diffusion. Furthermore, a decrease of ZSM-11 crystal size from 750 nm to 150nm also resulted in an 8-fold increase in catalyst lifetime. Another method of assessing diffusion is also employed to look at mass transport properties of the set of catalysts. Transient sorption experiment with probe molecule (2,2-dimethylbutane) followed by fitting of sorption curve with spherical diffusion model allow for extraction of the characteristic diffusional timescale ( $D/R^2$ ). The  $D/R^2$  values measured for this set of samples reveal a disparity between measured

SEM size and diffusion properties. Notably, although both the ZSM-5 and ZSM-11 have similar SEM measured size, defined as the average distance in the [100] and [010] directions, they have different  $D/R^2$  values, with ZSM-5 having the lower value, consistent with our suggestion that sinusoidal channels can impose increased diffusion constraint. Finally, we also established a linear correlation between increased  $D/R^2$  value (better mass transport) with increased catalyst lifetime (**Figure 3.1a**).

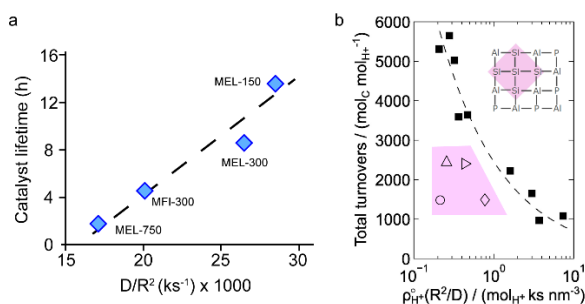


**Figure 3.1.** (a) Plot showing the apparent correlation between the characteristic diffusion timescale  $D/R^2$  and catalyst lifetime. The dashed line is interpolated to guide the eye. (b) Total turnovers versus a descriptor that accounts for diffusional constraints.

In another study of SAPO-34 catalysts for methanol-to-olefins (MTO) reactions, we prepared a set of SAPO-34 samples diverse in morphology and composition. Here, we utilize  $D/R^2$  as a functional assessment of averaged size, more sensitive to both morphological discrepancies and intracrystalline defects compared to common measurements from SEM micrographs. Using a single descriptor,  $\rho_{\text{H}^+}^{\circ}R^2/D$ , which accounts for acid site densities and diffusion properties, we showed that catalytic lifetime (total turnovers) decreases monotonically with increased  $\rho_{\text{H}^+}^{\circ}R^2/D$  for samples with isolated SI speciation (**Figure 3.1b**). On the other hand, at identical  $\rho_{\text{H}^+}^{\circ}R^2/D$  values, samples with siliceous islands (**Figure 3.1b**, open symbols in pink region) have lower total turnovers compared to those with uniquely  $\text{Si}(\text{OAl})_4$  speciation. This trend

is consistent with reported effects of crystallite size, site density, textural properties, and speciation on catalytic lifetime of SAPO-34 for MTO reactions. This combined descriptor is representative of diffusional constraints resulting from crystallite size, acid site density, and Si speciation. The effect of these properties are all manifestations of diffusional constraints. Comprehensive reaction-transport analysis of different reactions within the MTO complex network illustrate that the total turnovers decrease as a result of diffusional constraints regulated by  $\rho_{\text{H}^+}^{\circ} R^2/D$  or Si speciation, and this decrease in catalytic performance is due to the different impacts diffusional constraints have on dehydrocyclization reactions compared to olefins methylation, methanol transfer hydrogenation, and aromatics dealkylation.

These two studies illustrate the advantage in employing descriptors to account for different physicochemical properties of zeolite catalysts. Descriptors such as these facilitate side-by-side comparison of catalysts and corresponding reaction data in the literature by accounting for variance in catalyst properties. It remains to be determined what descriptors are most universal, although we posit there may be a need for multiple descriptors to account for the large diversity of zeolite properties. Nevertheless, such approaches have the added benefit of identifying possible defects in zeolite catalysts that are otherwise difficult to detect by conventional characterization techniques. Moreover, universal implementation of this approach would help establish robust structure-performance relationships in zeolite catalysis.

### **3.2 Motivation**

The high thermal stability, tunable acidity, and shape selectivity of nanoporous

aluminosilicate zeolite catalysts have led to their extensive use in commercial processes [28]. A common objective in zeolite catalyst optimization is to minimize mass transport limitations through the design of either nano-sized or hierarchical materials using a range of (post-)synthesis approaches to reduce the internal diffusion path length [5, 33-41]. Similar outcomes can be achieved by increasing access to external pore openings through the preparation of pillared [5, 183] or finned [7] zeolite catalysts; however, comparatively fewer studies [19, 125-127, 130, 131] have examined the impact of spatial gradients in zeolite composition (Si/Al ratio) on mass transport properties and their concomitant effects on catalyst performance. The spatial distribution of aluminum in zeolites is oftentimes considered to be homogeneous; however, non-uniform distributions of aluminum can exist [18, 19, 121, 184, 185]. Aluminum zoning (**Figure 3.2a**) is the most frequently observed wherein aluminum is disproportionately concentrated in the exterior rim of the zeolite particle. This phenomenon was first reported in large ZSM-5 crystals (80  $\mu\text{m}$ ) by von Ballmoos and Meier [121]. Multiple research groups [18, 19, 184, 185] have observed similar aluminum enrichment in the exterior of ZSM-5 crystals using various techniques to map elemental composition, such as focused ion beam (FIB) combined with energy dispersive X-ray spectroscopy (EDX), synchrotron-based micro X-ray diffraction, and controlled desilication treatment.

The alternative and less commonly reported configuration is silicon zoning wherein the exterior rim of ZSM-5 crystals is enriched in silicon (**Figure 3.2a**) [186]. The shape selectivity of zeolites is derived from Brønsted acid sites located within the confined pore network [187]. It has been demonstrated by Mobil, DuPont, and others that post-

synthesis modification of ZSM-5 catalysts with a siliceous exterior (or passivated surface) eliminates non-selective reactions on external surfaces (e.g., enhanced *para*-xylene selectivity for xylene isomerization) [188-191] or generates a hydrophobic exterior that is beneficial for selected applications (e.g., conversion of biomass to chemicals and fuels) [192, 193]. Different methods have been reported in the literature to passivate external Brønsted acid sites (e.g., chemical deposition of passivating agents); however, these methods often require multistep post-synthesis treatment and often sacrifice catalyst activity via pore blockage (i.e., increased mass transport limitations) [194, 195]. Post-synthesis dealumination can be used to remove exterior Al sites, but this method has deleterious and/or unintended side effects (e.g., generation of defects or mesopores, respectively) [196, 197]. In a previous study [22], we have developed a systematic method to prepare ZSM-5@silicalite-1 core-shell catalysts where silicalite-1 shells of tunable thickness are epitaxially grown on ZSM-5 crystals. This approach passivates exterior surfaces without blocking pore openings, thus allowing for improved selectivity without sacrificing catalyst activity; however, it requires a multistep synthesis procedure that is impractical for industrial applications. To this end, it is desirable to produce Si-zoned ZSM-5 via a one-pot synthesis method.

There is a resurgent interest in characterizing the spatial distribution of acid sites in zeolites. The vast majority of these studies have focused on isolated or paired Al siting in zeolite frameworks and their catalytic consequences [71, 198]. These variations in composition are at a local level, whereas zoning refers to mesoscopic gradients in composition. There are few studies of zoning, while its impact on catalyst performance

is largely unexplored. In this study, we report methods of preparing both Si- and Al-zoned ZSM-5 via one-pot syntheses based on the judicious selection of organic/inorganic structure-directing agents. We establish catalytic structure-performance relationships in methanol-to-hydrocarbons (MTH) reactions for zoned H-ZSM-5 catalysts and those with homogeneous Al distribution where distinct trends emerge when introducing an experimentally-derived descriptor that takes into account three critical physicochemical properties: mass transport, acid site concentration, and surface area. Our findings reveal that the introduction of a siliceous outer layer on Si-zoned ZSM-5 catalysts leads to an unexpected and dramatic improvement in mass transport properties with concomitant enhancement in catalyst performance (i.e., lifetime and turnovers) and alteration of the catalytic cycles of MTH reactions. These conclusions are drawn from both one-pot syntheses of zoned materials and core-shell analogues obtained by secondary growth where it is shown that spatial gradients in chemical composition can be used as an effective parameter to optimize zeolites.

### **3.3 Experimental Methods**

#### **3.3.1 Materials**

The following reagents were purchased from Sigma-Aldrich: colloidal silica (LUDOX SM-30), tetraethyl orthosilicate (TEOS, 98%), aluminum isopropoxide (AIP, 98%), sodium hydroxide pellets (NaOH, 98%), sodium hydroxide solution (NaOH, 1 mol/L), sodium chloride (NaCl, 99.5%), potassium chloride (KCl, 99%), silica gel (Davisil Grade 636, 35-60 mesh size), and pyridine (99.8%, anhydrous). The following reagents were purchased from Alfa Aesar: sodium aluminate ( $\text{NaAlO}_2$ , technical grade)

and tetrapropylammonium hydroxide (TPAOH, 40%). Additional reagents used for the synthesis of ZSM-5 include fumed silica (Cab-O-Sil M-5, Spectrum Chemical). Deionized (DI) water was produced with an Aqua Solutions RODI-C-12A purification system (18.2 M $\Omega$ ). All reagents were used as received without further purification. For reaction testing, methanol was purchased from Sigma Aldrich (ChromaSolv, 99.9%), and argon, oxygen and nitrogen gases were purchased from Matheson with UHP grade (99.999%).

### 3.3.2 Synthesis and catalyst preparation of ZSM-5 zeolites

The ZSM-5 zeolites using an OSDA-based method were synthesized from a growth solution with a molar composition of 24 TPAOH: 100 SiO<sub>2</sub>: 1.25 Al<sub>2</sub>O<sub>3</sub>: 0.4 Na<sub>2</sub>O:  $x$  NaCl (KCl): 1920 H<sub>2</sub>O: 400 EtOH, where  $x$  was varied between 0 to 12. NaOH, NaCl/KCl (if necessary), and TPAOH were mixed with DI water followed by the addition of the silica source, colloidal silica (SM30). EtOH were added to the mixture before the aluminum source, AIP, was introduced. The mixtures were aged at room temperature for 24 h under continuous stirring. The growth solutions were then placed in a Teflon-lined stainless steel acid digestion bomb (Parr Instruments) and heated at 100 °C under autogenous pressure for 72 h.

The synthesis of ZSM-5 zeolites in a medium of fixed total SDA content (Na<sup>+</sup> and TPA<sup>+</sup>) was performed using a growth solution with a molar composition of  $x$  TPAOH: 100 SiO<sub>2</sub>: 1.67 Al<sub>2</sub>O<sub>3</sub>: (32- $x$ ) NaOH: 4570 H<sub>2</sub>O (where  $x = 0 - 28.8$ ). The ZSM-5 zeolites using the same method with a fixed total inorganic SDA content (Na<sup>+</sup> and/or K<sup>+</sup>) were synthesized from a growth solution with a molar composition of  $x$  TPAOH:

100 SiO<sub>2</sub>: 1.67 Al<sub>2</sub>O<sub>3</sub>: (32-*x*) NaOH: *x* NaCl or KCl: 4570 H<sub>2</sub>O (where *x* = 7.4 – 28.8). The reagents NaOH, TPAOH, NaCl (and KCl), and the aluminum source (NaAlO<sub>2</sub>) were mixed with DI water followed by the addition of the silica source (colloidal silica SM30). The mixtures were aged at room temperature for 1 h under continuous stirring. The growth solutions were then placed in a Teflon-lined stainless steel acid digestion bomb (Parr Instruments) and heated at 190 °C under autogenous pressure for 24 h.

The synthesis of core-shell ZSM-5 follows a previously published protocol[22]. Shell growth solution of 14 TPAOH: 17 SiO<sub>2</sub>: 9500 H<sub>2</sub>O is chosen to generate the thinnest shell. Similarly, synthesis of inverse core-shell zeolites involves the use of a silicalite-1 core, generated using a growth solution 0.3 TPAOH: 1 TEOS: 35 H<sub>2</sub>O based on a published protocol [199]. The synthesis was performed at 170°C for 3 d. The aluminum containing shell is grown using the following molar composition of 20 TPAOH: 4 Na<sub>2</sub>O: 100 SiO<sub>2</sub>: 2.5 Al<sub>2</sub>O<sub>3</sub>: 4000 H<sub>2</sub>O. The growth solution was aged for 2 h before silicalite-1 core was added to get a 10 wt% suspension. The synthesis was performed under rotation at 120°C for 2d, following by an annealing process in cited procedure.

Crystals were isolated from the supernatant by three cycles of centrifugation, dried at room temperature in air, and then calcined in flowing dried air (100 mL min<sup>-1</sup>, Matheson Tri-Gas) at 550 °C (heating and cooling rates of 1 °C min<sup>-1</sup>) for 5 h. Ion exchange was performed three times using a 1 M NH<sub>4</sub>NO<sub>3</sub> solution (2 wt% of calcined samples in solutions), which was heated at 80 °C under continuous stirring for 2 h. The exchanged samples were dried and calcined by the same procedure described above to

obtain H-form zeolites.

### **3.3.3 Time-elapsd study of synthesis**

To examine the crystallization process, we followed previously outlined synthesis procedure and divided one synthesis solution into four different autoclaves. The autoclaves were placed in an oven at set temperature and were each removed and quenched at periodic times (ca. 3, 6, 12, and 24 h). The supernatant was separated from the solids by centrifugation and diluted with a recorded dilution factor prior to elemental analysis by ICP-MS.

### **3.3.4 Characterization of ZSM-5 zeolites**

Powder X-ray diffraction (XRD) patterns were collected on a Rigaku diffractometer using Cu K $\alpha$  radiation (40kV, 40 mA) to verify the crystallinity and topology of the catalysts. Nitrogen physisorption experiments were performed on a Micromeritics ASAP 2020 instrument at 77 K to calculate micropore volumes (t-plot method) and BET surface area. Transient sorption experiments with 2,3-dimethylbutane were performed by the Bhan Group (U. Minnesota), and collected data was fitted following a previously reported procedure [24, 148] to obtain the characteristic diffusion timescale  $R^2/D$ . Scanning electron microscopy (SEM) was conducted at the Methodist Hospital Research Institute in the Department of Nanomedicine SEM Core using a Nova NanoSEM 230 instrument with ultrahigh resolution FESEM (operated at 15 kV and a 5mm working distance). The overall Si/Al ratio was determined by inductively coupled plasma optical emission spectrometry (ICP-OES) analysis at Galbraith Laboratories (Knoxville, TN). Energy dispersive X-ray spectroscopy (EDX) was performed using a

JEOL SM-31010/METEK EDAX system at 15 kV and 15 mm working distance. X-ray photoelectron spectroscopy (XPS) analysis of samples was performed using a PHI 5800 ESCA (Physical Electronics) multitechnique system equipped with a standard achromatic Al K $\alpha$  X-ray source (1486.6 eV) operating at 300 W (15 kV and 20 mA) and a concentric hemispherical analyzer. The equipment neutralizer component was utilized to reduce charging effects. All data were collected at a 45° takeoff angle.

### 3.3.5 Characterization of zoning in ZSM-5 zeolites

We used a combination of two elemental analysis techniques, EDX and XPS, to characterize the spatial distribution of elements in ZSM-5 zeolites. The average bulk chemical composition of ZSM-5 crystals was estimated by EDX, which has a sampling depth around two micrometers. The chemical composition of the outer rim of zeolite crystals was evaluated by XPS, which is a surface-sensitive technique with a sampling depth of only a few nanometers. Using the atomic percentages of aluminum and silicon, we define the percentage of aluminum occupying tetrahedral (T) sites as

$$Al_i = \frac{(\text{Al atom}\%)}{(\text{Al atom}\%)+(\text{Si atom}\%)}, \quad (3.1)$$

where  $i$  = bulk or surface based on EDX or XPS measurements, respectively. Herein, we use the ratio  $Al_{\text{surface}}/Al_{\text{bulk}}$  as a descriptor for the spatial aluminum distribution in ZSM-5 zeolites. When this ratio is greater than one, aluminum is disproportionately concentrated at the surface of ZSM-5 crystals compared to the bulk, leading to Al-zoning. On the contrary, a ratio less than one signifies Si-zoning.

### 3.3.6 Characterization of Al gradient in ZSM-5 zeolites

We used variable kinetic energy X-ray photoelectron spectroscopy (VKE-XPS) to

probe the change in Si and Al contents as a function of depth into the crystals. VKE-XPS was performed at NSLSII (Brookhaven National Laboratory, Upton, NY) at beamline 7-ID-2 with an HAXPES endstation. The powder form of samples was deposited onto carbon taped with a thin layer of carbon coating to reduce charging effect. Samples were taped onto a sample holder rod and installed in the vacuum chamber overnight. A neutralizer was also used to further prevent shift in binding energy due to charging effect. An L2 plane mirror was used for large (mm scale) spot size for spectra collection, with pass energy of 500 eV and a take-off angle of 80°. Ag3d spectrum was collected after every photon energy change to calculate actual ionization energy. Each sample sweep was for 0.5 to 1 h with a time ratio of 1:30 of Si1s to Al1s. The collected spectra were integrated using the Scienta program (IgorPro), and the peak areas were subsequently corrected with Scofield cross-section (NIST XCOM database) for Si/Al calculation. Inelastic mean free path (IMFP,  $\lambda$ ) was calculated from corresponding Si1s and Al1s kinetic energy at each photon energy (eV) using relativistic equation TPP2M formula in the QUASES program) for SiO<sub>2</sub> and Al<sub>2</sub>O<sub>3</sub>. The information depth was then calculated from IMFP using the following equation:

$$\text{Information depth} = 3\lambda\cos(\theta_{\text{photoemission}}). \quad (3.2)$$

### **3.3.7 Measurement of shell thickness for zoning analogues**

To approximate shell thickness of the core-shell and inverse core-shell samples, we used dynamic light scattering (DLS) to obtain the average hydrodynamic diameter. Initially, a small amount of sample was dispersed into DI water and sonicated at 8W for 5 – 10 min. The solution was then filtered through a 250  $\mu\text{m}$  membrane, further diluted

with DI water, and placed in a clean glass vial. The level of dilution was adjusted to ensure a scattering count rate within 100 to 400 kcps. The glass vial was placed in a filtered decalin bath sample holder housed within a Brookhaven Instruments BI-200SM DLS equipped with a HeNe laser (637nm) and TurboCorr Digital Correlator. A total of eight measurements (2 min each) was taken for each sample at 25 °C. The autocorrelation functions collected were analyzed using the method of cumulants in the Brookhaven Instruments Corporation DLS software. The shell thickness of the core-shell sample ZSM-5@silicalite-1 was estimated from differences in the hydrodynamic diameters of core (C-0.2) and core-shell (CS-0.2). The shell thickness of the inverse core-shell sample silicalite-1@ZSM-5 was calculated similarly from the silicalite-1 core and the core-shell sample (ES-0.3).

### **3.3.8 Characterization of Al species and acid sites**

Aluminum speciation was determined from  $^{27}\text{Al}$  MAS NMR spectra collected at a spinning frequency of 12.5 kHz, pulse of  $\pi/12$ , relaxation delay of 0.8s, and 4K scans at 11.7T on a JEOL ECA-500 spectrometer.[127] We quantified the total number of acid sites with temperature-programmed desorption of ammonia ( $\text{NH}_3$ -TPD) on a Micromeritics Autochem II 2920 equipped with a TCD detector. Approximately 100 mg of catalyst sample was degassed for 1 h at 600 °C before being cooled down to 100 °C for ammonia adsorption. At saturation, the sample was flushed with He for 120 min before we ramped up the temperature to 600 °C at a rate of 10 °C /min while concurrently monitoring the desorbed ammonia with the TCD detector. To identify the types of acid sites (i.e., Lewis and Brønsted), we conducted pyridine-adsorbed Fourier-

transform infrared spectroscopy (pyr. FTIR). We first collected background spectrum at room temperature for a high temperature cell equipped with KBr windows using a Nicolet 6700 FTIR spectrometer. Subsequently, approximately 20 mg of sample was pelletized and placed in the cell. The configuration was installed in the spectrometer and connected to heated N<sub>2</sub> gas lines (150 °C). The cell was heated to 550 °C for 2 h to eliminate adsorbed moisture in the sample before being cooled down to 200 °C for the adsorption experiment. Parent spectrum is collected before increment of 1 µl anhydrous pyridine (Sigma Aldrich) was injected into the heated N<sub>2</sub> stream (Matheson, 50 cm<sup>3</sup> min<sup>-1</sup>). Spectra were collected 5 min after each injection until saturation, and the final spectrum was collected after purging for 2 h with N<sub>2</sub>. The subtracted results from the final and parent spectra were analyzed using OMNIC software with peaks assigned to Brønsted and Lewis acid sites at 1545 and 1450 cm<sup>-1</sup>, respectively [200]. The corrected peak area was used to obtain the percentages of Brønsted and Lewis acid sites.

### 3.3.9 Reaction testing

Methanol-to-hydrocarbon (MTH) reaction was carried out in a 0.25 in. stainless steel tube installed in a VTS clamshell furnace, equipped with a Watlow controller. All catalysts (40 – 60 mesh size) were diluted with silica gel (Davisol Grad 636; 35 – 60 mesh size) and held between two plugs of quartz wool. A K-type thermocouple (Omega Engineering) was inserted into the stainless tube to measure the temperature of the bottom of the catalyst bed. Prior to the reaction, the catalyst bed was pretreated *in situ* at 550 °C for 3 h under flow of dried air (Matheson, 6 cm<sup>3</sup> min<sup>-1</sup> of O<sub>2</sub>, 24 cm<sup>3</sup> min<sup>-1</sup> of N<sub>2</sub>). The catalyst bed was then cooled to the reaction temperature, 350 °C. Methanol

was fed by a syringe pump (Harvard Apparatus) into a heated inert gas stream of Ar (Matheson, UHP) to achieve a methanol partial pressure of 11.5 kPa. The molar space velocity is varied in the range of 0.18 – 0.30 s<sup>-1</sup> for the set of homogeneous and zoning samples, and in the range of 0.77 – 1.23 s<sup>-1</sup> for the set of core, core-shell, and inverse core-shell samples. First data point was collected after 20 min time on stream (TOS). Reaction effluent was evaluated using an on-stream gas chromatograph (Agilent 7890B) equipped with a FID detector and an Agilent DB-1 capillary column. Methanol and dimethyl ether (DME) are considered as reactant with the conversion  $X$  defined as

$$X = [1 - C_{\text{eff}}/C_{\text{feed}}] \times 100\% \quad (3.3)$$

where  $C_{\text{eff}}$  is the concentration of both methanol and DME in the effluent and  $C_{\text{feed}}$  is the concentration of methanol in the feed. The selectivity  $S_i$  of hydrocarbon product  $i$  is defined as

$$S_i = [C_i/C_{t,\text{eff}}] \times 100\% \quad (3.4)$$

where  $C_i$  is the concentration of hydrocarbon  $i$  in the effluent and  $C_{t,\text{eff}}$  is the total concentration of hydrocarbons in the effluent. Turnover number (TON) is calculated for a period of TOS based on previously reported equation[24]:

$$\text{TON}(t) = \frac{1}{N_{\text{H}^+}} \int_{t_1}^{t_2} F(\tau) d\tau \quad (3.5)$$

where  $N_{\text{acid site}}$  is the total number of Brønsted acid sites (from NH<sub>3</sub>-TPD and pyr. FTIR data),  $F(\tau)$  is the molar flow rate of converted carbon (methanol and dimethyl ether), and  $t$  is TOS.

### 3.3.10 Operando UV-vis spectroscopy with on-line gas chromatography

The hydrocarbon pool active species and related coke compounds formed during the

MTO processes were determined using operando UV-vis spectroscopy.[201] Operando UV-vis spectra were obtained using an AvaSpec 2048L spectrometer connected to a high-temperature UV-vis optical fiber probe, which was used to collect spectra in reflection mode. The measurements were performed in the wavelength range of 200 – 1000 nm (11000 – 50000  $\text{cm}^{-1}$  in wavenumber) using a high-temperature UV-vis probe provided by Avantes. The probe comprises one excitation and one collection optical fiber with a size diameter of 400  $\mu\text{m}$  and length of 1.5 m, which are placed in a stainless steel protection sleeve. The probe was connected to a deuterium-halogen light source and an AvaSpec 2048 UV-vis spectrometer. The probe was custom-made to operate at temperatures up to 873 K. The spectra were saved every 30 s, with 100 accumulations of ~50 ms exposure time each. Catalytic testing was done in a fixed-bed quartz reactor. The catalyst powder was pressed to give pellets, followed by crushing and sieving. The 212–425  $\mu\text{m}$  fraction was used for catalytic testing. Prior to the reaction the same amount of catalysts and silica gel as those in the catalytic testing was loaded and activated 550 °C for 3 h under 100% oxygen and then cooled to 350 °C. The weight hourly space velocity (WHSV) of methanol was kept at 9  $\text{g g}^{-1} \text{h}^{-1}$  by flowing He gas through a methanol saturator, which was kept at a temperature of ~293 K. The temperature of the reaction was varied between 573 and 723 K. Analysis of the reactant and reaction products was performed with online gas chromatography (Interscience Compact GC), equipped with an Rtx-wax and Rtx-1 column in series and an Rtx-1, Rt-TCEP and  $\text{Al}_2\text{O}_3/\text{Na}_2\text{SO}_4$  in series, both connected to an FID detector.

### 3.4 Results and Discussion

#### 3.4.1 Synthesis of Zoned ZSM-5 Crystals

We selected two reported protocols for synthesizing ZSM-5 in growth mixtures comprised almost solely of an organic (i.e., tetrapropylammonium, TPA<sup>+</sup>) [22] or exclusively with an inorganic (Na<sup>+</sup>) [202] structure-directing agent. The conditions of these two syntheses also differ with respect to temperature (100 vs. 190°C, respectively) and silicon source (tetraethylorthosilicate vs. colloidal silica, respectively). Elemental analysis using a combination of EDX and X-ray photoelectric spectroscopy (XPS) were performed to assess the Si/Al ratio of the entire crystal (bulk) and the outermost layer (surface). Both reference protocols yield ZSM-5 zeolites with a homogeneous distribution of Al, as indicated by equivalent bulk and surface Si/Al ratios. Interestingly, modifications of the synthesis composition to generate mixtures of both organic and inorganic SDAs resulted in the formation of zoned ZSM-5 materials where the degree of zoning increases monotonically as the ratio of SDAs approaches 50/50 organic/inorganic (**Figure 3.2b and c**). For syntheses in organic-rich media at lower temperature, the combination of TPA<sup>+</sup>/Na<sup>+</sup> results in Al-zoned ZSM-5 (**Figure 3.2b**), whereas for inorganic-rich media at higher temperature the combination yields Si-zoned ZSM-5 (**Figure 3.2c**). For comparison, we tested the effect of partially replacing Na<sup>+</sup> with K<sup>+</sup>, which has been shown to enhance the rate of ZSM-5 crystallization and alter Al incorporation [203, 204]. Our findings reveal similar trends in Si/Al ratio for both alkali metals; however, further characterization of select samples reveal distinct differences in their physicochemical properties, as discussed later.

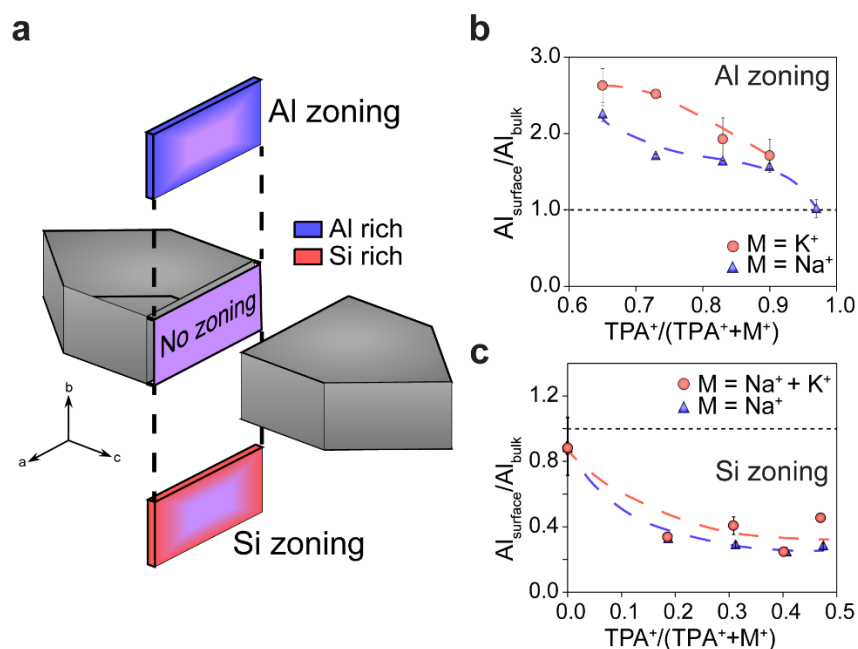


**Figure 3.2.** (a) Idealized depiction of Al- and Si-zoning in zeolite ZSM-5. (b) Ratio of  $Al_{\text{surface}}/Al_{\text{bulk}}$  as a function of organic SDA fraction ( $TPA^+$ ) in the growth mixture. Compositions of each sample are provided in Tables B1, B2, and B3.

Herein we focus on six samples using a naming convention for zeolites with a homogeneous Al distribution (Hx-y), Al-zoning (A-y), and Si-zoning (Sx-y) where  $x$  refers to the sample number and  $y$  refers to the effective crystal size (in microns). Powder X-ray diffraction (PXRD) patterns of all samples (Figs. S1 – S3) confirm the MFI framework structure of ZSM-5 without evidence of any impurities or residual amorphous material. Scanning electron microscopy (SEM) images of zeolite samples (**Figure 3.3**) reveal a distribution of crystal size and morphology. The Al-zoned sample (A-4) has the smallest crystal size (**Figure 3.3a**, ca. 1  $\mu\text{m}$ ). Homogenous samples exhibit similar size by SEM, but disparate morphology depending on synthesis conditions: spheroidal shapes obtained from a  $TPA^+$ -rich mixture (H1-3, **Figure 3.3b**) and faceted coffin-shapes with observable twinning from a  $Na^+$ -rich mixture (H2-6, **Figure 3.3c**).

The Si-zoned samples (S1-1, S2-1, and S3-2) exhibit similar morphology with differences in crystal size spanning 3 – 12  $\mu\text{m}$  (**Figures 3.3d – f**, respectively). One notable distinction among Si-zoned samples is the presence of faceted layers, or macrosteps, on the surfaces of the larger crystals (S2-1 and S3-2).

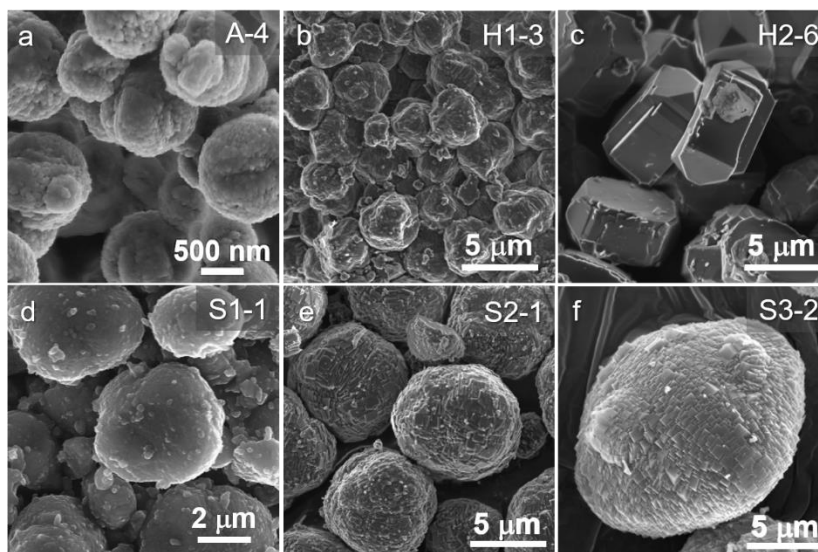


**Figure 3.3.** SEM images of (a) Al-zoned sample A-4, (b and c) homogeneous samples H1-3 and H2-6, and (d – f) Si-zoned samples S1-1, S2-1, and S3-2. All syntheses were performed at 190°C, with the exception of sample A-4 (100°C).

Few studies in literature have reported the direct synthesis of Si-zoned ZSM-5 [130, 131, 205]. Although the exact mechanism of formation is unknown, we posit the origin of Si-zoning is related to the relative rates of Si and Al depletion from growth media at various stages of crystallization compared to ZSM-5 samples with homogeneous Al distribution. To test this hypothesis, we conducted time-resolved measurements of supernatant Si and Al composition over a 24-hour period of hydrothermal treatment at 190°C (**Figure B4**). For synthesis mixtures leading to a ZSM-5 product with homogeneous Al distribution (e.g., H1-3), the supernatant solution after only 3 hours of heating contains ca. 776 mM of dissolved Si and Al with a Si/Al ratio of 43. Analysis

of PXRD patterns (**Figure B5a**) over the course of the full time period indicates that crystallization is nearly complete by 3 hours; however, corresponding SEM images (**Figure B6a – d**) reveal morphological changes between 3 and 24 hours that is seemingly associated with a ripening process based on the fact that crystal structure is unchanged and there is only a small shift in the elemental composition (Si/Al ratio) of extracted solids from  $31 \pm 5$  (at 3 hours) to  $26 \pm 2$  (at 24 hours). Conversely, the crystallization of Si-zoned ZSM-5 (e.g., S2-1) is much slower, such that the extracted solids after 3 hours are largely amorphous (**Figure B5b**). The corresponding supernatant solution contains much less dissolved solute (ca. 229 mM of Si and Al) with a Si/Al ratio of 429 (**Figure B4**). Analogous to time-resolved images during H1-3 synthesis, the morphology of extracted solids during S2-1 synthesis exhibit subtle changes in surface topography (**Figures B6e – h**). Collectively, these studies seem to indicate that a binary mixture of  $\text{TPA}^+/\text{Na}^+$  shift the equilibrium such that there is a reduced concentration of dissolved solute that is enriched with silicon, which likely facilitates the formation of Si-zoned samples; however, a fundamental understanding of this phenomenon is unresolved.

Depth profiling of Si/Al ratio was conducted with variable kinetic energy X-ray photoelectron spectroscopy (VKE-XPS). In these experiments the effect of charging can shift the binding energy of the samples, making it difficult to ascertain oxidation state, yet the intensity of each peak (semi-quantitatively correlated to Si and Al content) clearly demonstrates an increase in Al content with increasing probing depth into the crystal (i.e., increased photon energy) (**Figure 3.4a**). The binding energy ( $E_B$ , x-axis) is

plotted relative to the binding energy of spectra collected at a photon energy of 3003 eV ( $E_{B0} = 1839.2\text{eV}$  for Si1s and  $1559.2\text{ eV}$  for Al1s). The integrated peaks were used to calculate Si/Al ratios of each sample as a function of photon energy and information depth (**Figure 3.4b**), taken as 3 times the inelastic mean free path (IMFP). There is an obvious decrease in Si/Al with increased information depth for the three Si-zoned samples, as expected for Si-zoned samples with a siliceous exterior and higher Al content toward the interior. Notably, Si-zoned sample S2-1 shows a sharper decrease in Si/Al which is indicative of a thinner siliceous region in comparison to samples S1-1 and S3-2. One distinguishing feature of the S2-1 synthesis relative to those of S1-1 and S3-2 is the absence of potassium in the growth mixture, which may account for its thinner region of Si zoning.

**Table 3.1.** Physicochemical properties of H-ZSM-5 samples selected for catalyst testing

Catalyst sample <sup>a</sup>	$R_A$ ( $\mu\text{m}$ )	$R_E$ ( $\mu\text{m}$ )	$\text{Al}_{\text{ratio}} \text{ S/B}$ <sup>b</sup>	BET $S_A$ ( $\text{m}^2/\text{g}$ )	$V_{\text{micro}}$ ( $\text{cm}^3/\text{g}$ )	Si/Al <sub>c</sub>	$C_{\text{acid}}$ <sup>d</sup> ( $\mu\text{mol}/\text{g}$ )	Acid type <sup>e</sup> (%)		EFAl <sub>f</sub> (%)
								B	L	
A-4	1.1	3.8	1.7	409	0.08	28	531	na <sup>g</sup>	na <sup>g</sup>	12
H1-3	4.0	2.9	1.04	405	0.12	28	673	82	18	6
H2-6	4.0	6.4	0.88	370	0.12	21	941	88	12	7
S1-1	3.0	1.2	0.27	431	0.12	29	730	85	15	7
S2-1	8.0	1.3	0.32	403	0.12	37	578	83	17	3
S3-2	12.0	1.6	0.42	416	0.12	29	773	85	15	6
C-0.2	0.2	1.6	1.0	518	0.14	40	435	68	32	4
CS-0.2	0.2	1.2	0.78	516	0.15	46	327	71	29	3
ES-0.3	0.3	1.5	3.07	440	0.12	59	152	79	21	6

<sup>a</sup> A = Al-zoned, H = homogeneous, S = Si-zoned, C = core, CS = core-shell (ZSM-5@silicalite-1), ES = eggshell (silicalite-1@ZSM-5); <sup>b</sup> S/B = surface-to-bulk Al ratio; <sup>c</sup> ICP-OES; <sup>d</sup>  $\text{NH}_3$ -TPD, Fig. B9; <sup>e</sup> Measured by pyridine FTIR where B = Brønsted acid sites and L = Lewis acid sites; <sup>f</sup> Measured by  $^{27}\text{Al}$  MAS NMR, Fig. B10; <sup>g</sup> Not quantifiable due to negligible adsorption of pyridine

### 3.4.2 Comparison of Catalyst Performance

As-synthesized ZSM-5 samples were ion exchanged with  $\text{NH}_4^+$  and calcined to produce Brønsted acids (H-form) catalysts. The physicochemical properties of all corresponding H-ZSM-5 catalysts used in MTH reactions are provided in **Table 3.1**. Textural analysis (**Figure B8**) reveals similar values for all samples with the exception of Al-zoned A-4, which has lower micropore volume. Sample A-4 also has higher extra-framework Al (EFAl) content (i.e., approximately twice that of the other samples). Elemental analysis by ICP-OES reveals a relatively narrow range of Al content ( $\text{Si}/\text{Al} = 21 - 37$ ). The apparent crystal size,  $R_A$ , of each sample estimated from SEM images is reported in **Table 3.1**; however, we also determined an effective size,  $R_E$ , using a reported protocol [24, 148] where the effective diffusion timescale ( $D/R_E^2$ ) was measured from 2,3-dimethylbutane sorption experiments (**Figure B7**, where  $D$  is an effective diffusion coefficient measure for silicalite-1 at 110°C from literature [206]). A detailed discussion of these measurements is provided in the Methods. Interestingly, there are noticeable differences between sizes estimated from microscopy and sorption measurements. A parity plot in **Figure 3.4c** reveals that the Si-zoned samples have effective sizes that are much less than their apparent sizes from SEM images (i.e., as much as 8-fold less), whereas the Al-zoned sample has a larger  $R_E$  (ca. 4-fold larger) that seems to indicate the presence of defects resulting in mass transport restrictions (consistent with its notably lower microporous volume). For comparison, we also plotted values reported by Bhan and coworkers [27, 148] for ZSM-5 catalysts spanning a broad range of sizes ( $R_A = 2 \text{ nm to } 17 \text{ }\mu\text{m}$ ). Among all reported samples, the two

measured dimensions vary between being either nearly equivalent or having smaller  $R_E$  that are within a 2-fold difference. Homogeneous sample H1-3 falls close to the parity line, whereas homogeneous sample H2-6 is one of the only examples among those in **Table 3.1** (with the exception of A-4) to have an effective size larger than its apparent size.

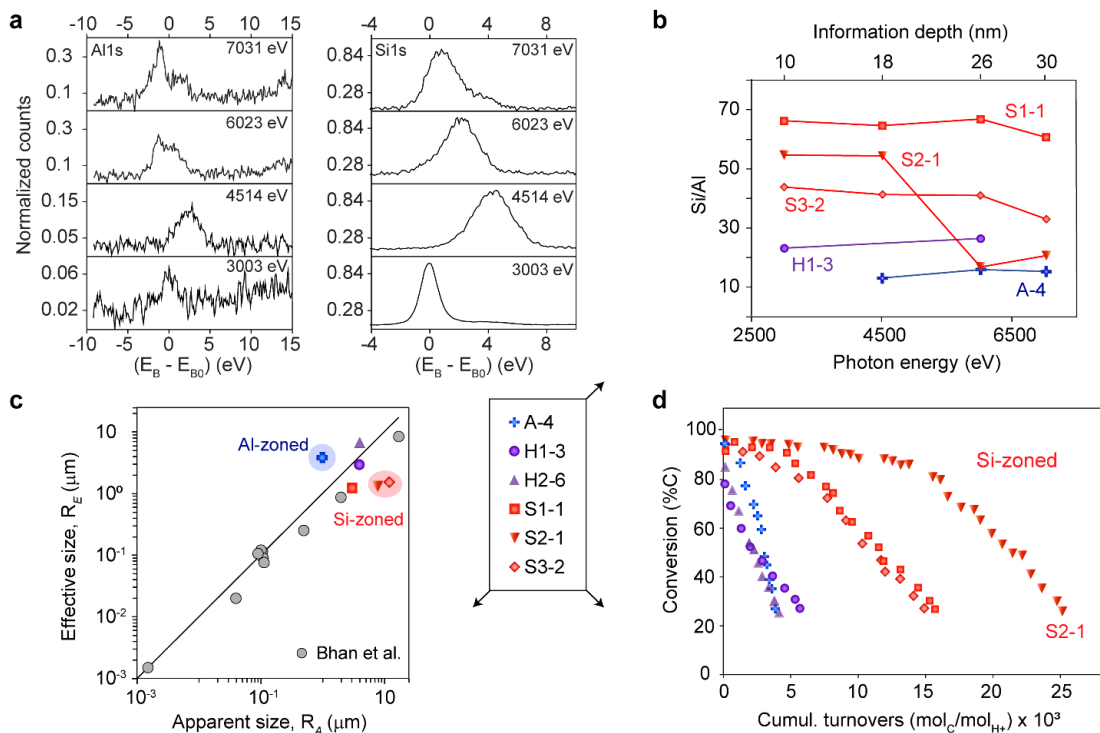


**Figure 3.4.** (a) Raw VKE-XPS spectra for sample S2-1 for other samples (Figures B11 and B12). (b) Si/Al from XPS depth analysis for 5 samples. (c) Parity plot in log scale of  $R_E$  against  $R_A$ . (d) Conversion of MeOH and DME versus cumulative turnovers.

Catalyst performance in the MTH reaction (**Figure 3.4d**) was assessed at sub-complete conversion ( $< 96\%$ ) using a similar molar contact time for all samples. As a proxy for time on stream (TOS) we use the cumulative turnovers (Eq. 3.5 in Methods) to compare all six catalysts. Surprisingly, all Si-zoned samples markedly outperform homogeneous sample H1-3 with lifetimes extended by as much as 4-fold. The activity

of the Al-zoned sample is slightly prolonged at early TOS but exhibits the fastest rate of deactivation (i.e., slope of the linear regions in **Figure 3.4d**). There are distinct differences between the two homogeneous samples, with H2-6 being less stable (ca. 2-fold less than H1-3). One factor that can explain the poor performances of both H2-6 and A-4 is their large  $R_E$  relative to  $R_A$ , which is indicative of diffusion limitations imposed by defects that compromise catalyst lifetime (as discussed later). Another interesting observation is the exceptionally long lifetime of S2-1 among the three Si-zoned samples, despite having an intermediate value of  $R_A$  (ca. 8  $\mu\text{m}$ ) and comparable  $R_E$  to S1-1. One factor that may contribute to its superior performance is the relatively thin region of silicon zoning, as indicated by VKE-XPS (**Figure 3.4b**).

To facilitate side-by-side comparisons of catalysts in a manner that accounts for the variability of physicochemical properties listed in Table 3.1, we introduce a structure-performance descriptor,  $R_E C_{H^+} S_A^{-1}$ , that is inspired by approaches reported by Bhan [25, 27] and Gascon [207] with slight modification. The descriptor used here accounts for mass transport ( $R_E$ , or diffusion path length) and total acid sites, analogous to Bhan's approach where the parameter  $C_{H^+}$  used here is the total concentration of Brønsted acid sites measured from combined  $\text{NH}_3$  TPD and pyridine FTIR. We also account for the BET surface area,  $S_A$ , used by Gascon, which yields a descriptor with units of moles Brønsted acids per unit length, in close agreement with the descriptor that was mathematically derived by Bhan (i.e., number of Al sites per unit length) [27]. Using the turnover number (TON) as a quantitative measure of catalyst lifetime, we assessed the performance of each catalyst in **Figure 3.5a** along with repeat samples and found

that trends were absent when comparisons were made on the basis of individual properties (e.g.,  $R_E$ ,  $C_{H^+}$ , etc.); however, a clear trend emerges when data are plotted in log-log scale as a function of the descriptor (**Figure 3.5a**), which is qualitatively consistent with a trend reported for SAPO-34 catalysts in the MTH reaction [25]. The indicator E/2MBu for the dual cycle mechanism representing the ratio of ethene to the sum of 2-methylbutane and 2-methylbutene (2MBu) is plotted in **Figure 3.5b** (log-log scale) as a function of the descriptor where we observe a decrease in E/2MBu ratio with decreasing values of the descriptor, in accordance with reported trends for ZSM-5 catalysts in MTH reactions (**Figure B13**) [27].

The data in **Figure 3.5** is one of the few examples where trends in lifetime and selectivity are directly compared as a function of catalyst properties. Interestingly, we see an inverse relationship where increased TON is correlated with reduced E/2MBu ratio, indicating the olefin-based cycle is promoted at lower values of  $R_E C_{H^+} S_A^{-1}$ . The physical meaning of the descriptor is the total number of acid sites that a molecule encounters over the net diffusion path length. Previous studies have shown how each factor (Al content and effective size) individually impacts the propagation of olefin and aromatic cycles. These trends are consistent when coupling both effects within the descriptor, irrespective of gradients in Al distribution among homogeneous or Si-zoned samples; however, the Al-zoned sample (A-4) appears to defy the trend given that its E/2MBu ratio is equivalent to the Si-zoned S1-1 while there is a 4-fold difference in TON values. This highlights the capability of this descriptor to identify outliers among catalyst samples. Another observation along these lines is the use of the descriptor to

identify the impact of synthesis conditions on catalyst performance. For instance, the two homogeneous samples were prepared using growth solutions with predominant organic (H1-3) or inorganic (H2-6) SDAs, where the latter synthesis protocol generates a less effective catalyst. Alternatively, the two Si-zoned catalysts with lower turnover number (samples S1-1 and S3-2) were prepared from growth mixtures containing  $\text{Na}^+$ ,  $\text{K}^+$ , and  $\text{TPA}^+$  (compared to  $\text{Na}^+$  and  $\text{TPA}^+$  for S2-1), suggesting the presence of  $\text{K}^+$  extends the region of silicon zoning (Figure 3.4b) that likely impacts catalyst lifetime (Figure 3.4d).

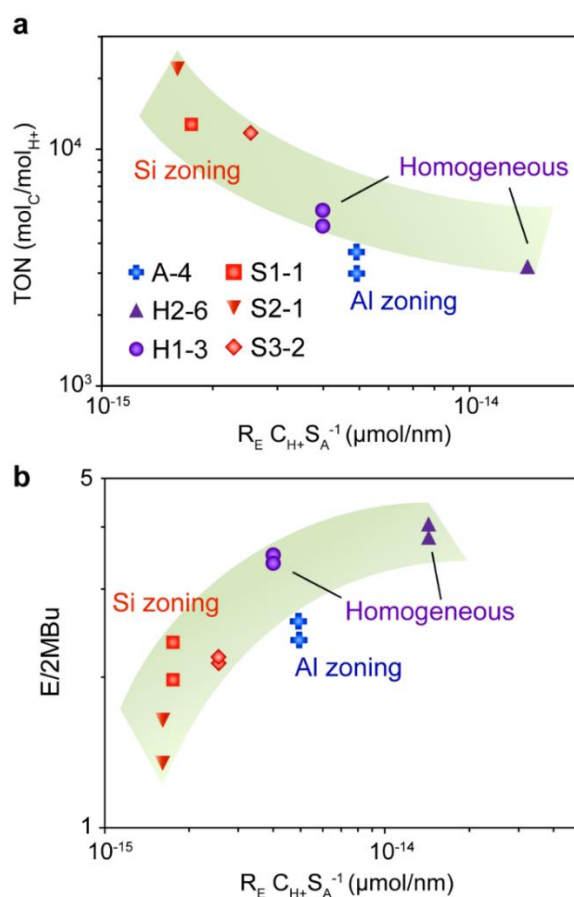


**Figure 3.5.** (a) Turnover number for H-ZSM-5 catalysts calculated from conversion vs. time on stream data (Figure B14) and (b) E/2MBu as function of the descriptor  $R_E C_{H^+} S_A^{-1}$ . Zoned trend line is qualitatively consistent with that reported in literature (Figure B13).

### 3.4.3 Deactivation Mechanism of H-ZSM-5 Catalysts

To further understand the catalytic behaviors of these samples, operando UV-Vis diffuse reflectance (DR) spectroscopy was utilized to follow the evolution of reactive intermediates, or hydrocarbon pool (HP) species, as well as coke (internal and external) [1, 24, 201, 208]. The catalysts are tested in a packed-bed reactor configuration where time-resolved UV-Vis spectra of the catalyst are collected during reaction. Here we correlate three regions of the spectra in generic groupings of HP species (**Figure 3.6a**, blue region), internal coke species (**Figure 3.6a**, yellow region), and external coke species (**Figure 3.6a**, gray region).

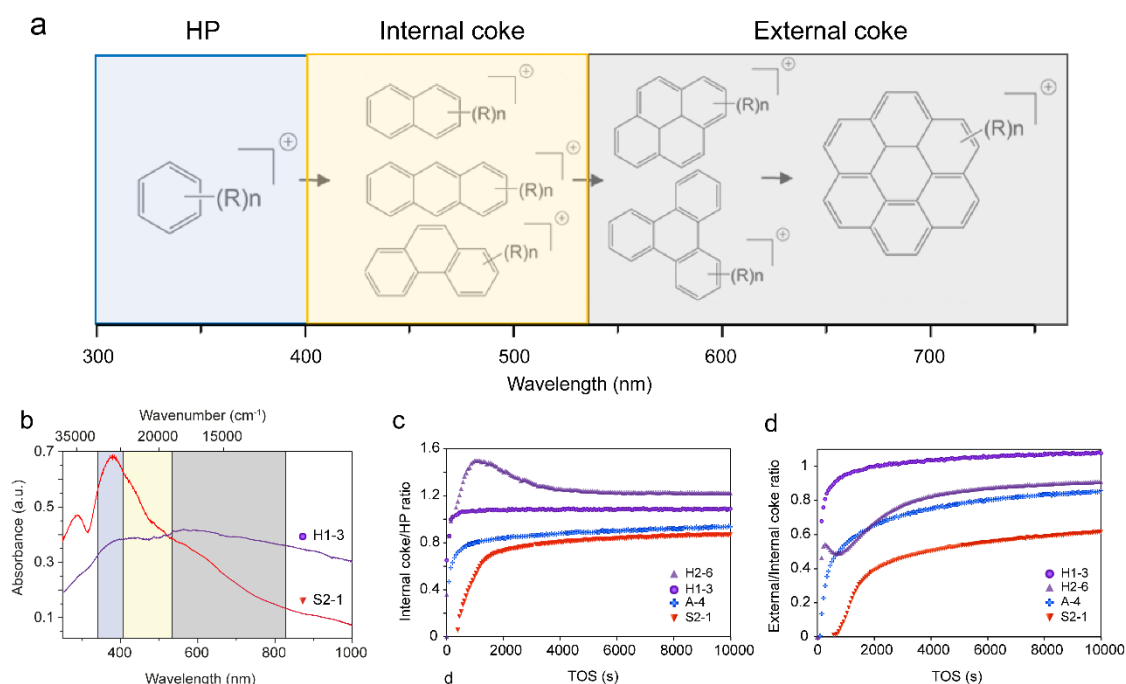


**Figure 3.6.** (a) UV-Vis bands corresponding to species during the MTH reaction [1]. (b) Operando UV-Vis spectra of selected samples. Changes of the intensity ratio of (c) internal coke-to-HP species as a function of TOS and (d) of the intensity ratio of external-to-internal coke species.

Comparison of UV-Vis spectra for representative homogeneous (H1-3) and Si-

zoned (S2-1) samples after 9990 s of MTH reaction at 350 °C (**Figure 3.6b**, see **Figure B15** for the full set of samples) reveal a significant reduction in external coke species relative to HP species for the zoned catalyst. Using select peaks in each spectrum (**Table S6**) we report a ratio of internal coke to HP species (**Figure 3.6c**) for four samples (see **Figure B16** for others). The Si-zoned catalyst (S2-1) has the lowest intensity ratio among all samples, which is qualitatively consistent with its longer lifetime (**Figure 3.4d**). The presence of a siliceous exterior also suppresses the formation of external coke, which is evident in the ratio of external to internal coke species (**Figure 3.6d**). Again, the Si-zoned catalyst exhibits the least degree of external coking compared to other samples. Similar suppression of internal (**Figure B16a**) and external (**Figure B16b**) coke is observed for the other two Si-zoned samples (S1-1 and S1-2); however, sample S2-1 stands out as having the lowest ratios of coke species, which is also reflected in its TON being 2-fold higher than other Si-zoned samples (Table S3.5). The exceptional performance of S2-1 among Si-zoned samples can be ascribed to its lower overall Brønsted acid concentration (**Table 3.1**), which is also reflected in its lowest  $R_E C_{H^+} S_A^{-1}$  value (**Figure 3.5**). An additional contributing factor may be the thinner Si-rich exterior region of S2-1 (**Figure 3.4b**).

There are clear differences between the homogeneous samples where the one prepared with Na<sup>+</sup> (H2-6) has a lower TON and larger R<sub>E</sub> than the one prepared with TPA<sup>+</sup> (H1-3). The former has the highest ratio of internal to HP species (**Figure 3.6c**) with a distinct maximum observed at early TOS. The preferential deactivation of H2-6 by internal coking can be interpreted as an initial buildup of coke species due to

diffusion limitations; and with time a larger fraction of coke precursors reach the external surface, leading to a delayed increase in external coke (**Figure 3.6d**). The disparity in size ( $R_E > R_A$ ) for H2-6 (**Figure 3.4c**) is suggestive of crystalline defects. This is consistent with a prominent broad band observed in the FTIR spectrum of H2-6 (**Figure 3.7a**) in the region associated with internal silanols (ca. 3650 – 3720  $\text{cm}^{-1}$ ). Bands have been assigned [200] to external silanols (ca. 3745  $\text{cm}^{-1}$ ), internal silanols (3720-3710  $\text{cm}^{-1}$ ), partially extra-framework Al (ca. 3665  $\text{cm}^{-1}$ ), Brønsted acid sites (ca. 3615  $\text{cm}^{-1}$ ), and silanol nests (ca. 3500  $\text{cm}^{-1}$ ). The presence of internal silanols have previously been correlated with deactivation where Beato and coworkers [209] refer to these sites as internal defects that can slow diffusion of hydrocarbon products and/or stabilize the adsorption of coke precursors. In a separate study, Valtchev and coworkers also demonstrate that ZSM-5 with less internal silanols have better activity and resistance to deactivation [210]. The other sample (H1-3) has fewer internal silanols (**Figure 3.7a**) and less diffusion limitations (as inferred by  $R_E \approx R_A$  in **Figure 3.4c**); therefore, this set of homogeneous H-ZSM-5 catalysts provides evidence that an increased number of crystalline defects can shift the predominant mode of deactivation from external (H1-3) to internal (H2-6) coking.

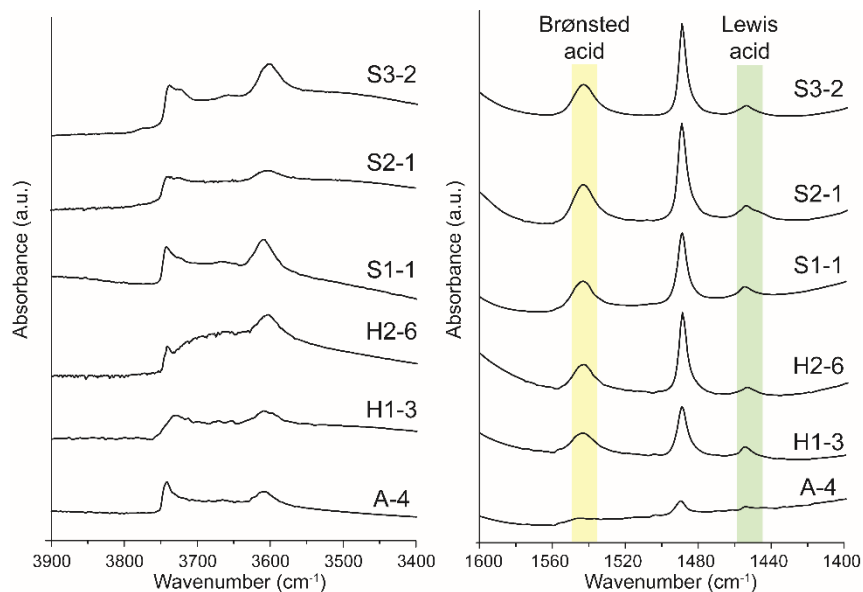


**Figure 3.7.** (a) Spectra in the range of 3900-3400  $\text{cm}^{-1}$  for H-form samples before pyridine adsorption. (b) Spectra in the range of 1600-1400  $\text{cm}^{-1}$  after pyridine adsorption.

Operando UV-Vis spectroscopy data for the Al-zoned sample (A-4) diverges from the above interpretations. This can be explained on the basis of diffusion limitations ( $R_E/R_A \approx 4$ ) that leads to a short lifetime (**Figure 3.4d**) and a TON that is comparable to defective H2-6 (**Table B5**). Interestingly, the ratio of internal coke to HP species for A-4 is lower than both homogeneous samples (**Figure 3.6c**) and its external-to-internal coke ratio is nearly equivalent to that of H2-6 (**Figure 3.6d**). The intermediate levels of internal and external coking for A-4 complicate the assignment of its predominant mode of deactivation. Acid site titration by pyridine-FT-IR spectroscopy yields a low-intensity spectrum in which the relative percentages of Brønsted and Lewis acids cannot be resolved. This suggests pore narrowing and/or pore blockage in Al-zoned samples, which could be associated with its relatively high percentage of extra-framework Al (**Table 3.1**) or may reflect partially-coordinated framework Al that was previously reported for Al-zoned ZSM-5 [127]. These defective Al sites impose extreme diffusion

limitations that promote internal coking and leads to lower external coking than expected on the basis of high Al concentration at the catalyst surface (**Table 3.1**). Similar ratios of internal coke to HP species for Al- and Si-zoned samples observed in **Figure 3.6c** may be attributed to an inaccessible fraction of active sites in sample A-4 as a result of defective Al, which could explain why the poor performance of Al-zoned ZSM-5 deviates from the trends of other catalysts (**Figure 3.5**).

#### 3.4.4 Analogues of Zoned ZSM-5

To demonstrate the efficacy of Si-zoning as a post-synthesis modification method, we synthesized a ZSM-5@Silicalite-1 core-shell catalyst (**Figure 3.8a**) as a Si-zoned analogue wherein a shell of silicalite-1 (siliceous **MFI**) was epitaxially grown on a homogeneous ZSM-5 parent crystal (core) using a previously reported protocol [22]. Standard characterization of both the core (sample C-0.2) and core-shell (sample CS-0.2) was performed (**Table 3.1, Figures B17 and B18**) in addition to dynamic light scattering (DLS) experiments to confirm the average thickness of the shell (<5 nm). Here we use the same convention for sample names where numbers indicate the apparent size  $R_A$  of the core (ca. 200 nm). Sample C-0.2 was prepared with a higher silicon content (Si/Al = 46) in order to achieve monodisperse spheroidal crystals for facile identification of shell growth. Catalyst performance was assessed at sub-complete conversion (<60%) using a lower space velocity than samples in Figure 3d owing to the reduced concentration of acid sites in sample C-0.2. The Si-zoned analogue CS-0.2 exhibits a 2-fold increase in catalyst lifetime (**Figure 3.8b**) compared to its homogeneous parent (C-0.2), consistent with the trend observed for Si-zoned samples

prepared by a one-pot synthesis. The concomitant increase in TON and decrease in E/2MBu ratio (**Figure 3.8c**) with the addition of a siliceous shell is also consistent with trends in **Figures 3.5a** and **3.5b**, respectively. This result is proof of principle that the performance of a ZSM-5 catalyst can be enhanced via post-synthesis modification as a proxy for direct synthesis of Si-zoned materials.

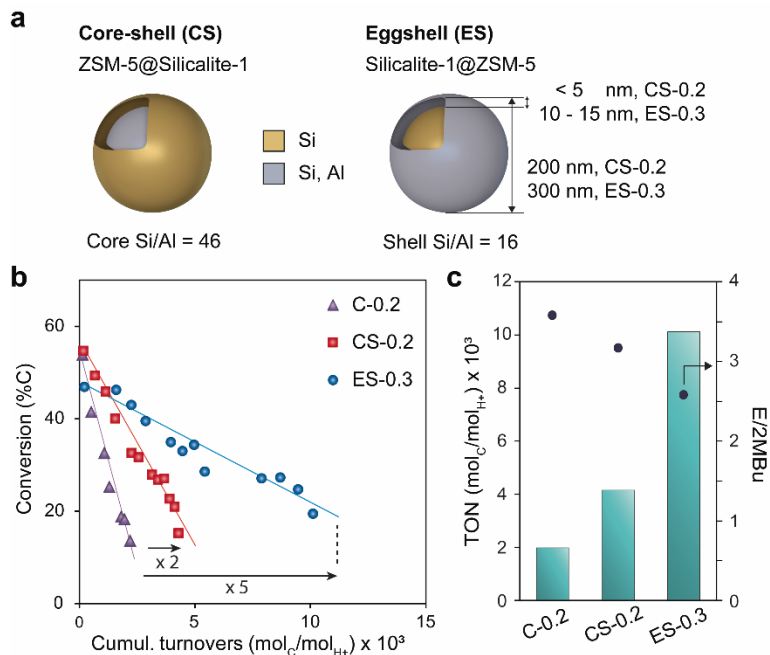


**Figure 3.8.** (a) Illustrations of core-shell (left) and eggshell (right) catalysts with thin (10 – 15 nm) shells. (b) Conversion of MeOH and DME as a function of cumulative turnovers. (c) Comparison of turnover number (TON, left y-axis) and E/2MBu ratio (right y-axis).

To address whether Al-zoned ZSM-5 is an inherently poor catalyst or a manifestation of defective Al, we prepared an “inverse” core-shell analogue (Silicalite-1@ZSM-5, sample ES-0.3) where a thin layer (10 – 15 nm) of ZSM-5 was epitaxially grown on a silicalite-1 core ( $R_A = 300$  nm). Analysis of ES-0.3 (**Table 3.1**) reveals no apparent diffusion limitations observed in the FT-IR spectrum after pyridine titration and a low quantity of EFAl in contrast to sample A-4. The performance of ES-0.3 aligns

with expectations for nanosized ZSM-5 [24, 30, 35, 211] that tend to exhibit long catalyst lifetime (**Figure 3.8b**), high TON, and low E/2MBu ratio (**Figure 3.8c**). These results confirm that the sub-optimal performance of Al-zoned ZSM-5 prepared by a one-pot synthesis (sample A-4) is primarily attributed to the presence of defective Al sites, consistent with our previous study [22] showing that penta-coordinated Al at the exterior of ZSM-5 catalyst dramatically reduces catalyst activity. Interestingly, ES-0.3 with its ca. 10-nm thick shell behaves as an ultrathin nanosheet that compares favorably with reported performances of 2D ZSM-5 (ca. 3 nm)[35]and other nano-sized ZSM-5 catalysts.[212] Reactions performed with ES-0.3 at a molar space velocity of  $0.77 \text{ s}^{-1}$  results in similar starting conversion (**Figure 3.8b**) as reactions with C-0.2 and CS-0.2 at lower space velocity ( $0.43$  and  $0.54 \text{ s}^{-1}$ , respectively). This indicates a higher apparent activity for ES-0.3, which has around one-half the concentration of Brønsted acid sites (**Table 3.1**), which contradicts general trends for homogeneous zeolite catalysts where a higher Si/Al ratio requires lower space velocity to achieve the same level of starting conversion. The exceptional catalytic performance of the egg-shell design shows promise for developing ultra-thin zeolite catalysts with reduced mass transport limitations and/or enhanced activity.

### 3.5 Summary

In this study we identified that surface passivation is an effective approach to manipulate the mass transport properties of zeolite catalysts and reduce the accumulation of coke on external surfaces. The enhanced performance of Si-zoned catalysts relative to homogenous counterparts suggests that diffusion limitations at the

pore mouth of MFI-type materials are more pronounced for ZSM-5 compared to silicalite-1. To this end, the approach presented here is a commercially-viable alternative to conventional methods aimed at reducing the size of zeolite crystals. Given the challenges of synthesizing ultra-small zeolites ( $< 100$  nm), one-pot methods to generate zeolite catalysts with elemental zoning is a relatively facile solution to improving diffusion properties that has the potential to be a generalizable approach for rational catalyst design.

## CHAPTER 4

### Core-Shell ZSM-11@Silicalite-2 Catalysts for Methanol-to-Hydrocarbons

The materials discussed in this chapter will be published in a peer reviewed journal. Figure and table labels are reformatted to be consistent with dissertation formatting requirement. The work was done in collaboration with Dr. Conan Weiland from Brookhaven National Laboratory, Dr. Simon R. Bare from SLAC National Accelerator Laboratory.

#### 4.1 Motivation

Zeolites as heterogeneous catalysts have significant commercial potential due to their shape selectivity and a set of tunable properties including but not limited to crystal habits and composition. The control of these properties proves to be challenging due to the complexity of zeolite synthesis and the resulting variability of aluminum speciations and macroscopic distribution, the latter of which receives notably less attention [198]. In chapter 3, we have shown that Al macroscopic distribution, also known as “zoning” can also impact zeolite catalysis, particularly methanol-to-hydrocarbons (MTH) reaction. Silicon zoning, in which the exterior of the zeolite crystal is Si-rich and hence lacking surface active sites, has been shown to improve catalyst lifetime in MTH. The enhancement in catalyst performance is mainly attributed to the suppression of external coke (i.e., bulky aromatics and graphitic hydrocarbons) development. In catalytic applications, since the Si-zoning phenomenon and synthesis of corresponding zeolites are underreported, its beneficial effect can be accomplished by multi-step synthesis whereby a layer of surface-passivated materials or a shell of siliceous zeolite is generated on the parent crystals. The first method (e.g., chemical vapor or liquid deposition of silanes) was first commercialized by Dupont [188] and Mobil [189] and

subsequently used by various groups [190, 191] with an overarching goal of limiting surface reactions and enforcing shape selectivity to within the interior pore network. However, deposition of amorphous layer can often narrow the zeolite pore mouth, which can improve product shape selectivity while sacrificing catalyst activity. Alternatively, the latter method can be used to generate a core-shell structures in which the core and shell are of identical framework type. An early example of core-shell zeolite is of an MFI core-shell, ZSM-5@silicalite-1 in a Mobil patent [189], and subsequent works on core-shell zeolites have been limited to only approximately 5 frameworks [137, 213-215]. In most cases, the shells are polycrystalline with thicknesses in the hundred nanometers to microns range, a factor which can negate the benefit of surface passivation by exacerbating mass transport limitations.

Various positive effects of both surface passivation and core-shell configuration, such as improve product selectivity [190, 216-218] and conversion capacity [136], have been reported; however, the variability in techniques and the difficulty of synthesizing well-defined materials with controllable thickness obfuscate the exact effect of surface passivation on catalysis. In chapter 3, we have shown for ZSM-5 in MTH reaction that catalyst lifetime can be enhanced by ca. 2-fold if the shell is sufficiently thin ( $< 5\text{nm}$ ). However, decoupling the effect of mass transport and surface passivation was not possible. Herein, we employ ZSM-11 and a previously devised method of controllable shell growth [22] to develop a model system to deconvolute the effect of siliceous shell on catalyst performance in MTH reactions. ZSM-11 is of MEL framework which has a more simplified network of straight

channels relative to MFI framework, and ZSM-11 catalyst has previously been shown to have exceptional performance in MTH [24, 219, 220].

## **4.2 Experimental Methods**

### **4.2.1 Materials**

The following reagents were purchased from Sigma-Aldrich: tetraethyl orthosilicate (TEOS, 98%), tetrabutylammonium hydroxide (TBAOH, 40%), 1,8-diaminooctane (DAO, 99%), aluminum sulfate ( $\text{Al}_2(\text{SO}_4)_3$ ), silica gel (Davisol Grade 636, 35-60 mesh size), and pyridine (99.8%, anhydrous). Deionized (DI) water was produced with an Aqua Solutions RODI-C-12A purification system (18.2 M $\Omega$ ). All reagents were used as received without further purification. For reaction testing, methanol was purchased from Sigma Aldrich (ChromaSolv, 99.9%), and argon, oxygen and nitrogen gases were purchased from Matheson with UHP grade (99.999%).

### **4.2.2 Synthesis and catalyst preparation of core-shell ZSM-11**

The synthesis of core ZSM-11 samples follows a previously published protocol for synthesis of MEL with 1,8 – diaminooctane [219]. The molar composition of the synthesis solution is 30 DAO: 10 K<sub>2</sub>O: 100 SiO<sub>2</sub>: 1 Al<sub>2</sub>(SO<sub>4</sub>)<sub>3</sub>: 4000 H<sub>2</sub>O. The solution was aged under stirring for 24 h before hydrothermal synthesis at 160°C for 3 d. The synthesized core was washed three times with centrifuge and kept in DI H<sub>2</sub>O before shell growth synthesis. The synthesis of core-shell ZSM-11 follows a previously published protocol [22]. The shell growth solution is 14 TBAOH:  $x$  SiO<sub>2</sub>: 9500 H<sub>2</sub>O with  $x$  varied in the range of 17-30 to control shell thickness. The synthesis was performed at 100°C for 1 d, followed by an annealing process with 14 TBAOH: 10 SiO<sub>2</sub>:

9500 H<sub>2</sub>O. The growth solution was aged for 24 h before silicalite-2 core was added to get a 1 wt% suspension. Crystals were isolated from the supernatant by three cycles of centrifugation, dried at room temperature in air, and then calcined in muffle furnace at 550 °C (heating and cooling rates of 1 °C min<sup>-1</sup>) for 5 h. Ion exchange was performed three times using a 1 M NH<sub>4</sub>NO<sub>3</sub> solution (2 wt% of calcined samples in solutions), which was heated at 80 °C under continuous stirring for 2 h. The exchanged samples were dried and calcined by the same procedure described above to obtain H-form zeolites.

#### **4.2.3 Characterization of ZSM-11 zeolites**

Powder X-ray diffraction (XRD) patterns were collected on a Rigaku diffractometer using Cu K $\alpha$  radiation (40kV, 40 mA) to verify the crystallinity and topology of the catalysts. Nitrogen physisorption experiments were performed on a Micromeritics ASAP 2020 instrument at 77 K to calculate micropore volumes (t-plot method) and BET surface area. Transient sorption experiments with 2,3-dimethylbutane were performed, and collected data was fitted following a previously reported procedure [24, 148] to obtain the characteristic diffusion timescale  $R^2/D$ . Scanning electron microscopy (SEM) was done on a GEMINI FE-SEM system. The overall Si/Al ratio was determined by inductively coupled plasma optical emission spectrometry (ICP-OES) analysis at Galbraith Laboratories (Knoxville, TN). Energy dispersive X-ray spectroscopy (EDX) was performed using a JEOL SM-31010/METEK EDAX system at 15 kV and 15 mm working distance. X-ray photoelectron spectroscopy (XPS) analysis of samples was performed using a PHI 5800 ESCA (Physical Electronics) multitechnique system

equipped with a standard an achromatic Al K $\alpha$  X-ray source (1486.6 eV) operating at 300 W (15 kV and 20 mA) and a concentric hemispherical analyzer. The equipment neutralizer component was utilized to reduce charging effects. All data were collected at a 45° takeoff angle.

#### 4.2.4 Characterization of core and shell composition in ZSM-11 zeolites

We used a combination of two elemental analysis techniques, EDX and XPS, to characterize the spatial distribution of elements in ZSM-5 zeolites. The average bulk chemical composition of ZSM-5 crystals was estimated by EDX, which has a sampling depth around two micrometers. The chemical composition of the outer rim of zeolite crystals was evaluated by XPS, which is a surface-sensitive technique with a sampling depth of only a few nanometers. Using the atomic percentages of aluminum and silicon, we define the percentage of aluminum occupying tetrahedral (T) sites as

$$Al_i = \frac{(Al \text{ atom}\%)}{(Al \text{ atom}\%)+(Si \text{ atom}\%)}, \quad (4.1)$$

where  $i$  = bulk or surface based on EDX or XPS measurements, respectively. Herein, we use the ratio  $Al_{\text{surface}}/Al_{\text{bulk}}$  as a descriptor for the spatial aluminum distribution in ZSM-5 zeolites. When this ratio is greater than one, aluminum is disproportionately concentrated at the surface of ZSM-5 crystals compared to the bulk, leading to Al-zoning. On the contrary, a ratio less than one signifies Si-zoning.

#### 4.2.5 Characterization of Al gradient in ZSM-11 zeolites

We used variable kinetic energy X-ray photoelectron spectroscopy (VKE-XPS) to probe the change in Si and Al contents as a function of depth into the crystals. VKE-XPS was performed at NSLSII (Brookhaven National Laboratory, Upton, NY) at

beamline 7-ID-2 with an HAXPES endstation. The powder form of samples was deposited onto carbon taped with a thin layer of carbon coating to reduce charging effect. Samples were taped onto a sample holder rod and installed in the vacuum chamber overnight. A neutralizer was also used to further prevent shift in binding energy due to charging effect. An L2 plane mirror was used for large (mm scale) spot size for spectra collection, with pass energy of 500 eV and a take-off angle of 80°. Ag3d spectrum was collected after every photon energy change to calculate actual ionization energy. Each sample sweep was for 0.5 to 1 h with a time ratio of 1:30 of Si1s to Al1s. The collected spectra were integrated using the Scienta program (IgorPro), and the peak areas were subsequently corrected with Scofield cross-section (NIST XCOM database) for Si/Al calculation. Inelastic mean free path (IMFP,  $\lambda$ ) was calculated from corresponding Si1s and Al1s kinetic energy at each photon energy (eV) using relativistic equation TPP2M formula in the QUASES program) for SiO<sub>2</sub> and Al<sub>2</sub>O<sub>3</sub>. The information depth was then calculated from IMFP using the following equation:

$$\text{Information depth} = 3\lambda\cos(\theta_{\text{photoemission}}). \quad (4.2)$$

#### **4.2.6 Characterization of Al species and acid sites**

Aluminum speciation was determined from <sup>27</sup>Al MAS NMR spectra collected at a spinning frequency of 12.5 kHz, pulse of  $\pi/12$ , relaxation delay of 0.8s, and 4K scans at 11.7T on a JEOL ECA-500 spectrometer [127]. We quantified the total number of acid sites with temperature-programmed desorption of ammonia (NH<sub>3</sub>-TPD) on a Micromeritics Autochem II 2920 equipped with a TCD detector. Approximately 100 mg of catalyst sample was degassed for 1 h at 600 °C before being cooled down to 100

°C for ammonia adsorption. At saturation, the sample was flushed with He for 120 min before we ramped up the temperature to 600 °C at a rate of 10 °C /min while concurrently monitoring the desorbed ammonia with the TCD detector. To identify the types of acid sites (i.e., Lewis and Brønsted), we conducted pyridine-adsorbed Fourier-transform infrared spectroscopy (pyr. FTIR). We first collected background spectrum at room temperature for a high temperature cell equipped with KBr windows using a Nicolet 6700 FTIR spectrometer. Subsequently, approximately 20 mg of sample was pelletized and placed in the cell. The configuration was installed in the spectrometer and connected to heated N<sub>2</sub> gas lines (150 °C). The cell was heated to 550 °C for 2 h to eliminate adsorbed moisture in the sample before being cooled down to 200 °C for the adsorption experiment. Parent spectrum is collected before increment of 1 µl anhydrous pyridine (Sigma Aldrich) was injected into the heated N<sub>2</sub> stream (Matheson, 50 cm<sup>3</sup> min<sup>-1</sup>). Spectra were collected 5 min after each injection until saturation, and the final spectrum was collected after purging for 2 h with N<sub>2</sub>. The subtracted results from the final and parent spectra were analyzed using OMNIC software with peaks assigned to Brønsted and Lewis acid sites at 1545 and 1450 cm<sup>-1</sup>, respectively [200]. The corrected peak area was used to obtain the percentages of Brønsted and Lewis acid sites.

#### **4.2.7 Reaction testing**

Methanol-to-hydrocarbon (MTH) reaction was carried out in a 0.25 in. stainless steel tube installed in a Thermo Fisher furnace, equipped with a controller. All catalysts (40 – 60 mesh size) were diluted with silica gel (Davisol Grad 636; 35 – 60 mesh size) and held between two plugs of quartz wool. A K-type thermocouple (Omega

Engineering) was inserted into the stainless tube to measure the temperature of the bottom of the catalyst bed. Prior to the reaction, the catalyst bed was pretreated *in situ* at 550 °C for 3 h under flow of dried air (Matheson, 6 cm<sup>3</sup> min<sup>-1</sup> of O<sub>2</sub>, 24 cm<sup>3</sup> min<sup>-1</sup> of N<sub>2</sub>). The catalyst bed was then cooled to the reaction temperature, 350 °C. Methanol was fed by a syringe pump (Harvard Apparatus) into a heated inert gas stream of Ar (Matheson, UHP) to achieve a methanol partial pressure of 11.5 kPa. The molar space velocity is varied in the range of 0.5 – 1.8 s<sup>-1</sup> to achieve different contact times,  $\tau$ . First data point was collected after 20 min time on stream (TOS) at 3 different  $\tau$  for each sample. Reaction effluent was evaluated using an on-stream gas chromatograph (Agilent 7890B) equipped with a FID detector and an Agilent DB-1 capillary column. Methanol and dimethyl ether (DME) are considered as reactant with the conversion  $X$  defined as

$$X = [1 - C_{\text{eff}}/C_{\text{feed}}] \times 100\% \quad (4.3)$$

where  $C_{\text{eff}}$  is the concentration of both methanol and DME in the effluent and  $C_{\text{feed}}$  is the concentration of methanol in the feed. The selectivity  $S_i$  of hydrocarbon product  $i$  is defined as

$$S_i = [C_i/C_{\text{t,eff}}] \times 100\% \quad (4.4)$$

where  $C_i$  is the concentration of hydrocarbon  $i$  in the effluent and  $C_{\text{t,eff}}$  is the total concentration of hydrocarbons in the effluent. Linear regression was performed on initial conversion versus contact time ( $\tau$ ) curves and conversion versus time-on-stream curves to obtain  $dX/d\tau$  and  $dX/dt$ , respectively. Site loss yield is calculated using the following equation [146]:

$$-\frac{d\tau}{dt} = \frac{dX/dt}{dX/d\tau} \quad (4.5)$$

where  $dX/dt$  and  $dX/d\tau$  are the slopes from the linear regressions.

### 4.3 Results and discussion

Core-shell catalysts with a ZSM-11 core (Si/Al = 30) and a silicalite-2 shell were prepared according to a previously reported seeded growth protocol [22] using ZSM-11 seeds (sample C-30) with an apparent thickness of 300 nm in the [100] direction (**Figure 4.1b**). The ZSM-11 seeds were synthesized using 1,8-diaminooctane (DAO) as the organic structure-directing agent to produce pure MEL-type zeolite without MFI impurity [219]. Secondary growth of seeds was accomplished in siliceous growth mixtures where the silica content was modified to generate a set of core-shell catalysts with progressively increasing shell thickness.

**Table 4.1.** Physicochemical properties of H-ZSM-11 catalysts.

Sample <sup>a</sup>	R <sup>2</sup> /D (ks)	BET S <sub>A</sub> (m <sup>2</sup> /g)	V <sub>micro</sub> (cm <sup>3</sup> /g)	C <sub>acid</sub> <sup>c</sup> (μmol/g)	Al <sub>ratio</sub> S/B <sup>b</sup>	Acid type <sup>d</sup> (%)		-dτ/dt (mol <sub>H+</sub> /molC)
						B	L	
C-30	0.22	427	0.14	302	1.1	85	15	501
CS-60	0.08	420	0.14	273	0.6	89	11	74
CS-91	0.08	403	0.14	243	0.4	90	10	439
CS-133	0.17	437	0.15	210	0.3	84	16	885
H-45	0.12	408	0.14	244	1.0	77	23	102
H-55	0.30	427	0.14	193	1.0	73	27	377

<sup>a</sup> C = core, CS = core-shell (ZSM-11@silicalite-2); <sup>b</sup> S/B = surface-to-bulk Al ratio (calculated using the Si/Al from XPS compared to EDS for C-30); <sup>c</sup> NH<sub>3</sub>-TPD; <sup>d</sup> Measured by pyridine FTIR where B = Brønsted acid sites and L = Lewis acid sites.

We prepared three core-shell samples that are labelled as CS-x, where x is the Si/Al

ratio of the shell measured by laboratory X-ray photoelectron spectroscopy (XPS). Table 4.1 lists the physicochemical properties of the core (C-30) and core-shell (CS-60, CS-91, and CS-133) samples. Textural analysis reveals nearly identical total surface area and micropore volume with adsorption and desorption curves shown in **Figure C1**. Acid site concentration and speciation was measured by a combination of techniques. Ammonia temperature programmed desorption (TPD) was used to calculate the total acid site concentration,  $C_{\text{acid}}$ . The percentage of acid type (Brønsted vs. Lewis acid) was measured by pyridine adsorption Fourier transform infrared (FTIR) spectroscopy. For this set of four samples, the concentration of acid sites monotonically decreases with increased shell thickness, as expected, but the speciation of acid sites is relatively constant.

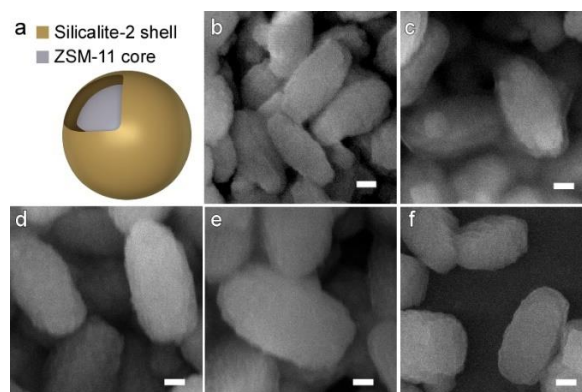


**Figure 4.1.** (a) Scheme of a ZSM-11@silicalite-2 core-shell particle. (b-f) Scanning electron micrographs of the (b) core C-30, (c) core-shell CS-60, (d) core-shell CS-91, (e) core-shell C-133, and (f) homogeneous ZSM-11 H-55. Scale bars equal 200 nm.

Seeded growth of silicalite-2 shells does not appreciably alter the morphology of ZSM-11 crystals, as confirmed by scanning electron microscopy (SEM, **Figure 4.1b-e**). The shell thickness for samples prepared in this study does not exceed 50 nm; however, electron microscopy lacks the sensitivity to distinguish subtle differences in

shell thickness, whereas the anisotropic rod-like shape of the crystals precludes the use of more sensitive techniques, such as dynamic light scattering (DLS), to detect small changes in particle size. Here, the progressive increase in surface Si/Al ratio measured by XPS is an indication of increasing shell thickness. The ratio of aluminum in external rim of the catalyst (surface) relative to its interior (bulk) is extracted from XPS data for each sample and energy dispersive X-ray spectroscopy (EDS) data of the core (labelled as  $Al_{ratio}$  S/B in Table 4.1). Furthermore, the growth of shell does not contribute to new defects such as internal silanols as seen from the parent spectra from FTIR experiments (**Figure C2**). Comparatively, the homogeneous samples, notably H-55, have an obvious internal silanol peak at ca.  $3500\text{ cm}^{-1}$ . In order to extract Si/Al ratios as a function of depth, we used the synchrotron source at Brookhaven National Laboratory to conduct variable kinetic energy XPS (VKE-XPS). As shown in **Figure 4.2**, the Si/Al ratio is reported for each sample as a function of both photon energy (bottom x-axis) and estimated information depth (top x-axis). This data confirms the increase in shell Si/Al ratio with the progressive increase in shell thickness. Our findings also reveal that secondary growth does not result in pure silicalite-2 owing to the possible reallocation of aluminum from the seed (core) to the shell during hydrothermal synthesis. As such, the shell never achieves complete surface passivation, although the concentration of Al sites in the shell are diluted by as much as 4-fold compared to the seed. An identical outcome was reported in our previous study of ZSM-5@silicalite-1 synthesis in chapter 3.

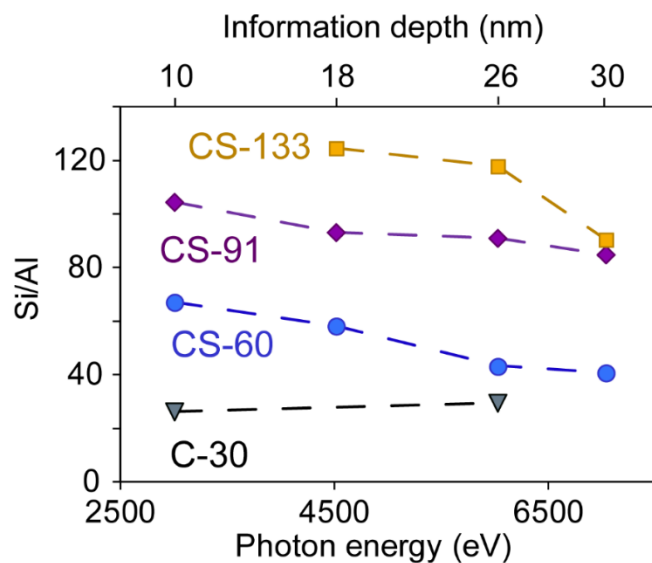


**Figure 4.2.** Comparison of Si/Al from XPS depth analysis (VKE-XPS) as a function of photon energy (bottom x-axis) and corresponding information depth (top x-axis).

Catalytic performance was assessed using the methanol to hydrocarbons (MTH) reaction. All reactions were conducted at sub-complete methanol conversion and 350 °C where the molar hourly space velocity was varied to achieve a starting conversion in the range of 50 to 70%. The slopes of conversion versus time-on-stream (**Figure 4.3a**), which are labelled as  $dX/dt$ , span an order of magnitude among all catalysts (ranging from 0.03 to 0.20  $h^{-1}$ ). Similar reactions were performed to assess changes in the initial conversion as a function of contact time  $\tau$  (**Figure 4.3b**), which was achieved by varying the space velocity. Comparisons are made for the core sample C-30 (inverted gray triangles), homogeneous sample H-60 (red triangles), and core-shell samples CS-60 (blue circles), CS-91 (purple diamonds), and CS-133 (gold squares). Dashed lines are linear regression with labelled slopes ( $dX/dt$  and  $dX/d\tau$ , respectively). The slopes of initial conversion versus contact time, labelled as  $dX/d\tau$ , are relatively similar for all

catalysts (ranging from 0.5 to 1.4 s<sup>-1</sup>). Janssens and coworkers [221] suggested the use of  $dX/dt$  as an assessment of catalyst deactivation in the MTH reaction is convoluted based on its inability to distinguish between loss of active sites and the intrinsic activity of sites. Bhan and coworkers [146] examined commercial ZSM-5 catalysts to expand upon the simple model introduced by Janssens wherein they empirically determined the quantity  $d\tau/dt$ , which is the ratio of  $dX/dt$  (Figure 3a) and  $dX/d\tau$  (**Figure 4.3b**). The physical significance of  $d\tau/dt$  is a site-loss yield (i.e., mole of H<sup>+</sup> loss for every mole of reactant fed), which is a more accurate parameter for comparing non-selective deactivation [222] of different catalysts. The measured site-loss yield for each catalyst in this study (**Table 4.1**) reveals that the coreshell with the thinnest shell (CS-60) loses active sites at a rate 7-fold lower than that of the core (C-30). As the thickness of the shell increases, the absolute value of  $d\tau/dt$  monotonically increases such that the coreshell catalyst with the largest thickness (CS-133) exhibits a 1.8-fold increase in loss of active sites relative to the parent core.

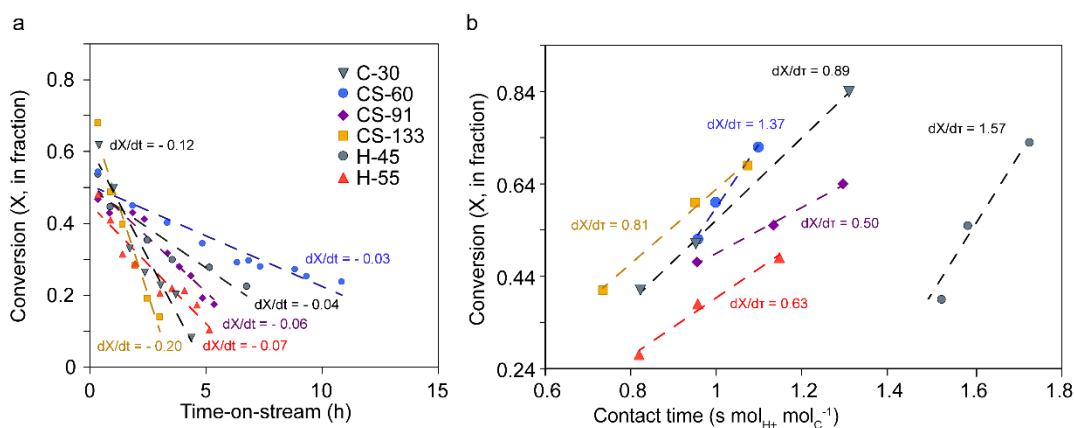


**Figure 4.3.** (a) Fractional conversion of MeOH and DME plotted as a function of time-on-stream  $t$ . (b) Initial conversion (at  $t = 20$  min) plotted as a function of contact time  $\tau$  (s mol<sub>H+</sub><sup>-1</sup> mol<sub>C</sub><sup>-1</sup>).

The performance of coreshell ZSM-11@silicalite-2 catalysts can be impacted by several factors, which include mass transport effects and dilution of total acid sites, among others not directly assessed in this study. Mass transport is quantitatively assessed on the basis of the diffusional timescale,  $R^2/D$ , experimentally determined from transient adsorption of a probe molecule (2,3-dimethylbutane, DMB). Values of  $R^2/D$  for all catalysts (**Table 4.1**, **Figure C3**) indicate that the addition of a siliceous shell on the surface of a parent core reduces diffusion limitations, consistent with our previous study of MFI-type materials (i.e., both Si-zoned and coreshell ZSM-5@silicalite-1). The nearly 3-fold reduction in  $R^2/D$  for coreshell materials is lost when shell thickness becomes prohibitively large, indicating that thinner shells enhance catalyst performance (consistent with trends in  $dX/dt$  and  $d\tau/dt$  in **Figure 4.3a** and **Table 4.1**, respectively). The impact of acid site dilution was assessed by preparing ZSM-11 catalysts with increasing Si/Al ratios where Al sites are homogeneously distributed throughout the catalyst. These samples are referred to as H- $x$  where  $x$  is the Si/Al ratio measured by EDX. For the two ZSM-11 samples prepared with reduced Al content (H-45 and H-55), catalyst lifetime increases relative to C-30. We also assessed differences in selectivity using a common mechanistic descriptor reported as the ratio of ethene (a characteristic product of the aromatic cycle) and the sum of 2-methylbutane and 2-methyl-2-butene (2MBu collectively), which are characteristic products of the olefin cycle [143]. Full selectivity profiles are provided in **Figure C4**. In our previous study of ZSM-5 surface passivation, we reported a trend in E/2MBu ratio with several catalyst properties that were combined into the descriptor  $C_{H+S_A^{-1}} R^2/D$ , where  $S_A$  is the BET surface area and

$C_{H^+}$  is the Brønsted acid concentration determined from  $\text{NH}_3$  TPD and pyridine FTIR. Here, each of these parameters were measured for all ZSM-11 and ZSM-11@silicalite-2 samples (Table 1). In **Figure 4.4**, we plot E/2MBu versus  $C_{H^+} S_A^{-1} R^2/D$  for catalysts in this study superimposed over previous data of ZSM-5 (green side triangles in **Figure 4.4**) where it is apparent that coreshell ZSM-11@silicalite-2 samples deviate from the trend (shaded region). Likewise, the homogenous ZSM-11 sample with highest Si/Al ratio (H-55) is an outlier (graytriangle in **Figure 4.4**).

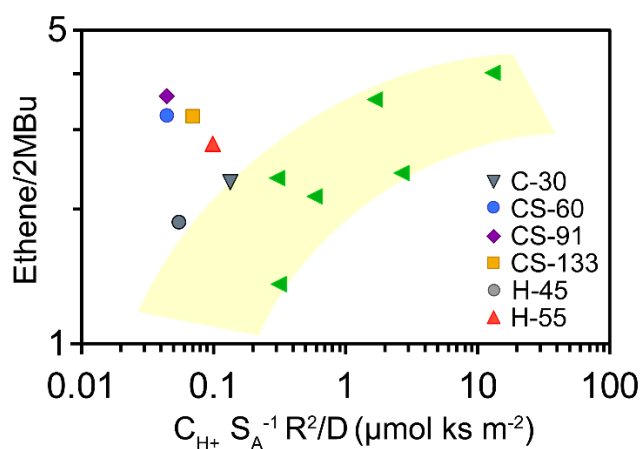


**Figure 4.4.** Initial E/2MBu at sub-conversion for MTH reactions over H-ZSM-11 plotted as a function of descriptor  $C_{H^+} S_A^{-1} R^2/D$ . Green side triangles marked data of homogeneous and zoned ZSM-5 in Chapter 3. Light yellow shaded area highlights general trend.

Here, we hypothesize potential reasons why coreshell MEL-type and H-55 samples deviate from a variety of zeolite catalysts that include homogeneous ZSM-11 (C-30 and H-45), homogenous ZSM-5, Si-zoned ZSM-5, and coreshell MFI-type samples. Bhan and coworkers [27, 148] previously examined the effect of crystallite size and Al content in ZSM-5 catalysts on ethene selectivity and reported that E/2MBu decreased with decreasing crystallite size and increasing Si/Al ratio, respectively. The dual effect of crystallite size and Al content were combined into one descriptor, similar to the one

used here, which represents the number of Al along a diffusion pathlength. An increase in Al content and crystallite size both increase the interaction the number of aromatic methylation/dealkylation events (i.e., interaction of methylbenzenes (MBs) with acid sites), leading to higher ethene selectivity. This trend is consistent with the homogeneous and zoned ZSM-5 samples (red triangles) and homogeneous samples ZSM-11 in this study, with the exception of H-55. However, the core-shell ZSM-11 samples deviate from this trend. The coreshell ZSM-11@silicalite-2 catalyst with the thinnest shell (CS-33) has increased catalyst lifetime and improved mass transport properties, which are both consistent with zeolites of smaller size, whereas its larger than expected E/2MBu ratio is more characteristic of zeolites with larger size and or higher overall acid site concentration. This apparent dichotomy defies trends observed for other zeolites. In a previous study on SAPO-34, we have shown that the imposition of diffusional constraints varies for different reactions within the complex MTO reaction network. For example, dehydrocyclization reactions experience stronger diffusion limitation than olefins methylation, methanol transfer hydrogenation, and aromatics dealkylation. Trends of increased cumulative selectivities of light alkanes (C<sub>1</sub>-C<sub>3</sub>) with increased diffusional constraints also reveal that it has a larger effect on olefins transfer hydrogenation than other reactions in the network. Indeed, the trend of deactivation and selectivities for core-shell ZSM-11 shown here suggests a dissimilarity in compositional gradients at the interior-exterior interface of the core-shell versus the Si-zoned samples from one-pot synthesis. This difference can impose different diffusional effect on different reactions within the MTH network. Our study suggests

further diffusional experiments with bulkier molecules (e.g., benzene, tertbutyl pyridine) capable of concurrently assessing internal diffusion and titrating acid sites are necessary to deconvolute different effect of compositional gradient in core-shell zeolites.

## CHAPTER 5

### 5.1 Current Research Summary

We have explored the dissolution of siliceous MFI zeolite (silicalite-1) with a combination of electron and scanning probe microscopy (in collaboration with Prof. Valtchev of ENSICAEN and Dr. Bozhilov of UC Riverside). Our findings reveal that dissolution initiates preferentially at lattice defects and progressively removes defect zones to reveal a mosaic structure of crystalline domains within each zeolite. In general, our study shows that time-resolved dissolution experiments allow us to elucidate the possible stages of zeolite MFI growth mechanism and is an efficient *ex situ* technique for revealing details about crystal growth features inaccessible by other methods.

We further expanded on the characterization of defects in relation to catalyst performance in the methanol-to-hydrocarbons (MTH) reaction whereby the effects of diffusion on catalyst lifetime and selectivity were compared for zeolites ZSM-5, ZSM-11, and SAPO-34 (in collaboration with Dr. Hwang and Prof. Bhan of the University of Minnesota). In these studies, the use of transient adsorption experiments of probe molecules (i.e., 2,3-dimethylbutane, 2,3-DMB) proved to be an effective assessment of mass transport. The measured diffusional timescale ( $R^2/D$ ) can account for topological irregularities and crystalline defects (unobservable by most conventional methods), which contribute to mass transport limitations. The diffusional timescale was further incorporated into a developed physicochemical descriptor that combines several key properties of the zeolite catalyst: Brønsted acid site concentration, BET surface area, and mass transport. These studies established a basis for catalyst assessment and

comparison, which can be broadly applied to a range of zeolite frameworks in MTH and potentially other reactions. The general understanding and utilization of descriptors to correlate structure-performance relationship allows for comprehensive investigation of the effect of mesoscopic compositional gradients on MTH catalytic performance using zoned ZSM-5 catalysts and their core-shell analogues. We reported one of the few instances of Si-zoned samples obtained from a one-pot synthesis and further demonstrated that the existence of a siliceous exterior region reduces diffusion limitations (i.e., reduced diffusional timescale,  $R^2/D$ ). We also showed that a siliceous exterior suppresses external coke development using operando UV-vis spectroscopy in collaboration with Nikolaos Nikolopoulos, Dr. Fu, and Prof. Weckhuysen of Utrecht University. These two factors contribute to improved catalyst lifetime (i.e., total turnover numbers) of Si-zoned ZSM-5 samples in relation to ZSM-5 samples with a homogeneous distribution of Al sites.

Lastly, we expanded upon studies of external surface passivation by examining the influence of siliceous shell thickness on the MTH reaction for core-shell ZSM-5 and ZSM-11 by synthesizing a set of ZSM-5@silicalite-1 and ZSM-11@silicalite-2 samples via secondary growth. Although we observed similar increase in catalyst lifetime for core-shell samples as with the Si-zoned samples, the product selectivity, assessed with a common descriptor, ethene/2MBu, deviates from the previous trend, with core-shell samples having higher ethene/2MBu ratios than the core sample. The higher ethene/2MBu ratio is not accompanied by an increase in aromatics selectivity and hydrogen transfer index (HTI), and hence, we posit that the increase in this ratio is partly

due to a higher ethene selectivity based on a reduction of non-selective reactions at the external surface. The difference in selectivity can also be associated with the dissimilarity in compositional gradients at the interior-exterior interface of the core-shell versus the Si-zoned sample. Our study suggests more detailed experiments with probe molecules capable of assessing internal diffusion and titrating acid sites are needed to further the understanding of compositional gradients in zeolites generated from secondary growth.

## **5.2 Future Outlook**

### **5.2.1 Zeolite secondary growth**

In our recent study of ZSM-5 and ZSM-11 we introduced a concept of finned zeolite catalysts wherein nano-crystalline zeolite domains are epitaxially grown over a zeolite particle of the same framework topology [7]. Although nanosized zeolites (sub 100 nm) can drastically reduce diffusion limitations for enhanced catalyst performance, the synthesis of nanosized single crystals is challenging and often results in low product yields. We offer an alternative approach of finned zeolite synthesis as a viable and facile method to enhance mass transport. We confirmed successful growth of finned zeolites for two frameworks, ZSM-5 and ZSM-11, in which the nano-crystalline zeolite domains (i.e., fins) are in the same crystallographic registry with the seeds. Extensive kinetic Monte Carlo modeling and time-resolved acid titration experiments also reveal substantial diffusion improvement, in line with catalytic testing results for MTH reactions. Catalytic behavior of finned catalysts is commensurate to that of a much smaller catalyst due to the existence of sub 50 nm fins. The concept of finned zeolites

can be applied to a larger range of frameworks to efficiently produce a new class of materials, pseudo nanocrystals, with enhanced catalytic performance.

### **5.2.2 Bifunctional zeolite catalysts**

As understanding of reaction mechanisms over heterogeneous catalysts becomes more expansive, it becomes crucial to rationally develop catalysts that can take advantage of these mechanistic knowledges. Oftentimes, catalysts possess diverse active sites that can promote different reactions. The design of bifunctional zeolite catalysts often involves the introduction of other framework heteroatoms or the incorporation of metal/metal-oxides via ion-exchange, vapor deposition, and incipient wetness impregnation [223-225]. Advancement in the area of multifunctional catalysts heavily relies on material synthesis as well-controlled incorporation of secondary active sites, which are nontrivial. Furthermore, due to the harsh synthesis conditions of zeolite frameworks (i.e., highly basic/caustic solutions, high pressure and temperature), bottom-up synthesis of bifunctional catalysts is challenging. As such, most bifunctional catalysts are produced via top-down methods; however, post synthesis modification of zeolites can inadvertently alter zeolite composition and Al speciation [226, 227]. Regardless, continued exploration of bottom-up synthesis can be beneficial. There have been elegant bottom up synthesis examples of multifunctional catalysts including single site Pt in K-LTL (zeolite L) [228] and the use of ligands or chelating agents to incorporate metal/metal oxides in various zeolite structures [229, 230].

#### **5.2.2.1 Core-shell Ammonia Slip Catalyst**

In my research, I have collaborated with Rajat Ghosh and Prof. Harold at the University of Houston in designing core-shell Pt/Al<sub>2</sub>O<sub>3</sub>@Cu/ZSM-5 for selective

oxidation of ammonia [231]. The core-shell catalyst mimics a commercial dual layered ammonia slip catalyst at a reduced scale which comprises of a Pt/Al<sub>2</sub>O<sub>3</sub> core responsible for oxidizing NH<sub>3</sub> and a Cu/ZSM-5 shell responsible for reducing NO<sub>x</sub>. The rational design of this catalyst involves an initial coating of Pt/Al<sub>2</sub>O<sub>3</sub> with a layer of silicalite-1 in milder synthesis condition (100°C) to prevent leaching before a ZSM-5 shell is grown over the coated core. The resulting bifunctional core-shell catalyst demonstrated better performance based on N<sub>2</sub> selectivity and light-off temperature compared to a physical mixture of Pt/Al<sub>2</sub>O<sub>3</sub> and Cu/ZSM-5. Although the resulting catalyst exhibits better performance and activity, the synthesis process is laborious with relatively low yield. Furthermore, the range of synthesis conditions is prohibitive due to possible disintegration or leaching of Pt/Al<sub>2</sub>O<sub>3</sub>. This study, however, is a starting point for further exploration of a single particle ammonia slip catalyst (ASC). Future studies should focus on (i) achieving a core-shell ASC catalyst with Cu/SSZ-13 shell, which is the preferred catalyst for NO<sub>x</sub> reduction and (ii) understanding of the effect of shell synthesis on Pt activity in the core.

#### **5.2.2.2 Bifunctional Y<sub>2</sub>O<sub>3</sub>/SAPO-34 catalyst for MTH reaction**

In the realm of methanol-to-hydrocarbons reactions, there are relatively fewer studies of bifunctional catalysts. The majority of studies reporting improved catalytic lifetime center around decreasing mass transport limitations via synthesis of nano-sized, nanosheet, or mesoporous zeolites. In some studies, incorporation of heteroatoms, metals (e.g., Ga, Ag, Zn), or metal oxides is a strategic approach to promote benzene-toluene-xylene (BTX) selectivity [21, 232, 233].

Alternatively, improvement of catalyst lifetime can also be achieved by limiting the

formation of formaldehyde, a known coke accelerant in MTH. Various methods have been proposed to limit formaldehyde formation, which include utilizing dimethyl ether (DME) instead of methanol as feed, seeding the hydrocarbon pool [234], and scavenging formed formaldehyde with rare-earth metal oxide placed in proximity with Brønsted acid sites [235]. The use of rare-earth metal oxides (e.g.,  $Y_2O_3$ ) [235] in MTH is accomplished by mixing and pelletizing it with the zeolite catalyst or by incipient wetness impregnation. Bhan and coworkers have demonstrated that the proximity of the rare-earth metal oxide,  $Y_2O_3$ , to the Brønsted acid sites of zeolites can improve catalytic lifetime, especially in SAPO-34 [235]. Indeed, spatial organization of metal active sites and acid sites can influence the reaction pathways, as demonstrated for hydroisomerization of light alkanes [236]. In this aspect, it can be especially beneficial to further reduce the distance between the Brønsted acid sites and the basic sites of  $Y_2O_3$  via top-down or bottom-up synthesis strategies. Due to the more complex composition of SAPO-34 compared to aluminosilicates and the sensitivity of acid site activity to synthesis conditions [25], a post-synthesis modification method such as mesopores generation to incorporate  $Y_2O_3$  particles can be difficult. Notably, the synthesis of ca. 10 nm or smaller  $Y_2O_3$  is nontrivial, and the acid site speciation of SAPO-34 cannot be effectively controlled during post synthesis treatment. On the other hand, bottom-up synthesis of  $Y_2O_3$ /SAPO-34 has not been reported, but it can open a new pathway for the rational design of bifunctional zeolite catalysts and can be interesting from a synthesis perspective. Below, I propose a few techniques that could help achieve this objective.

Firstly, to facilitate dispersion of  $Y_2O_3$  in the zeolite framework,  $Y_2O_3$  particles can initially be functionalized with a silane compound before seeding into SAPO-34 synthesis solution. Silane compounds must be chosen judiciously to not only functionalize  $Y_2O_3$  but to also enable crystallization of SAPO-34. A promising candidate is (2-diethylphosphatoethyl)methyldiethoxysilane (DPTES), which has been shown to successfully produce SAPO-34 by a Mobil patent [237]. DPTES is a phosphate functional trialkoxy silane with a silane group for functionalization of  $Y_2O_3$  and a phosphate group that can facilitate linkage to the SAPO-34 framework during synthesis. A preliminary experiment has shown that SAPO-34 can be crystallized using DPTES with the following recipe: 1 TEAOH: 0.25  $Al_2O_3$ : 0.11  $SiO_2$ : 0.30  $P_2O_5$ : 6  $H_2O$  at 235°C under rotation for 24 h (modified according to the Mobil patent). Commercial  $Y_2O_3$  (ca. 50 nm, Sigma Aldrich) was functionalized with 5-20 mmol of DPTES in anhydrous toluene (110°C for 10 h under stirring), dried, and seeded into SAPO-34 solution (2 wt% of total solution) before hydrothermal synthesis. To confirm the existence of  $Y_2O_3$  in the resulting product,  $CO_2$ -TPD was performed to probe the quantity of basic sites with measurement also done on a parent SAPO-34 as a control. The synthesized  $Y_2O_3$ /SAPO-34 does show a noticeable increase in  $CO_2$  desorbed; however, the amount is minimal. The negligible amount of  $CO_2$  detected can be an indication that the DPTES functionalization method requires further optimization and/or there are initially not enough basic sites in the commercial  $Y_2O_3$ . Instead,  $Y_2O_3$  particles can be synthesized via co-precipitation method to better control its morphology and concentration of basic sites [238]. Alternatively, to improve dispersion of  $Y_2O_3$  in a bottom up synthesis, a

soluble  $Y^{3+}$  – chelating agent complex can be introduced into the above SAPO-34 synthesis solution. Yttrium nitrate hexahydrate ( $Y(NO_3)_3 \cdot 6H_2O$ ) cannot be directly added to the synthesis solution as it can quickly precipitate in the presence of high tetraethylammonium hydroxide (TEAOH). As such, the chosen chelating agent must be able to stabilize the  $Y^{3+}$  cation against precipitation in the alkaline zeolite synthesis solution. Preliminary results from my experiment have shown that diethylenetriaminepentaacetic acid (DTPA), an expanded version of ethylenediaminetetraacetic acid (EDTA), but with a higher stability constant, can effectively stabilize  $Y^{3+}$  at a 2:1 mole ratio of DTPA to yttrium in the SAPO-34 solution listed above. To facilitate the formation of SAPO-34, a phosphonate version of DTPA, diethylenetriaminepentakis(methylphosphonic acid) (DTPMP), can also be used. The presence of phosphonic groups can perhaps promote bridging with SAPO-34 precursors to improve yttrium incorporation into the crystallized zeolites.

The outlined strategies I have proposed here for  $Y_2O_3$ /SAPO-34 are novel and promising. I anticipate continued pursuit and fine-tuning of these synthesis strategies will result in facile, well-controlled, one-pot synthesis of high performing bifunctional catalysts for methanol-to-hydrocarbon reactions.

## REFERENCES

- [1] D. Fu, O. van der Heijden, K. Stanciakova, J.E. Schmidt, B.M. Weckhuysen, "Disentangling reaction processes of zeolites within single-oriented channels," *Angew. Chem. Int. Ed.*, 59 (2020) 15502-15506.
- [2] W. Fan, M.A. Snyder, S. Kumar, P.S. Lee, W.C. Yoo, A.V. McCormick, R.L. Penn, A. Stein, M. Tsapatsis, "Hierarchical nanofabrication of microporous crystals with ordered mesoporosity," *Nat. Mater.*, 7 (2008) 984-991.
- [3] A.I. Lupulescu, M. Kumar, J.D. Rimer, "A facile strategy to design zeolite L crystals with tunable morphology and surface architecture," *J. Am. Chem. Soc.*, 135 (2013) 6608-6617.
- [4] K. Na, M. Choi, R. Ryoo, "Cyclic diquatery ammoniums for nanocrystalline BEA, MTW and MFI zeolites with intercrystalline mesoporosity," *Journal of Materials Chemistry*, 19 (2009) 6713-6719.
- [5] X. Zhang, D. Liu, D. Xu, S. Asahina, K.A. Cychosz, K.V. Agrawal, Y. Al Wahedi, A. Bhan, S. Al Hashimi, O. Terasaki, M. Thommes, M. Tsapatsis, "Synthesis of self-pillared zeolite nanosheets by repetitive branching," *Science*, 336 (2012) 1684-1687.
- [6] S.H. Keoh, W. Chaikittisilp, K. Muraoka, R.R. Mukti, A. Shimojima, P. Kumar, M. Tsapatsis, T. Okubo, "Factors Governing the Formation of Hierarchically and Sequentially Intergrown MFI Zeolites by Using Simple Diquaternary Ammonium Structure-Directing Agents," *Chemistry of Materials*, 28 (2016) 8997-9007.

- [7] H. Dai, Y. Shen, T. Yang, C. Lee, D. Fu, A. Agarwal, T.T. Le, M. Tsapatsis, J.C. Palmer, B.M. Weckhuysen, P.J. Dauenhauer, X. Zou, J.D. Rimer, "Finned zeolite catalysts," *Nat. Mater.*, (2020).
- [8] J.R. Di Iorio, R. Gounder, "Controlling the Isolation and Pairing of Aluminum in Chabazite Zeolites Using Mixtures of Organic and Inorganic Structure-Directing Agents," *Chemistry of Materials*, 28 (2016) 2236-2247.
- [9] A. Chawla, R. Li, R. Jain, R.J. Clark, J.G. Sutjianto, J.C. Palmer, J.D. Rimer, "Cooperative effects of inorganic and organic structure-directing agents in ZSM-5 crystallization," *Mol. Syst. Des. Eng.*, 3 (2018) 159-170.
- [10] J. Dedecek, V. Balgová, V. Pashkova, P. Klein, B. Wichterlová, "Synthesis of ZSM-5 Zeolites with Defined Distribution of Al Atoms in the Framework and Multinuclear MAS NMR Analysis of the Control of Al Distribution," *Chem. Mater.*, 24 (2012) 3231-3239.
- [11] J.R. Di Iorio, S. Li, C.B. Jones, C.T. Nimlos, Y. Wang, E. Kunkes, V. Vattipalli, S. Prasad, A. Moini, W.F. Schneider, R. Gounder, "Cooperative and Competitive Occlusion of Organic and Inorganic Structure-Directing Agents within Chabazite Zeolites Influences Their Aluminum Arrangement," *J. Am. Chem. Soc.*, 142 (2020) 4807-4819.
- [12] C. Li, A. Vidal-Moya, P.J. Miguel, J. Dedecek, M. Boronat, A. Corma, "Selective Introduction of Acid Sites in Different Confined Positions in ZSM-5 and Its Catalytic Implications," *ACS Catal.*, 8 (2018) 7688-7697.

- [13] P. Sazama, J. Dědeček, V. Gábová, B. Wichterlová, G. Spoto, S. Bordiga, "Effect of Aluminium Distribution in the Framework of ZSM-5 on Hydrocarbon Transformation. Cracking of 1-Butene," *J. Catal.*, 254 (2008) 180-189.
- [14] J.R. Di Iorio, C.T. Nimlos, R. Gounder, "Introducing Catalytic Diversity into Single-site Chabazite Zeolites of Fixed Composition via Synthetic Control of Active Site Proximity," *ACS Catal.*, 7 (2017) 6663-6674.
- [15] Z. Yu, S. Li, Q. Wang, A. Zheng, X. Jun, L. Chen, F. Deng, "Brønsted/Lewis Acid Synergy in H-ZSM-5 and H-MOR Zeolites Studied by  $^1\text{H}$  and  $^{27}\text{Al}$  DQ-MAS Solid-State NMR Spectroscopy," *J. Phys. Chem. C*, 115 (2011) 22320-22327.
- [16] R. Gounder, A.J. Jones, R.T. Carr, E. Iglesia, "Solvation and Acid Strength Effects on Catalysis by Faujasite Zeolites," *J. Catal.*, 286 (2011) 214-223.
- [17] X. Yi, K. Liu, W. Chen, J. Li, S. Xu, C. Li, Y. Xiao, H. Liu, X. Guo, S.-B. Liu, A. Zheng, "Origin and Structural Characteristics of Tri-coordinated Extra-framework Aluminum Species in Dealuminated Zeolites," *J. Am. Chem. Soc.*, 140 (2018) 10764-10774.
- [18] J.C. Groen, T. Bach, U. Ziese, A.M. Paulaime-van Donk, K.P. de Jong, J.A. Moulijn, J. Pérez-Ramírez, "Creation of Hollow Zeolite Architectures by Controlled Desilication of Al-Zoned ZSM-5 Crystals," *J. Am. Chem. Soc.*, 127 (2005) 10792-10793.
- [19] N. Danilina, F. Krumeich, S.A. Castelanelli, J.A. van Bokhoven, "Where are the active sites in zeolites? Origin of aluminum zoning in ZSM-5," *J. Phys. Chem. C*, 114 (2010) 6640-6645.

- [20] L. Karwacki, M.H.F. Kox, D.A. Matthijs de Winter, M.R. Drury, J.D. Meeldijk, E. Stavitski, W. Schmidt, M. Mertens, P. Cubillas, N. John, A. Chan, N. Kahn, S.R. Bare, M. Anderson, J. Kornatowski, B.M. Weckhuysen, "Morphology-Dependent Zeolite Intergrowth Structures Leading to Distinct Internal and Outer-Surface Molecular Diffusion Barriers," *Nat. Mater.*, 8 (2009) 959-965.
- [21] K. Miyake, Y. Hirota, K. Ono, Y. Uchida, S. Tanaka, N. Nishiyama, "Direct and Selective Conversion of Methanol to Para-Xylene over Zn Ion Doped ZSM-5/silicalite-1 Core-Shell Zeolite Catalyst," *J. Catal.*, 342 (2016) 63-66.
- [22] A. Ghorbanpour, A. Gumidyala, L.C. Grabow, S.P. Crossley, J.D. Rimer, "Epitaxial growth of ZSM-5@Silicalite-1: A core-shell zeolite designed with passivated surface acidity," *ACS Nano*, 9 (2015) 4006-4016.
- [23] A.D. Chowdhury, A.L. Paioni, K. Houben, G.T. Whiting, M. Baldus, B.M. Weckhuysen, "Bridging the Gap between the Direct and Hydrocarbon Pool Mechanisms of the Methanol-to-Hydrocarbons Process," *Angew. Chem. Int. Ed.*, 57 (2018) 8095-8099.
- [24] Y. Shen, T.T. Le, D. Fu, J.E. Schmidt, M. Filez, B.M. Weckhuysen, J.D. Rimer, "Deconvoluting the competing effects of zeolite framework topology and diffusion path length on methanol to hydrocarbons reaction," *ACS Catal.*, (2018) 11042-11053.
- [25] A. Hwang, T.T. Le, Z. Shi, H. Dai, J.D. Rimer, A. Bhan, "Effects of diffusional constraints on lifetime and selectivity in methanol-to-olefins catalysis on HSAPO-34," *J. Catal.*, 369 (2018) 122-132.

- [26] A.I. Lupulescu, J.D. Rimer, "In Situ Imaging of Silicalite-1 Surface Growth Reveals the Mechanism of Crystallization," *Science*, 344 (2014) 729.
- [27] R. Khare, Z.H. Liu, Y. Han, A. Bhan, "A mechanistic basis for the effect of aluminum content on ethene selectivity in methanol-to-hydrocarbons conversion on HZSM-5," *J. Catal.*, 348 (2017) 300-305.
- [28] C. Martínez, A. Corma, "Inorganic molecular sieves: Preparation, modification and industrial application in catalytic processes," *Coordination Chemistry Reviews*, 255 (2011) 1558-1580.
- [29] D. Oleksiak Matthew, D. Rimer Jeffrey, Synthesis of zeolites in the absence of organic structure-directing agents: factors governing crystal selection and polymorphism, in: *Reviews in Chemical Engineering*, 2014, pp. 1.
- [30] L. Tosheva, V.P. Valtchev, "Nanozeolites: Synthesis, crystallization mechanism, and applications," *Chem. Mater.*, 17 (2005) 2494-2513.
- [31] A.I. Lupulescu, J.D. Rimer, "In Situ Imaging of Silicalite-1 Surface Growth Reveals the Mechanism of Crystallization," *Science*, 344 (2014) 729-732.
- [32] S. Mintova, J. Grand, V. Valtchev, "Nanosized zeolites: Quo Vadis?," *Comptes Rendus Chimie*, 19 (2016) 183-191.
- [33] A.I. Lupulescu, W. Qin, J.D. Rimer, "Tuning Zeolite Precursor Interactions by Switching the Valence of Polyamine Modifiers," *Langmuir*, 32 (2016) 11888-11898.
- [34] A.I. Lupulescu, J.D. Rimer, "Tailoring Silicalite-1 Crystal Morphology with Molecular Modifiers," *Angew. Chem. Int. Ed.*, 51 (2012) 3345-3349.

- [35] M. Choi, K. Na, J. Kim, Y. Sakamoto, O. Terasaki, R. Ryoo, "Stable single-unit-cell nanosheets of zeolite MFI as active and long-lived catalysts," *Nature*, 461 (2009) 246-249.
- [36] W. Fan, M.A. Snyder, S. Kumar, P.-S. Lee, W.C. Yoo, A.V. McCormick, R. Lee Penn, A. Stein, M. Tsapatsis, "Hierarchical nanofabrication of microporous crystals with ordered mesoporosity," *Nat. Mater.*, 7 (2008) 984-991.
- [37] A.I. Lupulescu, M. Kumar, J.D. Rimer, "A Facile Strategy To Design Zeolite L Crystals with Tunable Morphology and Surface Architecture," *J. Am. Chem. Soc.*, 135 (2013) 6608-6617.
- [38] W. Chaikittisilp, Y. Suzuki, R.R. Mukti, T. Suzuki, K. Sugita, K. Itabashi, A. Shimojima, T. Okubo, "Formation of hierarchically organized zeolites by sequential intergrowth," *Angew. Chem. Int. Ed.*, 52 (2013) 3355-3359.
- [39] H. Awala, J.-P. Gilson, R. Retoux, P. Boullay, J.-M. Goupil, V. Valtchev, S. Mintova, "Template-free nanosized faujasite-type zeolites," *Nat. Mater.*, 14 (2015) 447-451.
- [40] E.-P. Ng, D. Chateigner, T. Bein, V. Valtchev, S. Mintova, "Capturing Ultrasmall EMT Zeolite from Template-Free Systems," *Science*, 335 (2012) 70-73.
- [41] A. Sachse, A. Grau-Atienza, E.O. Jardim, N. Linares, M. Thommes, J. García-Martínez, "Development of intracrystalline mesoporosity in zeolites through surfactant-templating," *Cryst. Growth Des.*, 17 (2017) 4289-4305.

- [42] N.D. Petkovich, A. Stein, "Controlling macro- and mesostructures with hierarchical porosity through combined hard and soft templating," *Chem. Soc. Rev.*, 42 (2013) 3721-3739.
- [43] D. Liu, A. Bhan, M. Tsapatsis, S. Al Hashimi, "Catalytic Behavior of Brønsted Acid Sites in MWW and MFI Zeolites with Dual Meso- and Microporosity," *ACS Catal.*, 1 (2011) 7-17.
- [44] J.D. Rimer, M. Kumar, R. Li, A.I. Lupulescu, M.D. Oleksiak, "Tailoring the physicochemical properties of zeolite catalysts," *Catal. Sci. Technol.*, 4 (2014) 3762-3771.
- [45] K.N. Olafson, R. Li, B.G. Alamani, J.D. Rimer, "Engineering Crystal Modifiers: Bridging Classical and Nonclassical Crystallization," *Chem. Mater.*, 28 (2016) 8453-8465.
- [46] M. Kumar, H. Luo, Y. Román-Leshkov, J.D. Rimer, "SSZ-13 Crystallization by Particle Attachment and Deterministic Pathways to Crystal Size Control," *Journal of the American Chemical Society*, 137 (2015) 13007-13017.
- [47] S. Jegatheeswaran, C.-M. Cheng, C.-H. Cheng, "Effects of adding alcohols on ZSM-12 synthesis," *Microporous Mesoporous Mater.*, 201 (2015) 24-34.
- [48] A.K. Jamil, O. Muraza, A.M. Al-Amer, "The role of alcohols and diols as co-solvents in fabrication of TON zeolite," *Journal of Industrial and Engineering Chemistry*, 29 (2015) 112-119.

- [49] M.A. Sanhoob, O. Muraza, E.M. Al-Mutairi, N. Ullah, "Role of crystal growth modifiers in the synthesis of ZSM-12 zeolite," *Adv. Powder Technol.*, 26 (2015) 188-192.
- [50] R. Das, S. Ghosh, M. Kanti Naskar, "Effect of secondary and tertiary alkylamines for the synthesis of Zeolite L," *Materials Letters*, 143 (2015) 94-97.
- [51] A. Chawla, R. Li, R. Jain, R.J. Clark, J.G. Sutjianto, J. Palmer, J.D. Rimer, "Cooperative Effects of Inorganic and Organic Structure-Directing Agents in ZSM-5 Crystallization," *Molecular Systems Design & Engineering*, (2017).
- [52] Y. Shen, T.T. Le, R. Li, J.D. Rimer, "Optimized Synthesis of ZSM-11 Catalysts using 1,8-Diaminooctane as a Structure-Directing Agent," *ChemPhysChem*, n/a-n/a.
- [53] K. Na, C. Jo, J. Kim, K. Cho, J. Jung, Y. Seo, R.J. Messinger, B.F. Chmelka, R. Ryoo, "Directing Zeolite Structures into Hierarchically Nanoporous Architectures," *Science*, 333 (2011) 328-332.
- [54] H.Y. Luo, V.K. Michaelis, S. Hodges, R.G. Griffin, Y. Roman-Leshkov, "One-pot synthesis of MWW zeolite nanosheets using a rationally designed organic structure-directing agent," *Chem. Sci.*, 6 (2015) 6320-6324.
- [55] G. Bonilla, I. Díaz, M. Tsapatsis, H.-K. Jeong, Y. Lee, D.G. Vlachos, "Zeolite (MFI) Crystal Morphology Control Using Organic Structure-Directing Agents," *Chem. Mater.*, 16 (2004) 5697-5705.
- [56] A. Corma, V. Fornes, S.B. Pergher, T.L.M. Maesen, J.G. Buglass, "Delaminated zeolite precursors as selective acidic catalysts," *Nature*, 396 (1998) 353-356.

- [57] I. Ogino, M.M. Nigra, S.-J. Hwang, J.-M. Ha, T. Rea, S.I. Zones, A. Katz, "Delamination of Layered Zeolite Precursors under Mild Conditions: Synthesis of UCB-1 via Fluoride/Chloride Anion-Promoted Exfoliation," *Journal of the American Chemical Society*, 133 (2011) 3288-3291.
- [58] Y. Zhou, Y. Mu, M.-F. Hsieh, B. Kabius, C. Pacheco, C. Bator, R.M. Rioux, J.D. Rimer, "Enhanced Surface Activity of MWW Zeolite Nanosheets Prepared via a One-Step Synthesis," *J. Am. Chem. Soc.*, 142 (2020) 8211-8222.
- [59] A. Corma, V. Fornés, J. Martínez-Triguero, S.B. Pergher, "Delaminated Zeolites: Combining the Benefits of Zeolites and Mesoporous Materials for Catalytic Uses," *J. Catal.*, 186 (1999) 57-63.
- [60] K. Varoon, X. Zhang, B. Elyassi, D.D. Brewer, M. Gettel, S. Kumar, J.A. Lee, S. Maheshwari, A. Mittal, C.-Y. Sung, M. Cococcioni, L.F. Francis, A.V. McCormick, K.A. Mkhoyan, M. Tsapatsis, "Dispersible Exfoliated Zeolite Nanosheets and Their Application as a Selective Membrane," *Science*, 334 (2011) 72-75.
- [61] M.Y. Jeon, D. Kim, P. Kumar, P.S. Lee, N. Rangnekar, P. Bai, M. Shete, B. Elyassi, H.S. Lee, K. Narasimharao, S.N. Basahel, S. Al-Thabaiti, W. Xu, H.J. Cho, E.O. Fetisov, R. Thyagarajan, R.F. DeJaco, W. Fan, K.A. Mkhoyan, J.I. Siepmann, M. Tsapatsis, "Ultra-selective high-flux membranes from directly synthesized zeolite nanosheets," *Nature*, 543 (2017) 690-694.
- [62] M. Moliner, F. Rey, A. Corma, "Towards the Rational Design of Efficient Organic Structure-Directing Agents for Zeolite Synthesis," *Angew. Chem. Int. Ed.*, 52 (2013) 13880-13889.

- [63] R. Li, N. Linares, J.G. Sutjianto, A. Chawla, J. Garcia-Martinez, J.D. Rimer, "Ultrasmall Zeolite L Crystals Prepared from Highly Interdispersed Alkali-Silicate Precursors," *Angew. Chem. Int. Ed.*, 57 (2018) 11283-11288.
- [64] S. Li, J. Li, M. Dong, S. Fan, T. Zhao, J. Wang, W. Fan, "Strategies to Control Zeolite Particle Morphology," *Chem. Soc. Rev.*, 48 (2019) 885-907.
- [65] B.C. Knott, C.T. Nimlos, D.J. Robichaud, M.R. Nimlos, S. Kim, R. Gounder, "Consideration of the Aluminum Distribution in Zeolites in Theoretical and Experimental Catalysis Research," *ACS Catal.*, 8 (2018) 770-784.
- [66] A. Ghorbanpour, J.D. Rimer, L.C. Grabow, "Computational Assessment of the Dominant Factors Governing the Mechanism of Methanol Dehydration over H-ZSM-5 with Heterogeneous Aluminum Distribution," *ACS Catal.*, 6 (2016) 2287-2298.
- [67] W. Haag, R. Lago, P. Weisz, "The Active Site of Acidic Aluminosilicate Catalysts," *Nature*, 309 (1984) 589-591.
- [68] S. Bordiga, C. Lamberti, F. Bonino, A. Travert, F. Thibault-Starzyk, "Probing Zeolites by Vibrational Spectroscopies," *Chem. Soc. Rev.*, 44 (2015) 7262-7341.
- [69] A.J. Jones, E. Iglesia, "The Strength of Brønsted Acid Sites in Microporous Aluminosilicates," *ACS Catal.*, 5 (2015) 5741-5755.
- [70] S. Nystrom, A. Hoffman, D. Hibbitts, "Tuning Brønsted Acid Strength by Altering Site Proximity in CHA Framework Zeolites," *ACS Catal.*, 8 (2018) 7842-7860.
- [71] A. Ghorbanpour, J.D. Rimer, L.C. Grabow, "Periodic, vdW-Corrected Density Functional Theory Investigation of the Effect of Al Siting in H-ZSM-5 on

Chemisorption Properties and Site-specific Acidity," *Catal. Commun.*, 52 (2014) 98-102.

[72] M. Boronat, A. Corma, "What Is Measured When Measuring Acidity in Zeolites with Probe Molecules?," *ACS Catal.*, 9 (2019) 1539-1548.

[73] T. Nishitoba, N. Yoshida, J.N. Kondo, T. Yokoi, "Control of Al Distribution in the CHA-Type Aluminosilicate Zeolites and Its Impact on the Hydrothermal Stability and Catalytic Properties," *Ind. Eng. Chem. Res.*, 57 (2018) 3914-3922.

[74] J. Devos, M.L. Bols, D. Plessers, C. Van Goethem, J.W. Seo, S.-J. Hwang, B.F. Sels, M. Dusselier, "Synthesis-Structure-Activity Relations in Fe-CHA for C-H Activation: Control of Al-Distribution by Interzeolite Conversion," *Chem. Mater.*, 32 (2019) 273-285.

[75] S. Kim, G. Park, M.H. Woo, G. Kwak, S.K. Kim, "Control of Hierarchical Structure and Framework-Al Distribution of ZSM-5 via Adjusting Crystallization Temperature and Their Effects on Methanol Conversion," *ACS Catal.*, (2019) 2880-2892.

[76] M.D. Oleksiak, K. Muraoka, M.F. Hsieh, M.T. Conato, A. Shimojima, T. Okubo, W. Chaikittisilp, J.D. Rimer, "Organic-Free Synthesis of a Highly Siliceous Faujasite Zeolite with Spatially Biased Q4 (nAl) Si Speciation," *Angew. Chem. Int. Ed.*, 129 (2017) 13551-13556.

[77] R. Li, A. Chawla, N. Linares, J.G. Sutjianto, K.W. Chapman, J.G. Martínez, J.D. Rimer, "Diverse Physical States of Amorphous Precursors in Zeolite Synthesis," *Ind. Eng. Chem. Res.*, 57 (2018) 8460-8471.

- [78] A. Chawla, N. Linares, R. Li, J. García-Martínez, J.D. Rimer, "Tracking Zeolite Crystallization by Elemental Mapping," *Chem. Mater.*, 32 (2020) 3278-3287.
- [79] T. Yokoi, H. Mochizuki, S. Namba, J.N. Kondo, T. Tatsumi, "Control of the Al Distribution in the Framework of ZSM-5 Zeolite and Its Evaluation by Solid-State NMR Technique and Catalytic Properties," *Journal of Physical Chemistry C*, 119 (2015) 15303-15315.
- [80] J. Dědeček, E. Tabor, S. Sklenak, "Tuning the Aluminum Distribution in Zeolites to Increase their Performance in Acid-Catalyzed Reactions," *ChemSusChem*, 12 (2019) 556-576.
- [81] A. Vjunov, J.L. Fulton, T. Huthwelker, S. Pin, D. Mei, G.K. Schenter, N. Govind, D.M. Camaioni, J.Z. Hu, J.A. Lercher, "Quantitatively Probing the Al Distribution in Zeolites," *J. Am. Chem. Soc.*, 136 (2014) 8296-8306.
- [82] J.A. Van Bokhoven, T.L. Lee, M. Drakopoulos, C. Lamberti, S. Thie, J. Zegenhagen, "Determining the Aluminium Occupancy on the Active T-Sites in Zeolites Using X-ray Standing Waves," *Nat. Mater.*, 7 (2008) 551-555.
- [83] R. Bohinc, J. Hoszowska, J.C. Dousse, W. Błachucki, F. Zeeshan, Y. Kayser, M. Nachtegaal, A.B. Pinar, J.A. Van Bokhoven, "Distribution of Aluminum over Different T-Sites in Ferrierite Zeolites Studied with Aluminum Valence to Core X-ray Emission Spectroscopy," *Phys. Chem. Chem. Phys.*, 19 (2017) 29271-29277.
- [84] A.B. Pinar, L. Gómez-Hortigüela, L.B. McCusker, J. Pérez-Pariente, "Controlling the Aluminum Distribution in the Zeolite Ferrierite via the Organic Structure Directing Agent," *Chem. Mater.*, 25 (2013) 3654-3661.

- [85] M. Kumar, Z.J. Berkson, J.R. Clark, Y. Shen, N.A. Prisco, Q. Zheng, Z. Zeng, H. Zheng, L.B. McCusker, J.C. Palmer, B.F. Chmelka, J.D. Rimer, "Crystallization of Mordenite Platelets using Cooperative Organic Structure-Directing Agents," *J. Am. Chem. Soc.*, 141 (2019) 20155-20165.
- [86] D.E. Perea, I. Arslan, J. Liu, Z. Ristanović, L. Kovarik, B.W. Arey, J.A. Lercher, S.R. Bare, B.M. Weckhuysen, "Determining the Location and Nearest Neighbours of Aluminium in Zeolites with Atom Probe Tomography," *Nat. Commun.*, 6 (2015) 1-8.
- [87] J. Dedecek, M.J. Lucero, C. Li, F. Gao, P. Klein, M. Urbanova, Z. Tvaruzkova, P. Sazama, S. Sklenak, "Complex Analysis of the Aluminum Siting in the Framework of Silicon-rich Zeolites. A Case Study on Ferrierites," *Journal of Physical Chemistry C*, 115 (2011) 11056-11064.
- [88] L. Čapek, J. Dědeček, P. Sazama, B. Wichterlová, "The decisive role of the distribution of Al in the framework of beta zeolites on the structure and activity of Co ion species in propane-SCR-NO<sub>x</sub> in the presence of water vapour," *J. Catal.*, 272 (2010) 44-54.
- [89] J. Dědeček, Z. Sobalík, B. Wichterlová, "Siting and Distribution of Framework Aluminium Atoms in Silicon-Rich Zeolites and Impact on Catalysis," *Catal. Rev.*, 54 (2012) 135-223.
- [90] A. Bhan, A.D. Allian, G.J. Sunley, D.J. Law, E. Iglesia, "Specificity of Sites within Eight-Membered Ring Zeolite Channels for Carbonylation of Methyls to Acetyls," *J. Am. Chem. Soc.*, 129 (2007) 4919-4924.

- [91] Y. Román-Leshkov, M. Moliner, M.E. Davis, "Impact of Controlling the Site Distribution of Al Atoms on Catalytic Properties in Ferrierite-Type Zeolites," *J. Phys. Chem. C*, 115 (2011) 1096-1102.
- [92] T. Liang, J. Chen, Z. Qin, J. Li, P. Wang, S. Wang, G. Wang, M. Dong, W. Fan, J. Wang, "Conversion of Methanol to Olefins over H-ZSM-5 Zeolite: Reaction Pathway Is Related to the Framework Aluminum Siting," *ACS Catal.*, 6 (2016) 7311-7325.
- [93] J. Chen, T. Liang, J. Li, S. Wang, Z. Qin, P. Wang, L. Huang, W. Fan, J. Wang, "Regulation of Framework Aluminum Siting and Acid Distribution in H-MCM-22 by Boron Incorporation and Its Effect on the Catalytic Performance in Methanol to Hydrocarbons," *ACS Catal.*, 6 (2016) 2299-2313.
- [94] A.J. Jones, E. Iglesia, "Kinetic, Spectroscopic, and Theoretical Assessment of Associative and Dissociative Methanol Dehydration Routes in Zeolites," *Angew. Chem. Int. Ed.*, 53 (2014) 12177-12181.
- [95] N. Kosinov, C. Liu, E.J.M. Hensen, E.A. Pidko, "Engineering of Transition Metal Catalysts Confined in Zeolites," *Chem. Mater.*, 30 (2018) 3177-3198.
- [96] C. Paolucci, A.A. Parekh, I. Khurana, J.R. Di Iorio, H. Li, J.D. Albarracin Caballero, A.J. Shih, T. Anggara, W.N. Delgass, J.T. Miller, "Catalysis in a Cage: Condition-Dependent Speciation and Dynamics of Exchanged Cu Cations in SSZ-13 Zeolites," *J. Am. Chem. Soc.*, 138 (2016) 6028-6048.
- [97] K.T. Dinh, M.M. Sullivan, K. Narsimhan, P. Serna, R.J. Meyer, M. Dincă, Y. Román-Leshkov, "Continuous Partial Oxidation of Methane to Methanol Catalyzed by

- Diffusion-Paired Copper Dimers in Copper-Exchanged Zeolites," *J. Am. Chem. Soc.*, 141 (2019) 11641-11650.
- [98] S. Sklenak, J. Dědeček, C. Li, B. Wichterlová, V. Gábová, M. Sierka, J. Sauer, "Aluminium siting in the ZSM-5 framework by combination of high resolution  $^{27}\text{Al}$  NMR and DFT/MM calculations," *Phys. Chem. Chem. Phys.*, 11 (2009) 1237-1247.
- [99] M. Ravi, V.L. Sushkevich, J.A. van Bokhoven, "Towards a better understanding of Lewis acidic aluminium in zeolites," *Nat. Mater.*, 19 (2020) 1047-1056.
- [100] C.J.A. Mota, D.L. Bhering, N. Rosenbach, "A DFT Study of the Acidity of Ultrastable Y Zeolite: Where is the Brønsted/Lewis Acid Synergism?," *Angew. Chem. Int. Ed.*, 43 (2004) 3050-3053.
- [101] M. Müller, G. Harvey, R. Prins, "Comparison of the Dealumination of Zeolites Beta, Mordenite, ZSM-5 and Ferrierite by Thermal Treatment, Leaching with Oxalic Acid and Treatment with  $\text{SiCl}_4$  by  $^1\text{H}$ ,  $^{29}\text{Si}$  and  $^{27}\text{Al}$  MAS NMR," *Microporous Mesoporous Mater.*, 34 (2000) 135-147.
- [102] J.A. van Bokhoven, D.C. Koningsberger, P. Kunkeler, H. Van Bekkum, A.P.M. Kentgens, "Stepwise Dealumination of Zeolite Beta at Specific T-sites Observed with  $^{27}\text{Al}$  MAS and  $^{27}\text{Al}$  MQ MAS NMR," *J. Am. Chem. Soc.*, 122 (2000) 12842-12847.
- [103] M.-C. Silaghi, C. Chizallet, J. Sauer, P. Raybaud, "Dealumination Mechanisms of Zeolites and Extra-framework Aluminum Confinement," *J. Catal.*, 339 (2016) 242-255.
- [104] L. Karwacki, D.A.M. de Winter, L.R. Aramburo, M.N. Lebbink, J.A. Post, M.R. Drury, B.M. Weckhuysen, "Architecture-Dependent Distribution of Mesopores in

Steamed Zeolite Crystals as Visualized by FIB-SEM Tomography," *Angew. Chem. Int. Ed.*, 50 (2011) 1294-1298.

[105] M. Abdolrahmani, K. Chen, J.L. White, "Assessment, Control, and Impact of Brønsted Acid Site Heterogeneity in Zeolite HZSM-5," *J. Phys. Chem. C*, 122 (2018) 15520-15528.

[106] A. Zheng, S.B. Liu, F. Deng, "<sup>31</sup>P NMR Chemical Shifts of Phosphorus Probes as Reliable and Practical Acidity Scales for Solid and Liquid Catalysts," *Chem. Rev.*, 117 (2017) 12475-12531.

[107] Z. Zhao, S. Xu, M.Y. Hu, X. Bao, C.H.F.F. Peden, J. Hu, "Investigation of Aluminum Site Changes of Dehydrated Zeolite H-Beta during a Rehydration Process by High-Field Solid-State NMR," *J. Phys. Chem. C*, 119 (2015) 1410-1417.

[108] J.P. Gilson, G.C. Edwards, A.W. Peters, K. Rajagopalan, R.F. Wormsbecher, T.G. Roberie, M.P. Shatlock, "Penta-co-ordinated Aluminium in Zeolites and Aluminosilicates," *Journal of the Chemical Society, Chemical Communications*, (1987) 91-92.

[109] C. Mirodatos, D. Barthomeuf, "Superacid Sites in Zeolites," *Journal of the Chemical Society, Chemical Communications*, (1981) 39-40.

[110] J.A. van Bokhoven, B.A. Williams, W. Ji, D.C. Koningsberger, H.H. Kung, J.T. Miller, "Observation of a Compensation Relation for Monomolecular Alkane Cracking by Zeolites: the Dominant Role of Reactant Sorption," *J. Catal.*, 224 (2004) 50-59.

- [111] A.J. Jones, R.T. Carr, S.I. Zones, E. Iglesia, "Acid Strength and Solvation in Catalysis by MFI Zeolites and Effects of the Identity, Concentration and Location of Framework Heteroatoms," *J. Catal.*, 312 (2014) 58.
- [112] N. Xue, A. Vjunov, S. Schallmoser, J.L. Fulton, M. Sanchez-Sanchez, J.Z. Hu, D. Mei, J.A. Lercher, "Hydrolysis of Zeolite Framework Aluminum and Its Impact on Acid Catalyzed Alkane Reactions," *J. Catal.*, 365 (2018) 359-366.
- [113] Z. Wang, L.A. O'Dell, X. Zeng, C. Liu, S. Zhao, W. Zhang, M. Gaborieau, Y. Jiang, J. Huang, "Insight into Three-Coordinate Aluminum Species on Ethanol-to-Olefin Conversion over ZSM-5 Zeolites," *Angewandte Chemie International Edition*, 58 (2019) 18061-18068.
- [114] S. Müller, Y. Liu, F.M. Kirchberger, M. Tonigold, M. Sanchez-Sanchez, J.A. Lercher, "Hydrogen Transfer Pathways during Zeolite Catalyzed Methanol Conversion to Hydrocarbons," *J. Am. Chem. Soc.*, 138 (2016) 15994-16003.
- [115] I. Yarulina, A.D. Chowdhury, F. Meirer, B.M. Weckhuysen, J. Gascon, "Recent Trends and Fundamental Insights in the Methanol-to-Hydrocarbons Process," *Nat. Catal.*, 1 (2018) 398-411.
- [116] C. Wang, Y. Chu, J. Xu, Q. Wang, G. Qi, P. Gao, X. Zhou, F. Deng, "Extra-Framework Aluminum-Assisted Initial C–C Bond Formation in Methanol-to-Olefins Conversion on Zeolite H-ZSM-5," *Angew. Chem. Int. Ed.*, 57 (2018) 10197-10201.
- [117] Y. Chu, X. Yi, C. Li, X. Sun, A. Zheng, "Brønsted/Lewis Acid Sites Synergistically Promote the Initial C-C Bond Formation in the MTO Reaction," *Chem. Sci.*, 9 (2018) 6470-6479.

- [118] R. Althoff, B. Schulz-Dobrick, F. Schüth, K. Unger, "Controlling the Spatial-Distribution of Aluminum in ZSM-5 Crystals," *Microporous Mater.*, 1 (1993) 207.
- [119] K.j. Chao, J.y. Chern, "Aluminium Distribution in Large ZSM-5 Crystals," *Zeolites*, 8 (1988) 82-85.
- [120] G. Garralón, V. Fornés, A. Corma, "Faujasites Dealuminated with Ammonium Hexafluorosilicate: Variables Affecting the Method of Preparation," *Zeolites*, 8 (1988) 268-272.
- [121] R. von Ballmoos, W.M. Meier, "Zoned Aluminium Distribution in Synthetic Zeolite ZSM-5," *Nature*, 289 (1981) 782-783.
- [122] K. Ding, A. Corma, J.A. Maciá-Agulló, J.G. Hu, S. Krämer, P.C. Stair, G.D. Stucky, "Constructing Hierarchical Porous Zeolites via Kinetic Regulation," *J. Am. Chem. Soc.*, 137 (2015) 11238-11241.
- [123] C.S. Cundy, M.S. Henty, R.J. Plaisted, "Investigation of Na,TPA-ZSM-5 zeolite synthesis by chemical methods," *Zeolites*, 15 (1995) 342-352.
- [124] L.R. Aramburo, Y. Liu, T. Tyliczszak, F.M.F. de Groot, J.C. Andrews, B.M. Weckhuysen, "3D Nanoscale Chemical Imaging of the Distribution of Aluminum Coordination Environments in Zeolites with Soft X-Ray Microscopy," *ChemPhysChem*, 14 (2013) 496-499.
- [125] J.E. Schmidt, J.D. Poplawsky, B. Mazumder, O. Attila, D. Fu, D.A. de Winter, F. Meirer, S.R. Bare, B.M. Weckhuysen, "Coke formation in a zeolite crystal during the methanol-to-hydrocarbons reaction as studied with atom probe tomography," *Angew. Chem. Int. Ed.*, 55 (2016) 11173-11177.

- [126] T. Kunieda, J.H. Kim, M. Niwa, "Source of selectivity of p-xylene formation in the toluene disproportionation over HZSM-5 zeolites," *J. Catal.*, 188 (1999) 431-433.
- [127] W. Qin, Y. Zhou, J.D. Rimer, "Deleterious effects of non-framework Al species on the catalytic performance of ZSM-5 crystals synthesized at low temperature," *React. Chem. Eng.*, 4 (2019) 1957-1968.
- [128] M. Henry, M. Bulut, W. Vermandel, B. Sels, P. Jacobs, D. Minoux, N. Nesterenko, J.P. Dath, "Low Temperature Conversion of Linear C<sub>4</sub> Olefins Using Acid ZSM-5 Zeolites with Aluminum Concentration Gradient," *Appl. Catal., A*, 437-438 (2012) 96-103.
- [129] A.A. Rownaghi, F. Rezaei, M. Stante, J. Hedlund, "Selective Dehydration of Methanol to Dimethyl Ether on ZSM-5 Nanocrystals," *Appl. Catal., B*, 119 (2012) 56-61.
- [130] D. Mores, E. Stavitski, S.P. Verkleij, A. Lombard, A. Cabiac, L. Rouleau, J. Patarin, A. Simon-Masseron, B.M. Weckhuysen, "Core-shell H-ZSM-5/Silicalite-1 composites: Brønsted acidity and catalyst deactivation at the individual particle level," *Phys. Chem. Chem. Phys.*, 13 (2011) 15985.
- [131] C. Wang, L. Zhang, X. Huang, Y. Zhu, G. Li, Q. Gu, J. Chen, L. Ma, X. Li, Q. He, J. Xu, Q. Sun, C. Song, M. Peng, J. Sun, D. Ma, "Maximizing sinusoidal channels of HZSM-5 for high shape-selectivity to p-xylene," *Nat. Commun.*, 10 (2019) 1-8.
- [132] N. Masoumifard, R. Guillet-Nicolas, F. Kleitz, "Synthesis of Engineered Zeolitic Materials: From Classical Zeolites to Hierarchical Core-Shell Materials," *Adv. Mater.*, 30 (2018) 1704439-1704439.

- [133] A.M. Goossens, B.H. Wouters, V. Buschmann, J.A. Martens, "Oriented FAU Zeolite Films on Micrometer-Sized EMT Crystals," *Adv. Mater.*, 11 (1999) 561-564.
- [134] Y. Bouizi, L. Rouleau, V.P. Valtchev, "Factors Controlling the Formation of Core-Shell Zeolite-Zeolite Composites," *Chem. Mater.*, 18 (2006) 4959-4966.
- [135] Q. Li, Z. Wang, J. Hedlund, D. Creaser, H. Zhang, X. Zou, A.-J. Bons, "Synthesis and Characterization of Colloidal Zoned MFI Crystals," *Microporous Mesoporous Mater.*, (2004).
- [136] F. Goodarzi, I.P. Herrero, G.N. Kalantzopoulos, S. Svelle, A. Lazzarini, P. Beato, U. Olsbye, S. Kegnæs, "Synthesis of Mesoporous ZSM-5 Zeolite Encapsulated in an Ultrathin Protective Shell of Silicalite-1 for MTH Conversion," *Microporous Mesoporous Mater.*, 292 (2020) 109730-109730.
- [137] C. Peng, Z. Liu, Y. Yonezawa, Y. Yanaba, N. Katada, I. Murayama, S. Segoshi, T. Okubo, T. Wakihara, "Ultrafast Post-Synthesis Treatment to Prepare ZSM-5@Silicalite-1 as a Core-Shell Structured Zeolite Catalyst," *Microporous Mesoporous Mater.*, 277 (2019) 197-202.
- [138] U. Olsbye, S. Svelle, M. Bjørgen, P. Beato, T.V.W. Janssens, F. Joensen, S. Bordiga, K.P. Lillerud, "Conversion of Methanol to Hydrocarbons: How Zeolite Cavity and Pore Size Controls Product Selectivity," *Angew. Chem. Int. Ed.*, 51 (2012) 5810-5831.
- [139] A. Galadima, O. Muraza, "From synthesis gas production to methanol synthesis and potential upgrade to gasoline range hydrocarbons: A review," *Journal of Natural Gas Science and Engineering*, 25 (2015) 303-316.

- [140] A.D. Chowdhury, K. Houben, G.T. Whiting, M. Mokhtar, A.M. Asiri, S.A. Al-Thabaiti, S.N. Basahel, M. Baldus, B.M. Weckhuysen, "Initial Carbon-Carbon Bond Formation during the Early Stages of the Methanol-to-Olefin Process Proven by Zeolite-Trapped Acetate and Methyl Acetate," *Angew. Chem. Int. Ed.*, 55 (2016) 15840-15845.
- [141] Y. Liu, S. Müller, D. Berger, J. Jelic, K. Reuter, M. Tonigold, M. Sanchez-Sanchez, J.A. Lercher, "Formation Mechanism of the First Carbon–Carbon Bond and the First Olefin in the Methanol Conversion into Hydrocarbons," *Angew. Chem. Int. Ed.*, 55 (2016) 5723-5726.
- [142] S. Ilias, A. Bhan, "Mechanism of the Catalytic Conversion of Methanol to Hydrocarbons," *ACS Catal.*, 3 (2013) 18-31.
- [143] S. Ilias, R. Khare, A. Malek, A. Bhan, "A descriptor for the relative propagation of the aromatic- and olefin-based cycles in methanol-to-hydrocarbons conversion on H-ZSM-5," *J. Catal.*, 303 (2013) 135-140.
- [144] S.S. Arora, A. Bhan, "The critical role of methanol pressure in controlling its transfer dehydrogenation and the corresponding effect on propylene-to-ethylene ratio during methanol-to-hydrocarbons catalysis on H-ZSM-5," *J. Catal.*, 356 (2017) 300-306.
- [145] Y. Liu, F.M. Kirchberger, S. Müller, M. Eder, M. Tonigold, M. Sanchez-Sanchez, J.A. Lercher, "Critical role of formaldehyde during methanol conversion to hydrocarbons," *Nat. Commun.*, 10 (2019) 1462.

- [146] B.L. Foley, B.A. Johnson, A. Bhan, "A Method for Assessing Catalyst Deactivation: A Case Study on Methanol-to-Hydrocarbons Conversion," *ACS Catal.*, 9 (2019) 7065-7072.
- [147] M. Guisnet, L. Costa, F.R. Ribeiro, "Prevention of zeolite deactivation by coking," *Journal of Molecular Catalysis A: Chemical*, 305 (2009) 69-83.
- [148] R. Khare, D. Millar, A. Bhan, "A mechanistic basis for the effects of crystallite size on light olefin selectivity in methanol-to-hydrocarbons conversion on MFI," *J. Catal.*, 321 (2015) 23-31.
- [149] Zeolite Market Size Worth \$33.80 Billion By 2022 | Growth Rate: 2.5%, in.
- [150] G. Harvey, L.S. Dent Glasser, Structure and Properties of Aluminosilicate Solutions and Gels, in: *Zeolite Synthesis*, American Chemical Society, 1989, pp. 49-65.
- [151] M. Kumar, M.K. Choudhary, J.D. Rimer, "Transient modes of zeolite surface growth from 3D gel-like islands to 2D single layers," *Nat. Commun.*, 9 (2018) 2129.
- [152] F. Schüth, "Nucleation and crystallization of solids from solution," *Current Opinion in Solid State and Materials Science*, 5 (2001) 389-395.
- [153] M. Smaïhi, O. Barida, V. Valtchev, "Investigation of the Crystallization Stages of LTA-Type Zeolite by Complementary Characterization Techniques," *European Journal of Inorganic Chemistry*, 2003 (2003) 4370-4377.
- [154] E.A. Eilertsen, M. Haouas, A.B. Pinar, N.D. Hould, R.F. Lobo, K.P. Lillerud, F. Taulelle, "NMR and SAXS Analysis of Connectivity of Aluminum and Silicon Atoms in the Clear Sol Precursor of SSZ-13 Zeolite," *Chem. Mater.*, 24 (2012) 571-578.

- [155] G. Melinte, V. Georgieva, M.-A. Springuel-Huet, A. Nossov, O. Ersen, F. Guenneau, A. Gedeon, A. Palčić, K.N. Bozhilov, C. Pham-Huu, S. Qiu, S. Mintova, V. Valtchev, "3D Study of the Morphology and Dynamics of Zeolite Nucleation," *Chem. Eur. J.*, 21 (2015) 18316-18327.
- [156] S. Mintova, N.H. Olson, V. Valtchev, T. Bein, "Mechanism of Zeolite A Nanocrystal Growth from Colloids at Room Temperature," *Science*, 283 (1999) 958.
- [157] R. Aiello, F. Crea, A. Nastro, B. Subotić, F. Testa, "Influence of cations on the physicochemical and structural properties of aluminosilicate gel precursors. Part 1. Chemical and thermal properties," *Zeolites*, 11 (1991) 767-775.
- [158] V. Valtchev, S. Rigoleto, K.N. Bozhilov, "Gel evolution in a FAU-type zeolite yielding system at 90°C," *Microporous Mesoporous Mater.*, 101 (2007) 73-82.
- [159] D.P. Petry, M. Haouas, S.C.C. Wong, A. Aerts, C.E.A. Kirschhock, J.A. Martens, S.J. Gaskell, M.W. Anderson, F. Taulelle, "Connectivity Analysis of the Clear Sol Precursor of Silicalite: Are Nanoparticles Aggregated Oligomers or Silica Particles?," *J. Phys. Chem. C*, 113 (2009) 20827-20836.
- [160] L. Ren, C. Li, F. Fan, Q. Guo, D. Liang, Z. Feng, C. Li, S. Li, F.-S. Xiao, "UV-Raman and NMR Spectroscopic Studies on the Crystallization of Zeolite A and a New Synthetic Route," *Chem. Eur. J.*, 17 (2011) 6162-6169.
- [161] P. Cubillas, S.M. Stevens, N. Blake, A. Umemura, C.B. Chong, O. Terasaki, M.W. Anderson, "AFM and HRSEM Investigation of Zeolite A Crystal Growth. Part 1: In the Absence of Organic Additives," *J. Phys. Chem. C*, 115 (2011) 12567-12574.

- [162] B. Slater, T. Ohsuna, Z. Liu, O. Terasaki, "Insights into the crystal growth mechanisms of zeolites from combined experimental imaging and theoretical studies," *Faraday Discussions*, 136 (2007) 125-141.
- [163] W.H. Dokter, H.F. van Garderen, T.P.M. Beelen, R.A. van Santen, W. Bras, "Homogeneous versus Heterogeneous Zeolite Nucleation," *Angewandte Chemie International Edition in English*, 34 (1995) 73-75.
- [164] F.K. Crundwell, "The dissolution and leaching of minerals: Mechanisms, myths and misunderstandings," *Hydrometallurgy*, 139 (2013) 132-148.
- [165] F.K. Crundwell, "The mechanism of dissolution of minerals in acidic and alkaline solutions: Part I — A new theory of non-oxidation dissolution," *Hydrometallurgy*, 149 (2014) 252-264.
- [166] F.K. Crundwell, "On the Mechanism of the Dissolution of Quartz and Silica in Aqueous Solutions," *ACS Omega*, 2 (2017) 1116-1127.
- [167] F.K. Crundwell, "The mechanism of dissolution of minerals in acidic and alkaline solutions: Part II Application of a new theory to silicates, aluminosilicates and quartz," *Hydrometallurgy*, 149 (2014) 265-275.
- [168] M. Milina, S. Mitchell, P. Crivelli, D. Cooke, J. Pérez-Ramírez, "Mesopore quality determines the lifetime of hierarchically structured zeolite catalysts," *Nat. Commun.*, 5 (2014) 3922.
- [169] Z. Qin, J.-P. Gilson, V. Valtchev, "Mesoporous zeolites by fluoride etching," *Current Opinion in Chemical Engineering*, 8 (2015) 1-6.

- [170] N. Linares, F.G. Cirujano, D.E. De Vos, J. García-Martínez, "Surfactant-templated zeolites for the production of active pharmaceutical intermediates," *Chem. Commun.*, 55 (2019) 12869-12872.
- [171] S. van Donk, A.H. Janssen, J.H. Bitter, K.P. de Jong, "Generation, Characterization, and Impact of Mesopores in Zeolite Catalysts," *Catal. Rev.*, 45 (2003) 297-319.
- [172] S.M.T. Almutairi, B. Mezari, E.A. Pidko, P.C.M.M. Magusin, E.J.M. Hensen, "Influence of steaming on the acidity and the methanol conversion reaction of HZSM-5 zeolite," *J. Catal.*, 307 (2013) 194-203.
- [173] R.M. Barrer, M.B. Makki, "MOLECULAR SIEVE SORBENTS FROM CLINOPTILOLITE," *Canadian Journal of Chemistry*, 42 (1964) 1481-1487.
- [174] M. Tromp, J.A. van Bokhoven, M.T. Garriga Oostenbrink, J.H. Bitter, K.P. de Jong, D.C. Koningsberger, "Influence of the Generation of Mesopores on the Hydroisomerization Activity and Selectivity of n-Hexane over Pt/Mordenite," *J. Catal.*, 190 (2000) 209-214.
- [175] M. Ogura, S.-y. Shinomiya, J. Tateno, Y. Nara, M. Nomura, E. Kikuchi, M. Matsukata, "Alkali-treatment technique — new method for modification of structural and acid-catalytic properties of ZSM-5 zeolites," *Appl. Catal., A*, 219 (2001) 33-43.
- [176] M.K. Wardani, G.T.M. Kadja, A.T.N. Fajar, Subagjo, I.G.B.N. Makertihartha, M.L. Gunawan, V. Suendo, R.R. Mukti, "Highly crystalline mesoporous SSZ-13 zeolite obtained via controlled post-synthetic treatment," *RSC Adv.*, 9 (2019) 77-86.

- [177] Z. Qin, G. Melinte, J.P. Gilson, M. Jaber, K. Bozhilov, P. Boullay, S. Mintova, O. Ersen, V. Valtchev, "The Mosaic Structure of Zeolite Crystals," *Angew. Chem. Int. Ed.*, 55 (2016) 15049-15052.
- [178] Z. Qin, L. Pinard, M.A. Benghalem, T.J. Daou, G. Melinte, O. Ersen, S. Asahina, J.-P. Gilson, V. Valtchev, "Preparation of Single-Crystal "House-of-Cards"-like ZSM-5 and Their Performance in Ethanol-to-Hydrocarbon Conversion," *Chem. Mater.*, 31 (2019) 4639-4648.
- [179] T.M. Davis, T.O. Drews, H. Ramanan, C. He, J. Dong, H. Schnablegger, M.A. Katsoulakis, E. Kokkoli, A.V. McCormick, R.L. Penn, M. Tsapatsis, "Mechanistic principles of nanoparticle evolution to zeolite crystals," *Nat. Mater.*, 5 (2006) 400-408.
- [180] J.J. De Yoreo, P.U.P.A. Gilbert, N.A.J.M. Sommerdijk, R.L. Penn, S. Whitlam, D. Joester, H. Zhang, J.D. Rimer, A. Navrotsky, J.F. Banfield, A.F. Wallace, F.M. Michel, F.C. Meldrum, H. Cölfen, P.M. Dove, "Crystallization by particle attachment in synthetic, biogenic, and geologic environments," *Science*, 349 (2015).
- [181] J.R. Agger, N. Hanif, C.S. Cundy, A.P. Wade, S. Dennison, P.A. Rawlinson, M.W. Anderson, "Silicalite Crystal Growth Investigated by Atomic Force Microscopy," *J. Am. Chem. Soc.*, 125 (2003) 830-839.
- [182] C.G. Darwin, "XCII. The reflexion of X-rays from imperfect crystals," *The London, Edinburgh, and Dublin Philosophical Magazine and Journal of Science*, 43 (1922) 800-829.

- [183] K. Na, M. Choi, W. Park, Y. Sakamoto, O. Terasaki, R. Ryoo, "Pillared MFI zeolite nanosheets of a single-unit-cell thickness," *J. Am. Chem. Soc.*, 132 (2010) 4169-4177.
- [184] R. Althoff, B. Schulz-Dobrick, F. Schüth, K. Unger, "Controlling the spatial distribution of aluminum in ZSM-5 crystals," *Microporous Mater.*, 1 (1993) 207-218.
- [185] R. Zoran, H.J. P., D. Upakul, S.T. U., R. Marcus, B.A. M., W.B. M., "Intergrowth structure and aluminium zoning of a zeolite ZSM-5 crystal as resolved by synchrotron-based micro x-ray diffraction imaging," *Angew. Chem. Int. Ed.*, 52 (2013) 13382-13386.
- [186] L.R. Aramburo, K. Lukasz, C. Pablo, A. Shunsuke, d.W.D.A. Matthijs, D.M. R., B.I.L. C., S. Eli, M. Davide, D. Marco, B. Philippe, D. Paul, T.S. Frédéric, P.J. A., A.M. W., T. Osamu, W.B. M., "The porosity, acidity, and reactivity of dealuminated zeolite ZSM-5 at the single particle level: The influence of the zeolite architecture," *Chem. Eur. J.*, 17 (2011) 13773-13781.
- [187] K. Kim, R. Ryoo, H.-D. Jang, M. Choi, "Spatial distribution, strength, and dealumination behavior of acid sites in nanocrystalline MFI zeolites and their catalytic consequences," *J. Catal.*, 288 (2012) 115-123.
- [188] D.J. Yang, Process for coating crystalline silica polymorphs, in, EI Du Pont de Nemours and Co, 1982.
- [189] P.G. Rodewald, Silica-modified zeolite catalysts, in, Mobil Oil Corporation, New York. N.Y., 1981.

- [190] J.H. Kim, A. Ishida, M. Okajima, M. Niwa, "Modification of HZSM-5 by CVD of various silicon compounds and generation of para-selectivity," *J. Catal.*, 161 (1996) 387-392.
- [191] S. Zheng, H.R. Heydenrych, A. Jentys, J.A. Lercher, "Influence of surface modification on the acid site distribution of HZSM-5," *J. Phys. Chem. B*, 106 (2002) 9552-9558.
- [192] J. Jae, G.A. Tompsett, A.J. Foster, K.D. Hammond, S.M. Auerbach, R.F. Lobo, G.W. Huber, "Investigation into the shape selectivity of zeolite catalysts for biomass conversion," *J. Catal.*, 279 (2011) 257.
- [193] T. Ennaert, J. Van Aelst, J. Dijkmans, R. De Clercq, W. Schutyser, M. Dusselier, D. Verboekend, B.F. Sels, "Potential and challenges of zeolite chemistry in the catalytic conversion of biomass," *Chem. Soc. Rev.*, 45 (2016) 584.
- [194] S. Zheng, H.R. Heydenrych, H.P. Röger, A. Jentys, J.A. Lercher, "On the enhanced selectivity of HZSM-5 modified by chemical liquid deposition," *Top. Catal.*, 22 (2003) 101-106.
- [195] C. Yu-Ting, W. Zhuopeng, G.C. J., F. Wei, H.G. W., "Production of p-xylene from biomass by catalytic fast pyrolysis using ZSM-5 catalysts with reduced pore openings," *Angew. Chem. Int. Ed.*, 51 (2012) 11097-11100.
- [196] A.J. Foster, J. Jae, Y.-T. Cheng, G.W. Huber, R.F. Lobo, "Optimizing the aromatic yield and distribution from catalytic fast pyrolysis of biomass over ZSM-5," *Appl. Catal., A*, 423-424 (2012) 154-161.

- [197] Z. Yan, D. Ma, J. Zhuang, X. Liu, X. Liu, X. Han, X. Bao, F. Chang, L. Xu, Z. Liu, "On the acid-dealumination of USY zeolite: a solid state NMR investigation," *J. Mol. Catal. A: Chem.*, 194 (2003) 153-167.
- [198] T.T. Le, A. Chawla, J.D. Rimer, "Impact of acid site speciation and spatial gradients on zeolite catalysis," *J. Catal.*, 391 (2020) 56-68.
- [199] Y.-Q. Deng, S.-F. Yin, C.-T. Au, "Preparation of nanosized Silicalite-1 and its application in vapor-phase Beckmann rearrangement of cyclohexanone oxime," *Ind. Eng. Chem. Res.*, 51 (2012) 9492-9499.
- [200] G. Paul, C. Bisio, I. Braschi, M. Cossi, G. Gatti, E. Gianotti, L. Marchese, "Combined solid-state NMR, FT-IR and computational studies on layered and porous materials," *Chem. Soc. Rev.*, 47 (2018) 5684-5739.
- [201] E. Borodina, F. Meirer, I. Lezcano-González, M. Mokhtar, A.M. Asiri, S.A. Al-Thabaiti, S.N. Basahel, J. Ruiz-Martinez, B.M. Weckhuysen, "Influence of the reaction temperature on the nature of the active and deactivating species during methanol to olefins conversion over H-SSZ-13," *ACS Catal.*, 5 (2015) 992-1003.
- [202] F.Y. Dai, M. Suzuki, H. Takahashi, I. Saito, Mechanism of zeolite crystallization without using template reagents of organic bases, in: Y. Murakami, A. Iijima, J.W. Ward (Eds.) *Stud. Surf. Sci. Catal.*, Elsevier, 1986, pp. 223-230.
- [203] A. Chawla, R. Li, R. Jain, R.J. Clark, J.G. Sutjianto, J.C. Palmer, J.D. Rimer, "Cooperative effects of inorganic and organic structure-directing agents in ZSM-5 crystallization," *Molecular Systems Design & Engineering*, 3 (2018) 159-170.

- [204] L. Meng, X. Zhu, W. Wannapakdee, R. Pestman, M.G. Goesten, L. Gao, A.J.F. van Hoof, E.J.M. Hensen, "A dual-templating synthesis strategy to hierarchical ZSM-5 zeolites as efficient catalysts for the methanol-to-hydrocarbons reaction," *J. Catal.*, 361 (2018) 135-142.
- [205] L. Karwacki, M.H.F. Kox, D.A. Matthijs De Winter, M.R. Drury, J.D. Meeldijk, E. Stavitski, W. Schmidt, M. Mertens, P. Cubillas, N. John, A. Chan, N. Kahn, S.R. Bare, M. Anderson, J. Kornatowski, B.M. Weckhuysen, "Morphology-dependent zeolite intergrowth structures leading to distinct internal and outer-surface molecular diffusion barriers," *Nat. Mater.*, 8 (2009) 959-965.
- [206] C.L. Cavalcante, Jr., D.M. Ruthven, "Adsorption of branched and cyclic paraffins in Silicalite. 2. Kinetics," *Ind. Eng. Chem. Res.*, 34 (1995) 185-191.
- [207] I. Yarulina, K. De Wispelaere, S. Bailleul, J. Goetze, M. Radersma, E. Abou-Hamad, I. Vollmer, M. Goesten, B. Mezari, E.J.M. Hensen, J.S. Martínez-Espín, M. Morten, S. Mitchell, J. Perez-Ramirez, U. Olsbye, B.M. Weckhuysen, V. Van Speybroeck, F. Kapteijn, J. Gascon, "Structure–performance descriptors and the role of Lewis acidity in the methanol-to-propylene process," *Nat. Chem.*, 10 (2018) 804-812.
- [208] J. Goetze, F. Meirer, I. Yarulina, J. Gascon, F. Kapteijn, J. Ruiz-Martínez, B.M. Weckhuysen, "Insights into the activity and deactivation of the methanol-to-olefins process over different small-pore zeolites as studied with operando uv–vis spectroscopy," *ACS Catal.*, (2017) 4033-4046.

- [209] K. Barbera, F. Bonino, S. Bordiga, T.V.W. Janssens, P. Beato, "Structure–deactivation relationship for ZSM-5 catalysts governed by framework defects," *J. Catal.*, 280 (2011) 196-205.
- [210] Z. Qin, L. Lakiss, L. Tosheva, J.-P. Gilson, A. Vicente, C. Fernandez, V. Valtchev, "Comparative study of nano-ZSM-5 catalysts synthesized in OH<sup>-</sup> and F<sup>-</sup> media," *Adv. Funct. Mater.*, 24 (2014) 257-264.
- [211] Z. Li, J. Martínez-Triguero, P. Concepción, J. Yu, A. Corma, "Methanol to olefins: activity and stability of nanosized SAPO-34 molecular sieves and control of selectivity by silicon distribution," *Phys. Chem. Chem. Phys.*, 15 (2013) 14670-14680.
- [212] S. Lee, M. Choi, "Unveiling coke formation mechanism in MFI zeolites during methanol-to-hydrocarbons conversion," *J. Catal.*, 375 (2019) 183-192.
- [213] R. Brent, S.M. Stevens, O. Terasaki, M.W. Anderson, "Coaxial core shell overgrowth of zeolite L - Dependence on original crystal growth mechanism," *Cryst. Growth Des.*, 10 (2010) 5182-5186.
- [214] W. Huybrechts, J.W. Thybaut, B.R. De Waele, G. Vanbutsele, K.J. Houthoofd, F. Bertinchamps, J.F.M. Denayer, E.M. Gaigneaux, G.B. Marin, G.V. Baron, P.A. Jacobs, J.A. Martens, "Bifunctional catalytic isomerization of decane over MTT-type aluminosilicate zeolite crystals with siliceous rim," *Journal of Catalysis*, 239 (2006) 451-459.
- [215] M. Okamoto, L. Huang, M. Yamano, S. Sawayama, Y. Nishimura, "Skeletal isomerization of tetradecane catalyzed by TON-type zeolites with a fragmented core-shell structure," *Appl. Catal., A*, 455 (2013) 122-128.

- [216] J.H. Ahn, R. Kolvenbach, S.S. Al-Khattaf, A. Jentys, J.A. Lercher, "Enhancing shape selectivity without loss of activity - novel mesostructured ZSM5 catalysts for methylation of toluene to p-xylene," *Chem. Commun.*, 49 (2013) 10584-10586.
- [217] T. Hibino, M. Niwa, Y. Murakami, "Shape-selectivity over hzsm-5 modified by chemical vapor deposition of silicon alkoxide," *J. Catal.*, 128 (1991) 551-558.
- [218] S. Zheng, H.R. Heydenrych, H.P. Roger, A. Jentys, J.A. Lercher, "On the Enhanced Selectivity of HZSM-5 Modified by Chemical Liquid Deposition," *Top. Catal.*, 22 (2003) 101.
- [219] Y. Shen, T.T. Le, R. Li, J.D. Rimer, "Optimized Synthesis of ZSM-11 Catalysts using 1,8-Diaminooctane as a Structure-Directing Agent," *ChemPhysChem*, 19 (2018) 529-537.
- [220] F. Bleken, W. Skistad, K. Barbera, M. Kustova, S. Bordiga, P. Beato, K.P. Lillerud, S. Svelle, U. Olsbye, "Conversion of methanol over 10-ring zeolites with differing volumes at channel intersections: comparison of TNU-9, IM-5, ZSM-11 and ZSM-5," *Phys. Chem. Chem. Phys.*, 13 (2011) 2539-2549.
- [221] T.V.W. Janssens, "A new approach to the modeling of deactivation in the conversion of methanol on zeolite catalysts," *J. Catal.*, 264 (2009) 130-137.
- [222] J.S. Martinez-Espin, M. Morten, T.V.W. Janssens, S. Svelle, P. Beato, U. Olsbye, "New insights into catalyst deactivation and product distribution of zeolites in the methanol-to-hydrocarbons (MTH) reaction with methanol and dimethyl ether feeds," *Catal. Sci. Technol.*, (2017).

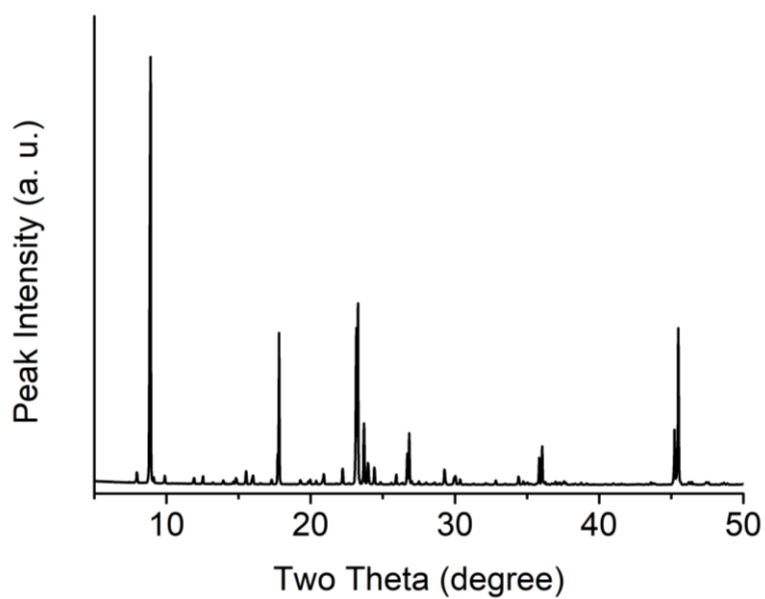
- [223] M. Miyamoto, K. Mabuchi, J. Kamada, Y. Hirota, Y. Oumi, N. Nishiyama, S. Uemiya, "para-Selectivity of silicalite-1 coated MFI type galloaluminosilicate in aromatization of light alkanes," *Journal of Porous Materials*, 22 (2015) 769-778.
- [224] A. Bhan, W. Nicholas Delgass, "Propane Aromatization over HZSM-5 and Ga/HZSM-5 Catalysts," *Catal. Rev.*, 50 (2008) 19-151.
- [225] M.H. Mahyuddin, A. Staykov, Y. Shiota, K. Yoshizawa, "Direct Conversion of Methane to Methanol by Metal-Exchanged ZSM-5 Zeolite (Metal = Fe, Co, Ni, Cu)," *ACS Catal.*, 6 (2016) 8321-8331.
- [226] V. Valtchev, G. Majano, S. Mintova, J. Perez-Ramirez, "Tailored crystalline microporous materials by post-synthesis modification," *Chemical Society Reviews*, 42 (2013) 263-290.
- [227] M.C. Silaghi, C. Chizallet, P. Raybaud, "Challenges on Molecular Aspects of Dealumination and Desilication of Zeolites," *Microporous Mesoporous Mater.*, 191 (2014) 82-96.
- [228] J.D. Kistler, N. Chotigkrai, P. Xu, B. Enderle, P. Praserthdam, C.-Y. Chen, N.D. Browning, B.C. Gates, "A Single-Site Platinum CO Oxidation Catalyst in Zeolite KLTL: Microscopic and Spectroscopic Determination of the Locations of the Platinum Atoms," *Angewandte Chemie International Edition*, 53 (2014) 8904-8907.
- [229] M. Choi, Z. Wu, E. Iglesia, "Mercaptosilane-Assisted Synthesis of Metal Clusters within Zeolites and Catalytic Consequences of Encapsulation," *Journal of the American Chemical Society*, 132 (2010) 9129-9137.

- [230] T. Otto, S.I. Zones, Y. Hong, E. Iglesia, "Synthesis of highly dispersed cobalt oxide clusters encapsulated within LTA zeolites," *J. Catal.*, 356 (2017) 173-185.
- [231] R.S. Ghosh, T.T. Le, T. Terlier, J.D. Rimer, M.P. Harold, D. Wang, "Enhanced Selective Oxidation of Ammonia in a Pt/Al<sub>2</sub>O<sub>3</sub>@Cu/ZSM-5 Core–Shell Catalyst," *ACS Catal.*, 10 (2020) 3604-3617.
- [232] M.F. Hsieh, Y.W. Zhou, H. Thirumalai, L.C. Grabow, J.D. Rimer, "Silver-Promoted Dehydroaromatization of Ethylene over ZSM-5 Catalysts," *ChemCatChem*, 9 (2017) 1675-1682.
- [233] J. Zhang, W. Qian, C. Kong, F. Wei, "Increasing Para-Xylene Selectivity in Making Aromatics from Methanol with a Surface-Modified Zn/P/ZSM-5 Catalyst," *ACS Catal.*, 5 (2015) 2982-2988.
- [234] P. Bollini, A. Bhan, "Improving HSAPO-34 Methanol-to-Olefin Turnover Capacity by Seeding the Hydrocarbon Pool," *ChemPhysChem*, 19 (2017) 479-483.
- [235] A. Hwang, A. Bhan, "Bifunctional Strategy Coupling Y<sub>2</sub>O<sub>3</sub>-Catalyzed Alkanal Decomposition with Methanol-to-Olefins Catalysis for Enhanced Lifetime," *ACS Catal.*, 7 (2017) 4417-4422.
- [236] K. Cheng, L.I. van der Wal, H. Yoshida, J. Oenema, J. Harmel, Z. Zhang, G. Sunley, J. Zečević, K.P. de Jong, "Impact of the Spatial Organization of Bifunctional Metal–Zeolite Catalysts on the Hydroisomerization of Light Alkanes," *Angew. Chem. Int. Ed.*, 59 (2020) 3592-3600.

[237] D.C.S. Calabro, NJ), Method of preparing silicoaluminophosphate compositions using a reagent containing both phosphorus and silicon reactive sites in the same molecule, in, Mobil Oil Corporation (Fairfax, VA), United States, 1994.

[238] M.D. Fokema, E. Chiu, J.Y. Ying, "Synthesis and Characterization of Nanocrystalline Yttrium Oxide Prepared with Tetraalkylammonium Hydroxides," *Langmuir*, 16 (2000) 3154-3159.

## Appendix A Supplementary Information for Chapter 2



**Figures A1.** Powder XRD pattern of ZSM-5 (MFI framework) synthesized in a fluoride medium.

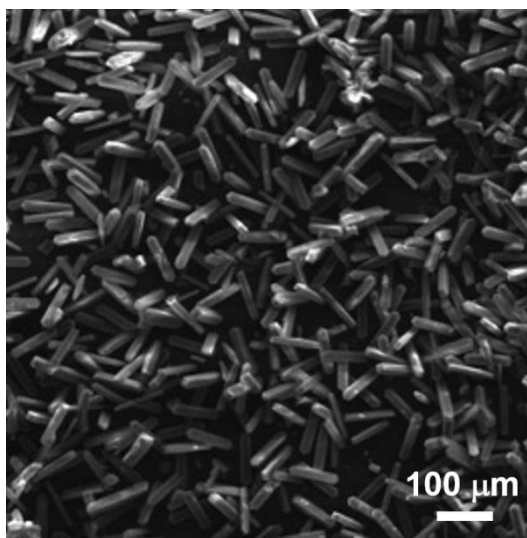


**Figure A2.** Scanning electron micrograph of representative ZSM-5 crystals synthesized in a fluoride medium.

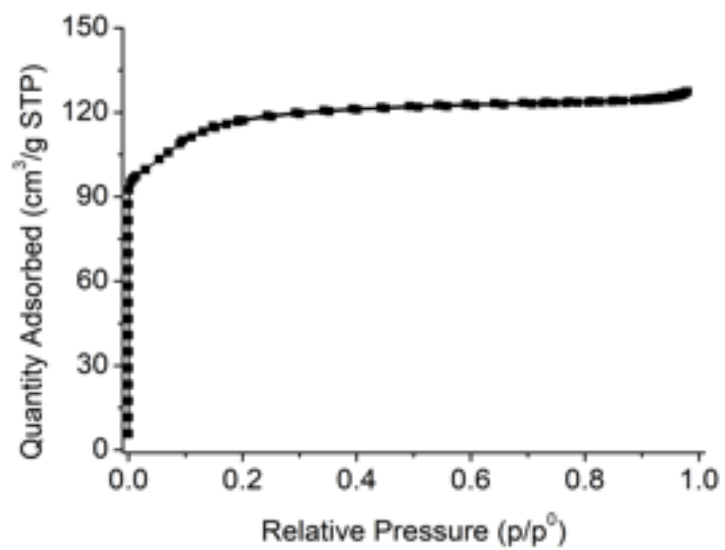


**Figure A3.** Nitrogen adsorption-desorption isotherm of ZSM-5.

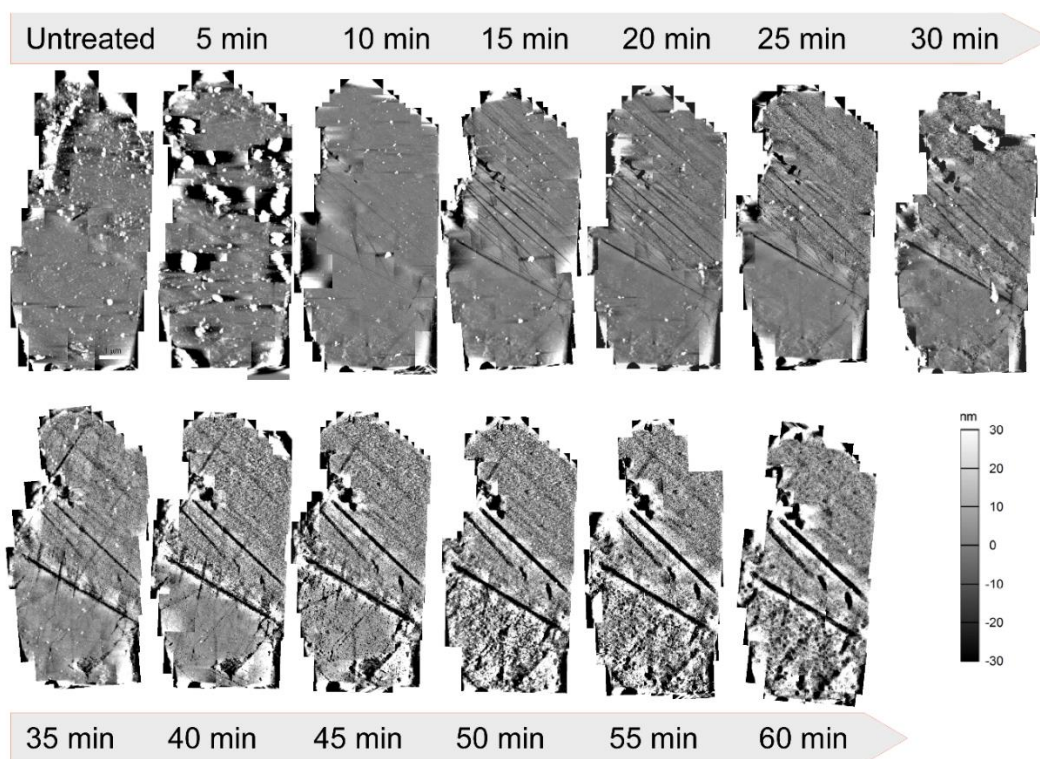


**Figure A4.** Merged AFM height images of a silicalite-1 sample treated *ex situ* in 40 wt%  $\text{NH}_4\text{F}$  solution for up to 60 min (shown here in 5 min intervals).

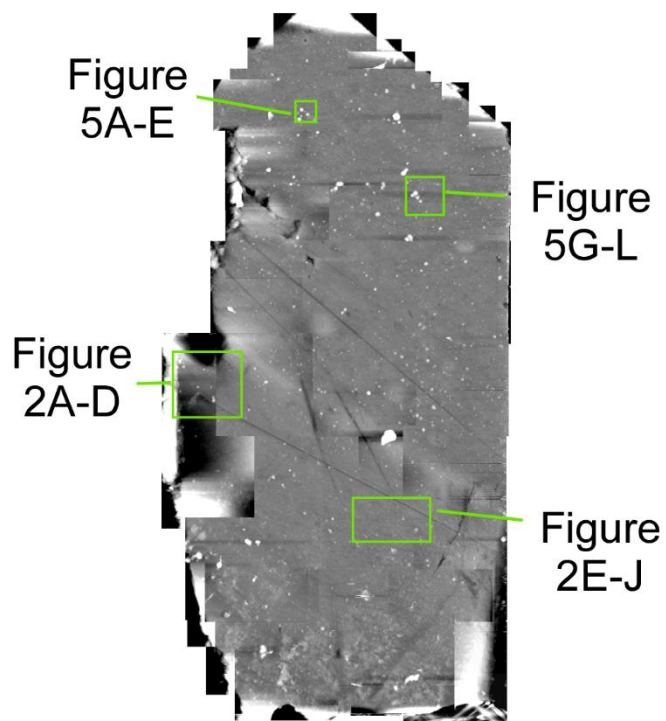


**Figure A5.** AFM height images of an MFI crystal after 10 min of treatment used as a template to mark areas of analyses of figures in the main text.

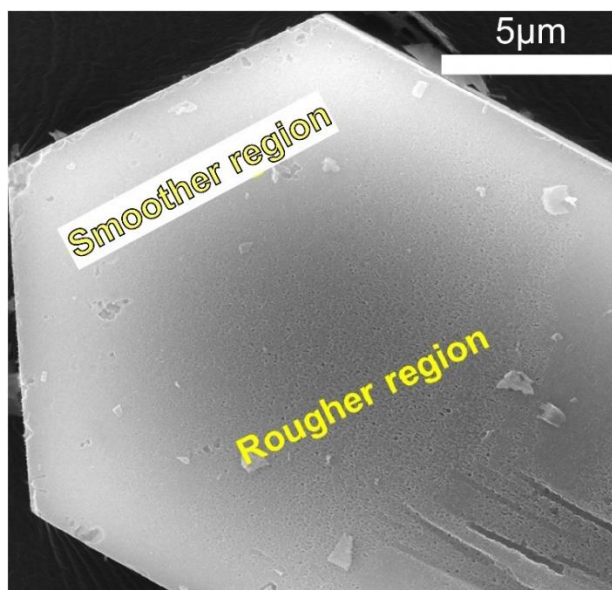


**Figure A6.** Scanning electron micrograph of a ZSM-5 crystal after  $\text{NH}_4\text{F}$  etching for 60 min.

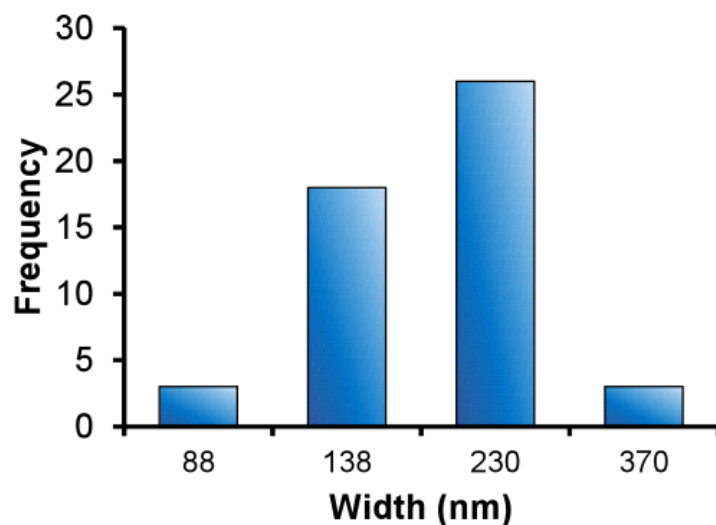


**Figure A7.** Histogram of measured widths of etch pits ( $n = 50$  measurements) over two different crystals. Widths listed in the  $x$ -axis are median values.

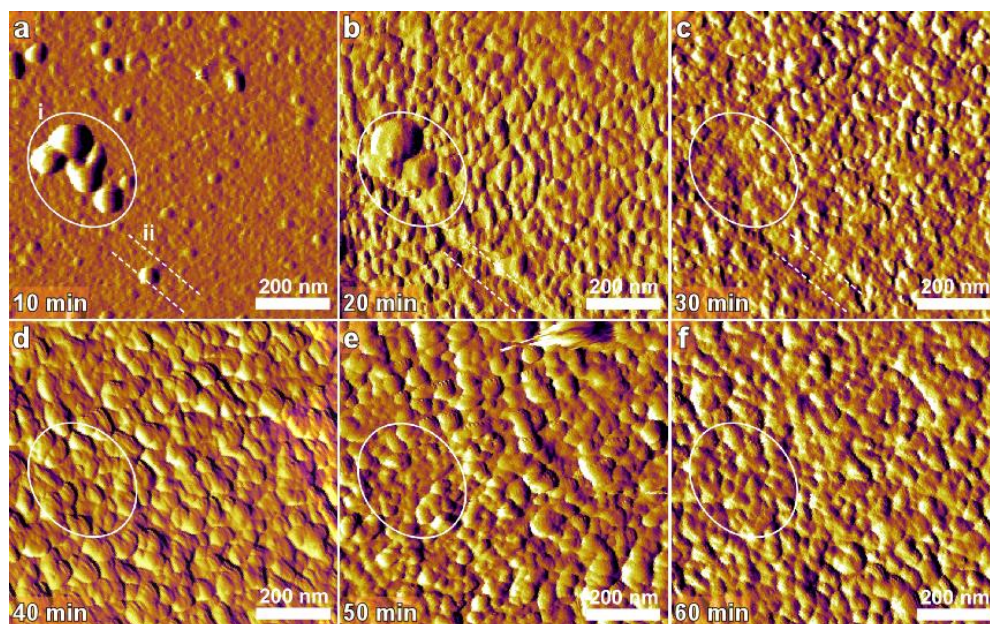


**Figure A8.** Corresponding amplitude images of Figure 5g-l in the main text. The circle (labelled  $i$ ) highlights a fixed area where the topography alternates. The dashed lines (labelled  $ii$ ) highlight a crevice.

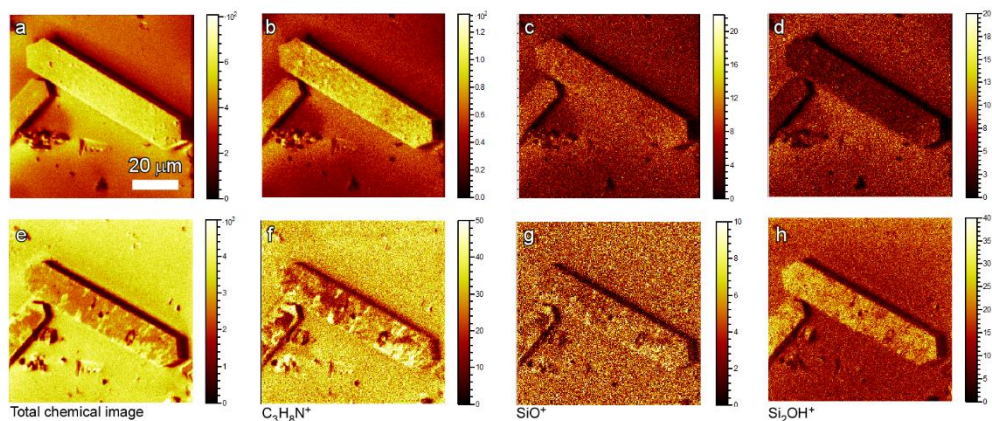


**Figure A9.** Chemical mapping of surface of two crystals from ToF-SIMS for parent MFI (a-d) and the acid-treated sample (e-h). Total chemical images (a and e), and mapping of (b and f)  $C_3H_8N^+$ , fragment of TPA ion, (c and g)  $SiO^+$ , (d-h)  $Si_2OH^+$ .

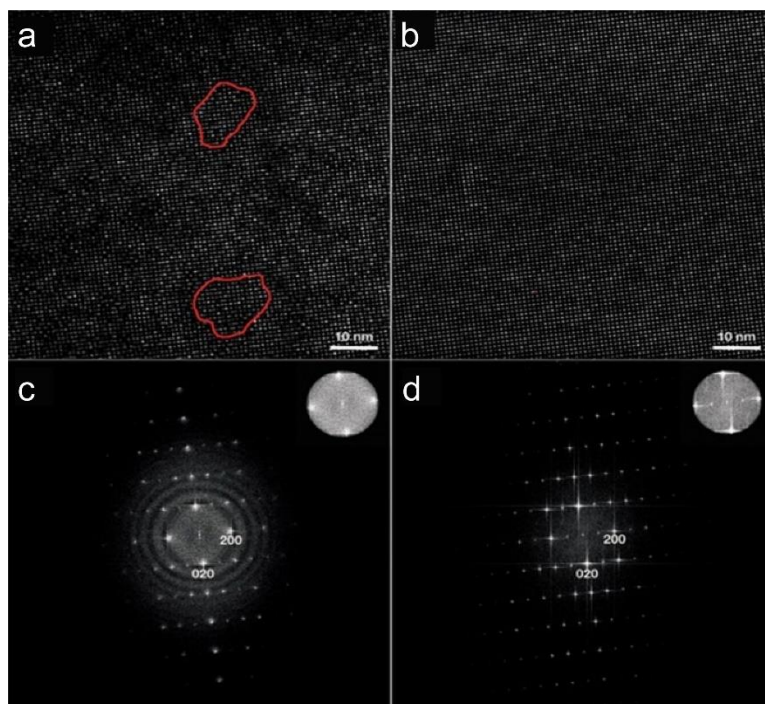
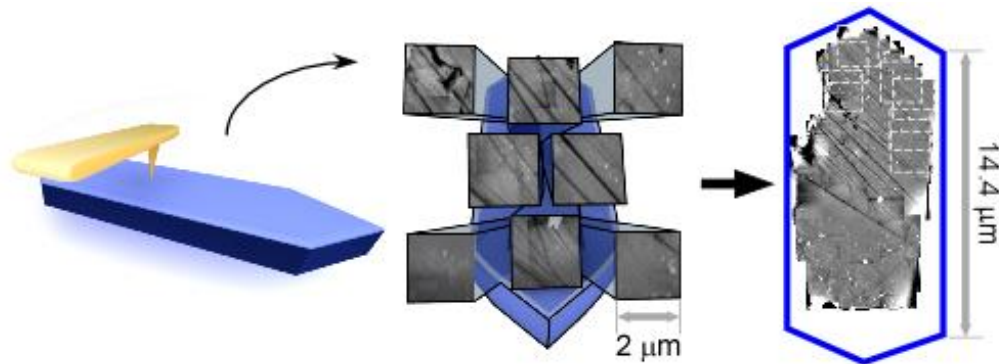
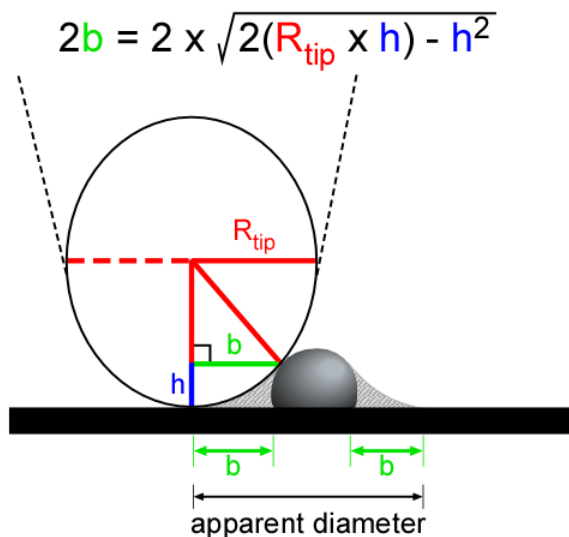


**Figure A10.** TEM imaging of a thin FIB lamellae cut of an untreated ZSM-5 crystal. (a) FI-FFT image from the [001] FFT pattern (c, central part), and (b) from the [001] FFT pattern image shown in d, peripheral part.



**Scheme A1.** (left) Atomic force microscopy (AFM) images of an entire MFI (010) crystal surface (ca. 14  $\mu\text{m}$  in length) compiled from the merging and overlapping of individual scans (size 2 x 2  $\mu\text{m}^2$ ).



**Scheme A2.** Scheme illustrating AFM tip geometry effect. The geometric factor is accounted for in diameter measurements of spheroidal features (**Figure 2.5f**). Adapted from [26].

## Appendix B Supplementary Information for Chapter 3

**Table B1.** Synthesis conditions and properties of ZSM-5 from an OSDA-based protocol.

Sample	Temp. (°C)	NaCl/Al <sub>2</sub> O <sub>3</sub>	KCl/Al <sub>2</sub> O <sub>3</sub>	M <sup>+</sup> / (TPA <sup>+</sup> +M <sup>+</sup> )	(Si/Al) <sub>bulk</sub> <sup>a</sup>	(Si/Al) <sub>surface</sub> <sup>b</sup>	Al <sub>surface</sub> /Al <sub>bulk</sub> <sup>c</sup>	Size (μm) <sup>d</sup>
ZH1	100	0	0	0.03	10.7 ± 1.4	10.4	0.97	0.9
ZA1	100	1.6	0	0.10	18.7 ± 0.4	11.6	1.57	1.0
ZA2	100	3.2	0	0.17	21.0 ± 0.1	12.4	1.64	1.2
ZA3	100	6.4	0	0.27	23.0 ± 0.4	13.1	1.70	1.1
ZA4	100	9.6	0	0.35	23.2 ± 1.0	9.7	2.26	0.9
ZA5	100	0	1.6	0.10	23.7 ± 3.1	13.4	1.71	1.0
ZA6	100	0	3.2	0.17	23.1 ± 3.5	11.5	1.93	1.0
ZA7	100	0	6.4	0.27	23.2 ± 0.2	8.6	2.52	1.2
ZA8	100	0	9.6	0.35	26.5 ± 2.3	9.5	2.63	1.1
ZS1	190	0	0	0.03	14.5 ± 0.7	20.7	0.71	8.0
ZS2	190	6.4	0	0.27	25.9 ± 1.9	48.2	0.55	2.5

<sup>a</sup> The (Si/Al)<sub>bulk</sub> values with two standard deviation errors from EDX measurements of different batches; <sup>b</sup> The (Si/Al)<sub>surface</sub> values are determined by XPS; <sup>c</sup> Ratio calculated from measured (Si/Al)<sub>bulk</sub> values and (Si/Al)<sub>surface</sub>; <sup>d</sup> The crystal size is measured by SEM and each value is the average of more than 50 crystals.

**Table B2.** Properties of ZSM-5 from an OSDA-free method where Na<sup>+</sup> is replaced with TPA<sup>+</sup>.

Sample	NaOH/Al	TPAOH/Al	(Si/Al) <sub>bulk</sub>	(Si/Al) <sub>surface</sub>	Al <sub>surface</sub> /Al <sub>bulk</sub>	Size (μm)
ZH2	9.6	0.0	17.5 ± 2.3	20.0	0.88	4 <sup>a</sup>
ZS3	7.5	2.1	14.9 ± 0.3	38.0	0.41	8
ZS4	5.3	4.3	20.6 ± 2.1	64.0	0.32	8
ZS5	3.2	6.4	29.1 ± 1.3	35.7	0.82	4.5
ZH3	1.0	8.6	26.2 ± 1.9	25.1	1.04	4

<sup>a</sup> Crystal thickness in b-direction is used to represent the size of faceted crystals for ZS-3, while the average particle size is used to present the size of spheroidal samples.

**Table B3.** Properties of ZSM-5 from an OSDA-free method where NaOH is replaced with TPAOH and amount of alkali metal is replenished with NaCl or KCl salt.

Sample	NaOH/Al	TPAOH/Al	NaCl <sup>a</sup> /Al	KCl <sup>a</sup> /Al	(Si/Al) <sub>bulk</sub>	(Si/Al) <sub>surface</sub>	Al <sub>surface</sub> /Al <sub>bulk</sub>	Size (μm)
ZS6	7.5	2.1	2.1	0.0	16.7 ± 1.9	53.0	0.33	7
ZS7	5.3	4.3	4.3	0.0	17.4 ± 1.3	62.8	0.29	5
ZS8	3.2	6.4	6.4	0.0	20.0 ± 1.0	70.8	0.25	4
ZS9	1.0	8.6	8.6	0.0	16.7 ± 0.5	76.5	0.28	3
ZS10	7.5	2.1	0.0	2.1	21.0 ± 1.6	61.4	0.35	13
ZS11	5.3	4.3	0.0	4.3	22.5 ± 3.1	48.7	0.41	12
ZS12	3.2	6.4	0.0	6.4	20.7 ± 0.6	80.1	0.26	6.5
ZS13	1.0	8.6	0.0	8.6	17.2 ± 0.8	47.3	0.46	11
ZS14 <sup>b</sup>	5.3	4.3	0.0	4.3	19.9 ± 0.5	61.9	0.27	3

<sup>a</sup> NaCl or KCl was added to keep total inorganic SDA content fixed; <sup>b</sup> ZS-14 was synthesized under rotation.

**Table B4.** Synthesis conditions and properties of selected ZSM-5 samples for catalysis study.

Sample	Temp. (°C)	NaCl/ Al <sub>2</sub> O <sub>3</sub>	KCl/ Al <sub>2</sub> O <sub>3</sub>			M <sup>+</sup> / (TPA <sup>+</sup> +M <sup>+</sup> )	(Si/Al) <sub>bulk</sub> <sup>b</sup>	(Si/Al) <sub>surface</sub> <sup>c</sup>	Al <sub>surface</sub> / Al <sub>bulk</sub> <sup>d</sup>	Size (μm) <sup>e</sup>
A-4	100	6.4	0			0.27	23.0 ± 0.4	13.1	1.70	1.1
		NaOH /Al	TPAOH/ Al	NaCl/ Al <sup>a</sup>	KCl /Al <sup>a</sup>					
H1-3	190	1.0	8.6	0	0	0.10	26.2 ± 1.9	25.1	1.04	4
H2-6	190	9.6	0.0	0	0	1	17.5 ± 2.3	20.0	0.88	4
S1-1 <sup>a,f</sup>	190	5.3	4.3	0.0	4.3	0.69	19.9 ± 0.5	61.9	0.27	3
S2-1	190	5.3	4.3	0	0	0.55	20.6 ± 2.1	64.0	0.32	8
S3-2	190	5.3	4.3	0.0	4.3	0.69	22.5 ± 3.1	48.7	0.41	12

<sup>a</sup> NaCl or KCl was added to keep total inorganic SDA content fixed; <sup>b</sup> The (Si/Al)<sub>bulk</sub> values with two standard deviation errors from EDX measurements of different batches; <sup>c</sup> The (Si/Al)<sub>surface</sub> values are determined by XPS; <sup>d</sup> Ratio calculated from measured (Si/Al)<sub>bulk</sub> values and (Si/Al)<sub>surface</sub>; <sup>e</sup> The crystal size is measured by SEM and each value is the average of more than 50 crystals. <sup>f</sup> S1-1 was synthesized under rotation.

**Table B5.** Summary of  $R^2/D$ , turnover numbers, and E/2MBu ratios.

Catalyst sample	$R_E^2/D$ (ks)	$R_E C_{H^+} S_A^{-1}$ ( $\mu\text{mol}/\text{nm}$ )	TON <sup>a</sup> (mol <sub>C</sub> /mol <sub>Brønsted</sub> )	E/2MBu <sup>c</sup>
A-4	2.06	$4.9 \times 10^{-15}$	3042, 3719 <sup>b,c</sup>	2.4, 2.6
H1-3	1.23	$4.0 \times 10^{-15}$	5518	3.4, 3.5
H2-6	5.81	$1.4 \times 10^{-14}$	3129	3.8, 4.0
S1-1	0.21	$1.8 \times 10^{-15}$	12769, 12820 <sup>c</sup>	2.0, 2.3
S2-1	0.26	$1.6 \times 10^{-15}$	22167	1.4, 1.7
S3-2	0.37	$2.5 \times 10^{-15}$	11694	2.1, 2.2
C-0.2	0.35	$8.9 \times 10^{-16}$	1944	3.6
CS-0.2	0.22	$5.6 \times 10^{-16}$	4117	3.2
ES-0.3	0.31	$5.1 \times 10^{-16}$	10109	2.6

<sup>a</sup> Calculate for  $\Delta(\text{conversion}) = 47\%$  starting from initial conversion

<sup>b</sup> Calculate with total acid site concentration measured by  $\text{NH}_3$ -TPD since pyridine-adsorbed spectrum from FTIR experiment is not quantifiable for A-4.

<sup>c</sup> Values from two separate runs of different sample batches

**Table B6.** Summary of local maxima (in wavenumbers) in each UV-vis spectral region for all samples. Specific association of species with wavelengths is summarized by Fu et al., [1].

Catalyst sample	HCP ( $\text{cm}^{-1}$ )	Internal coke ( $\text{cm}^{-1}$ )	External coke ( $\text{cm}^{-1}$ )
A-4	370	416	574
H1-3	361	422	560
H2-6	353	421	569
S1-1	356	415	569
S2-1	373	422	564
S3-2	364	421	571

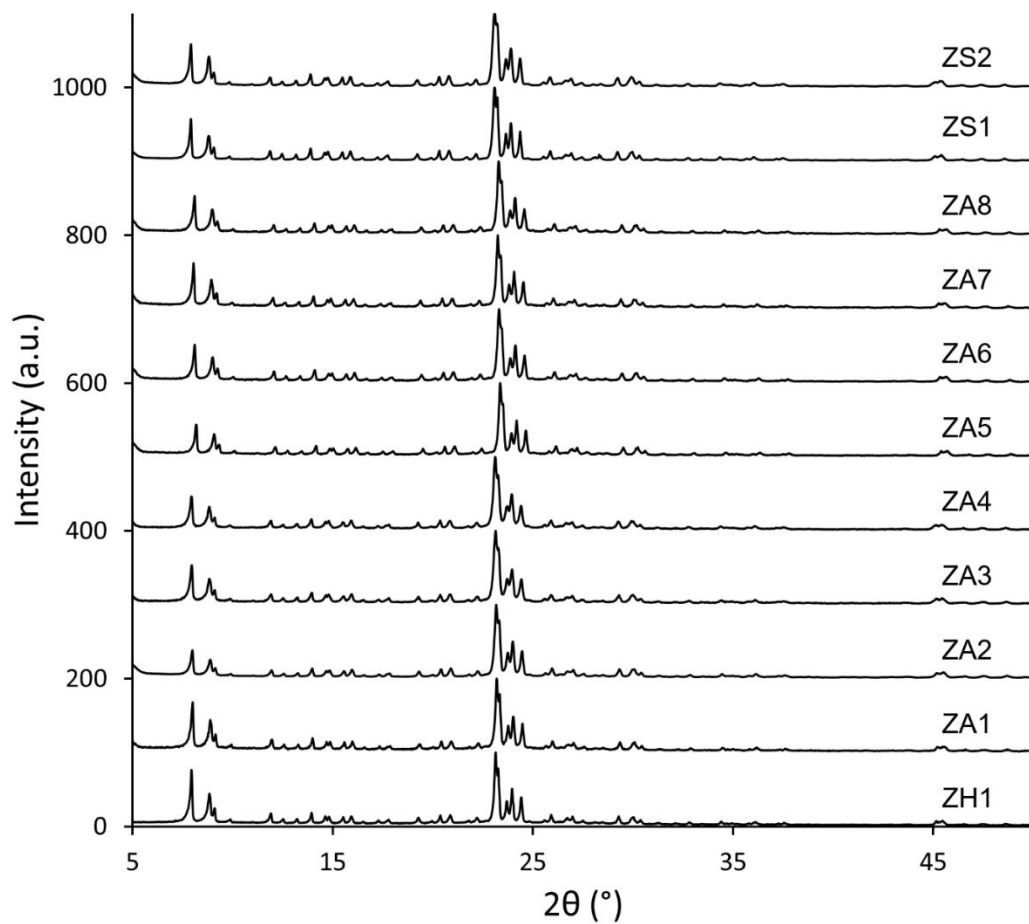


**Figure B1.** Powder XRD patterns for the set of samples shown in Table B1. The patterns for all samples display typical peaks indicative of the MFI framework.

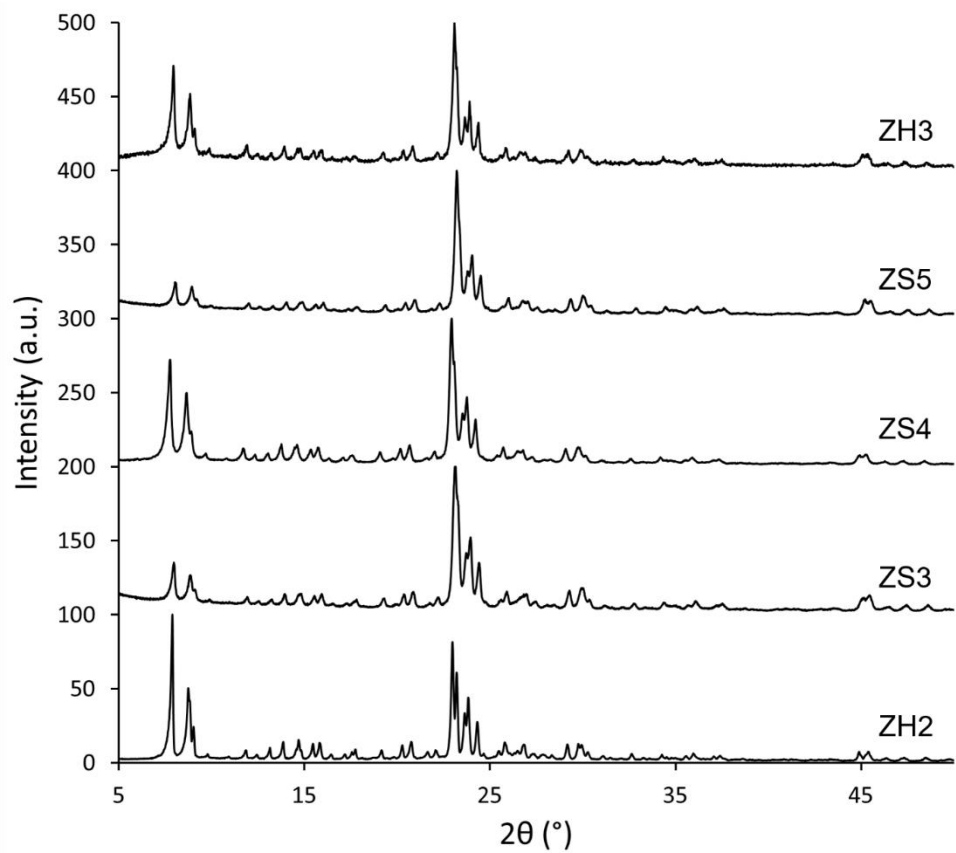


**Figure B2.** XRD patterns for the set of samples shown in Table B2. The patterns for all samples display typical peaks indicative of the MFI framework.

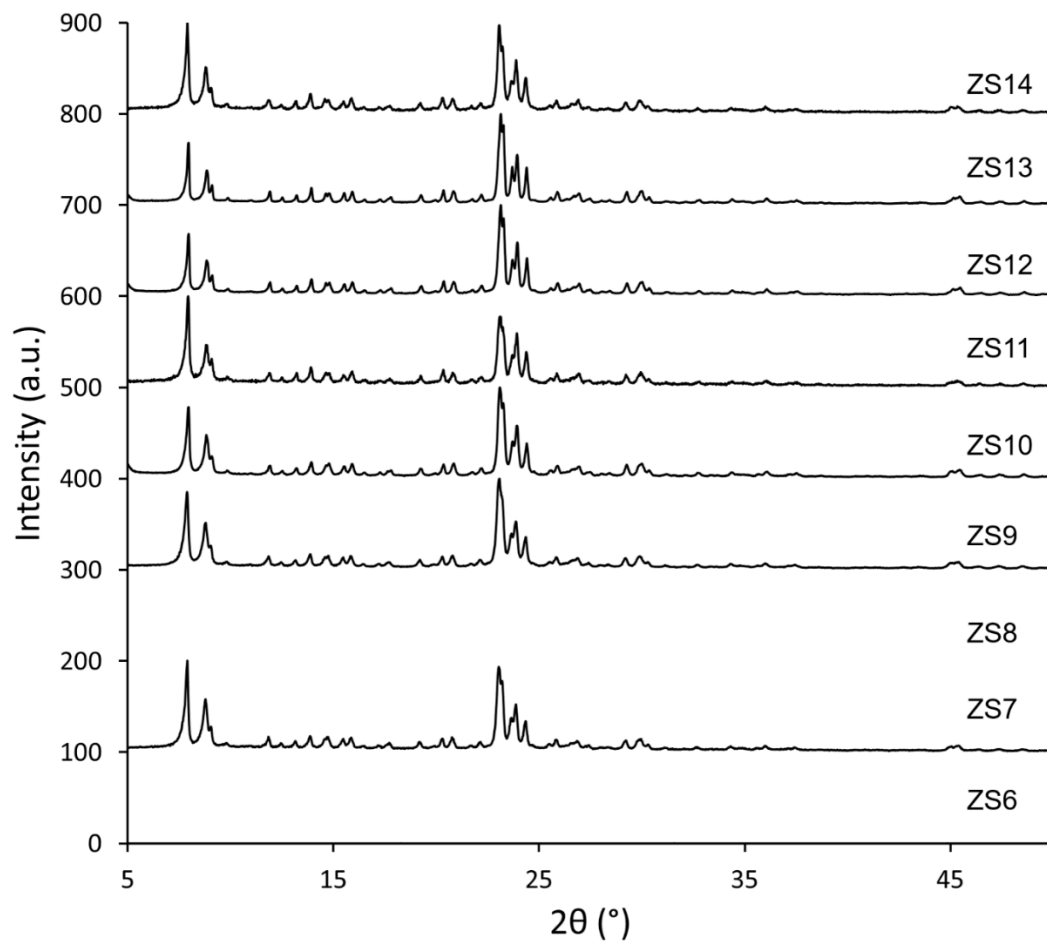


**Figure B3.** XRD patterns for the set of samples shown in Table B3. The patterns for all samples display typical peaks indicative of the MFI framework.

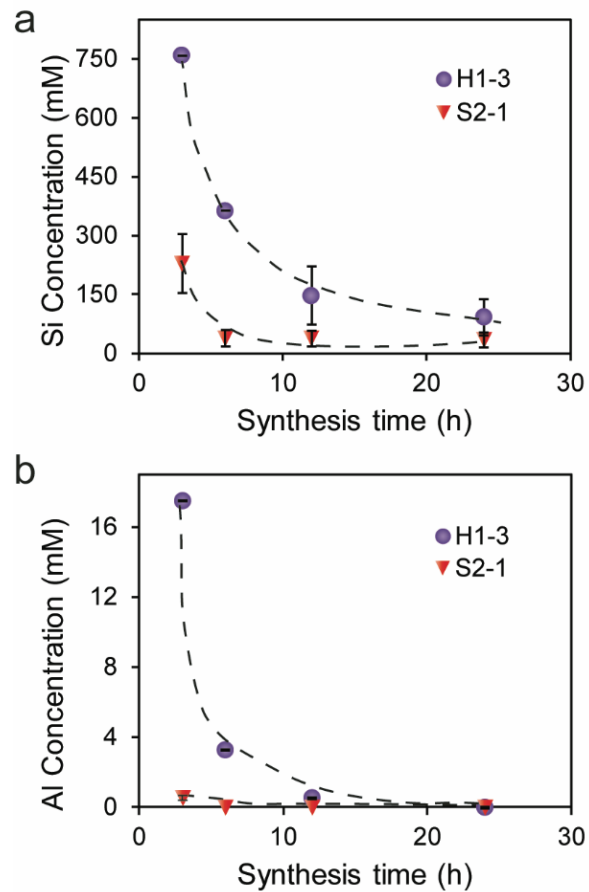


**Figure B4.** Si and Al concentration in the supernatant, analyzed with ICP-MS, as a function of time for homogeneous sample (H1-3, purple circles) and Si-zoned sample (S2-1, red inverted triangles). Error bars span two standard deviations.

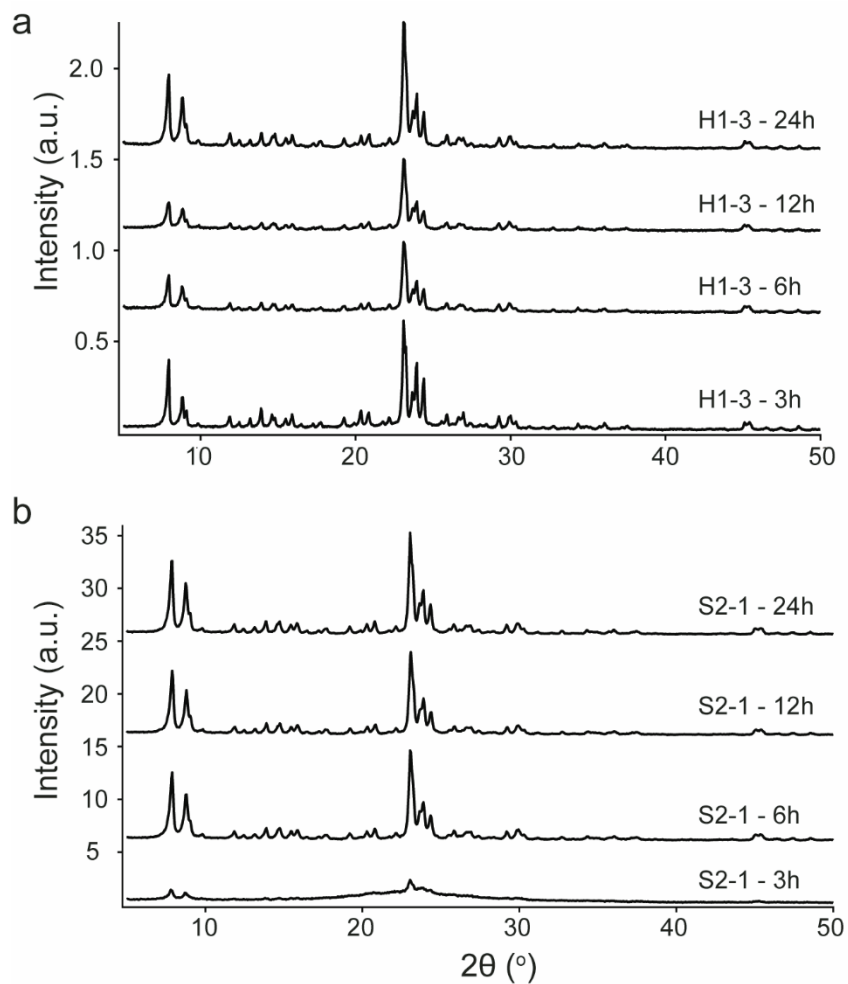


**Figure B5.** (a) XRD patterns of homogeneous sample synthesized with mixed SDAs (H1-3) and of (b) a Si-zone sample (S2-1) after 3, 6, 12, and 24 h of synthesis. The patterns display typical MFI peaks, except for S2-1 - 3h which shows partially amorphous phase.

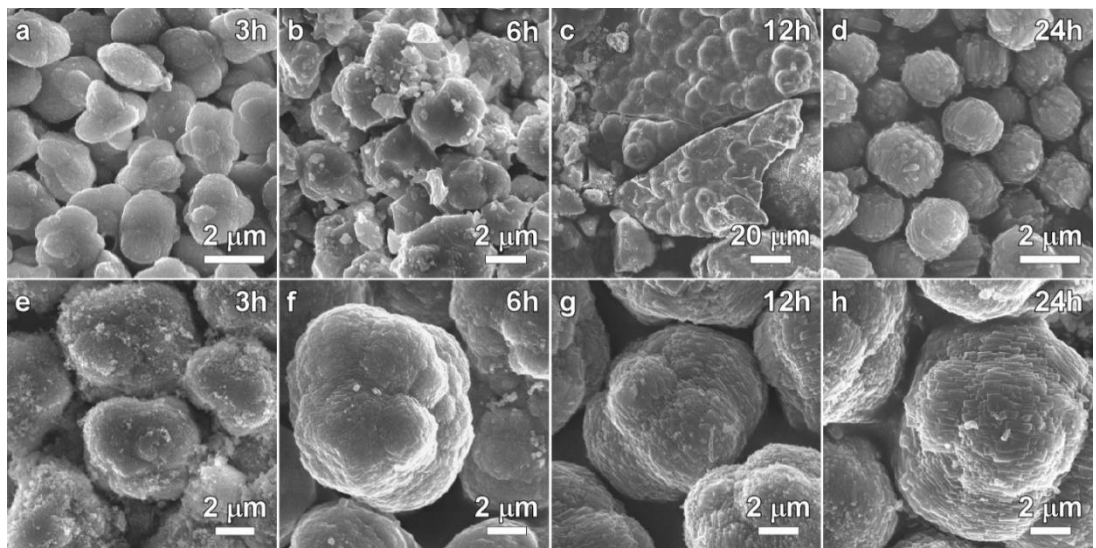


**Figure B6.** SEM micrographs of (a – d) homogeneous sample (H1-3) and (e – h) Si-zone sample (S2-1) collected from time-elapsd study after 3, 6, 12, and 24 h.

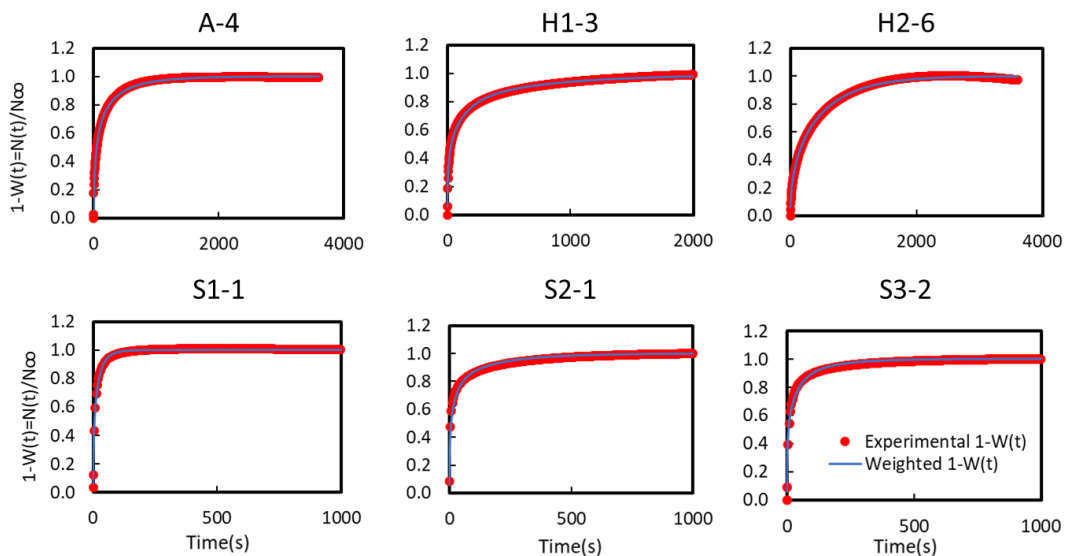


**Figure B7.** Results of transient sorption of 2,3-dimethylbutane, plotted as the normalized adsorption with respect to time. The experimental curves are shown with red circles, and the weighted curves are shown in blue.

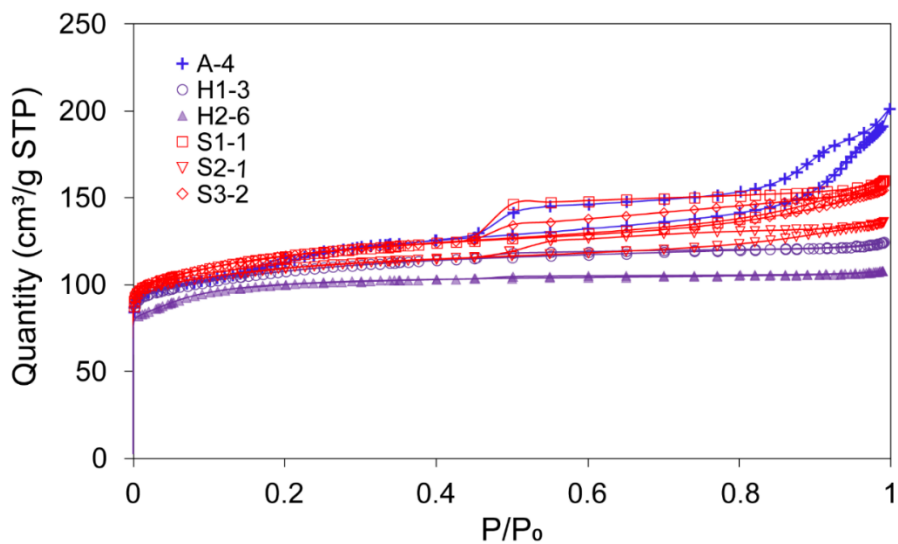


**Figure B8.** Physisorption curves plotted as quantity of  $N_2$  adsorbed/desorbed versus relative pressure for samples A-4 to S3-2 listed in Table 4.1.

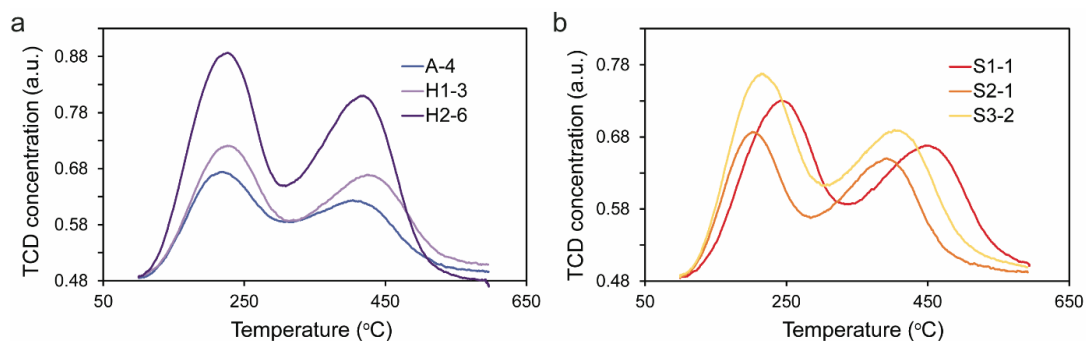


**Figure B9.**  $NH_3$  – TPD curves plotted as TCD concentration versus desorption temperature for (a) Al-zoned sample (blue), homogeneous sample from an inorganic synthesis (dark purple), and homogeneous sample from mixed SDAs (lavender); (b) Si-zoned samples.

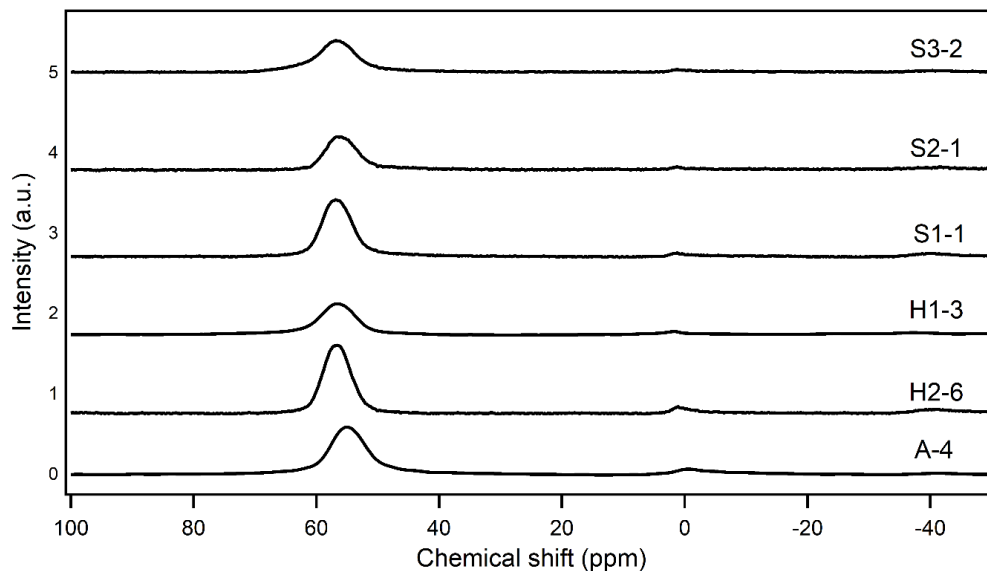


**Figure B10.**  $^{27}\text{Al}$  MAS NMR spectra for H-ZSM-5 catalyst samples with Al-zoning (A-4), Si-zoning (S1-1, S2-1, and S3-2), and homogeneous Al distribution (H1-3, H2-6).

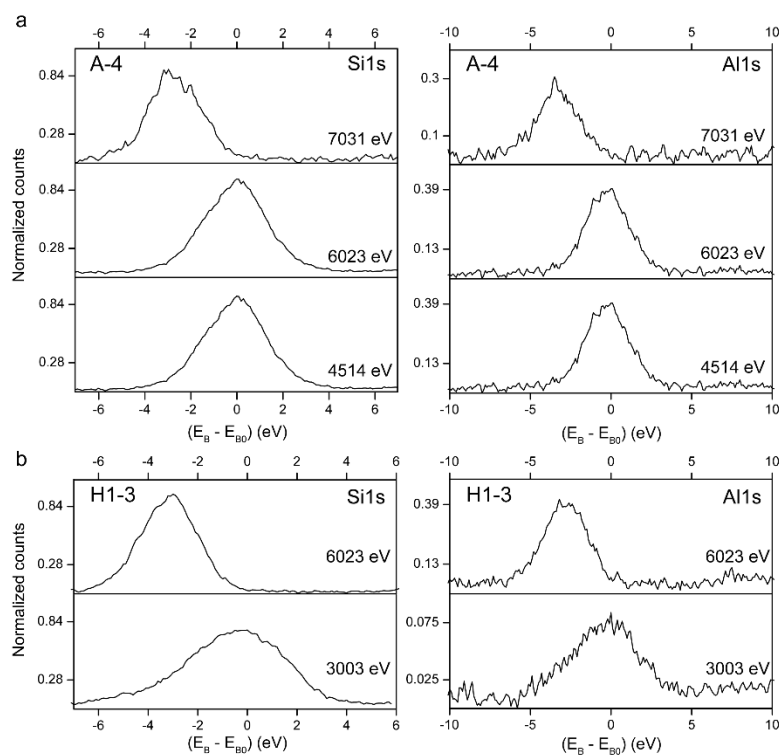


**Figure B11.** Raw VKE-XPS spectra for (a) sample A-4 and (b) H1-3. The binding energy ( $E_B$ , x-axis) is plotted relative to the binding energy of spectra collected at a photon energy of 3003 eV.

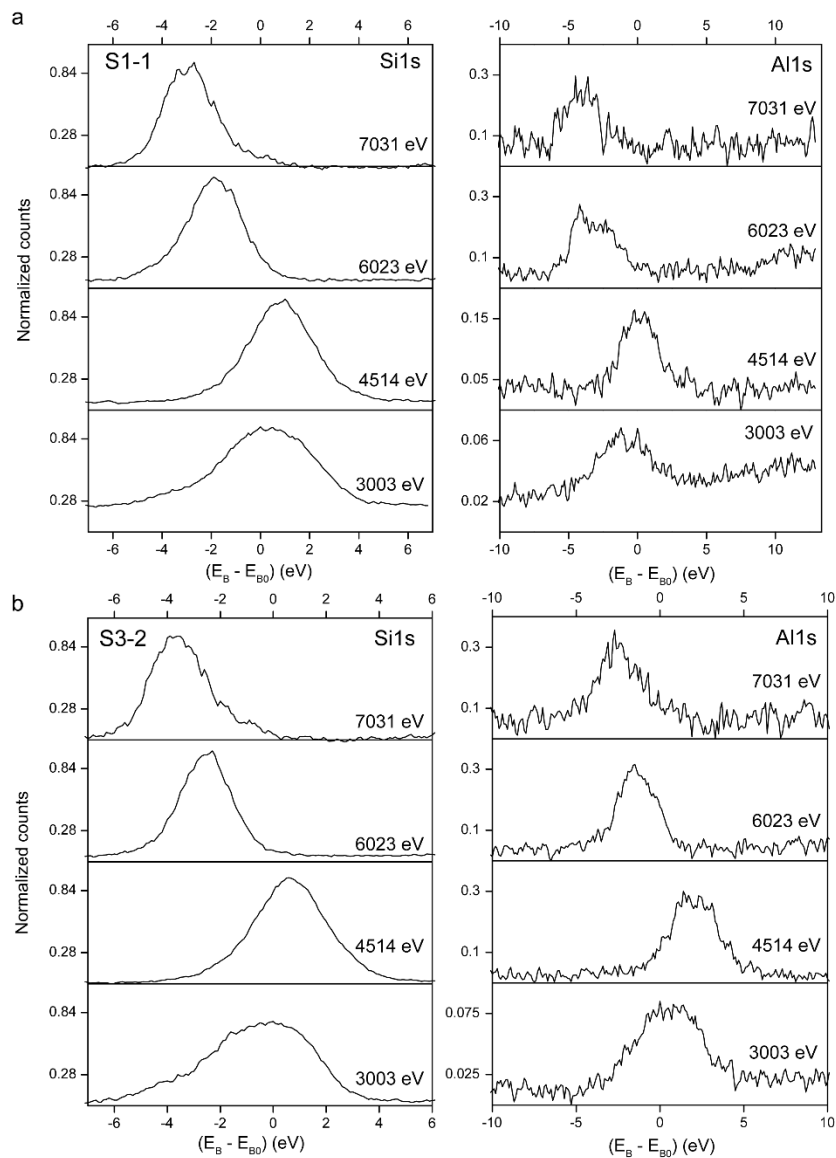


**Figure B12.** Raw VKE-XPS spectra for (a) sample S1-1, (b) sample S3-2. The binding energy ( $E_B$ , x-axis) is plotted relative to the binding energy of spectra collected at a photon energy of 3003 eV.

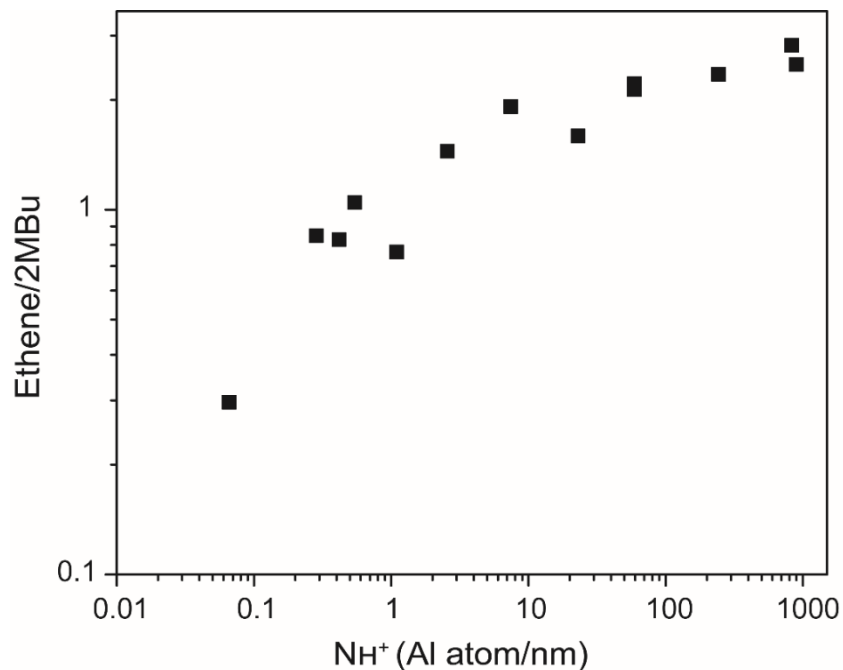


**Figure B13.** Ethene-to-2MBu selectivity ratio as a function of a descriptor ( $N_{H^+}$ ). The digitizer tool in OriginLab was used to extract ethene and 2MBu selectivities from Figure S4a of Khare et al., [27].

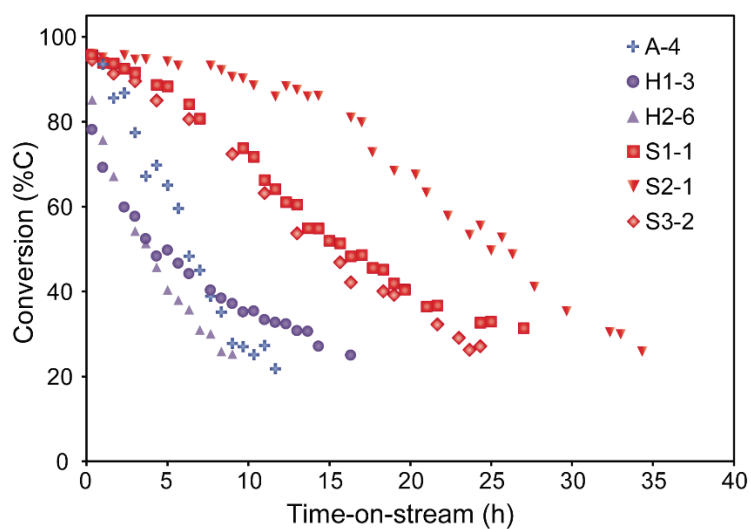


**Figure B14.** Conversion of MeOH and DME as a function of TOS for the Al-zoned (blue), homogeneous (purple), and Si-zoned samples (red). All reactions were performed at 350 °C using a space velocity of 0.18 - 0.30 mol MeOH mol<sup>-1</sup> H<sup>+</sup> s<sup>-1</sup>.

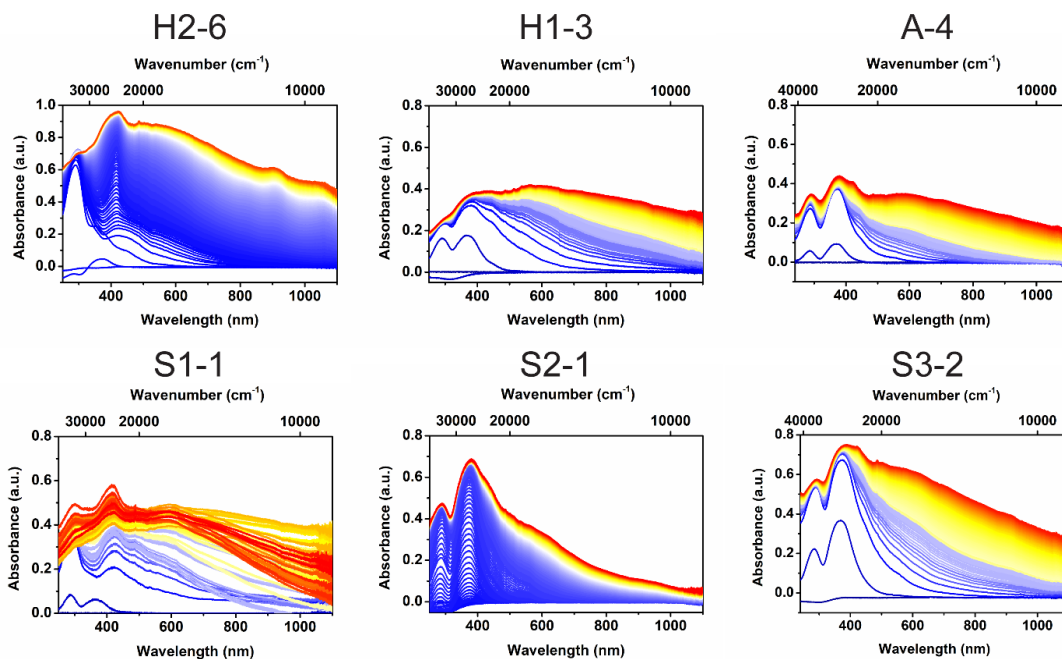


**Figure B15.** UV-vis spectra collected under operando condition for methanol-to-hydrocarbon reaction.

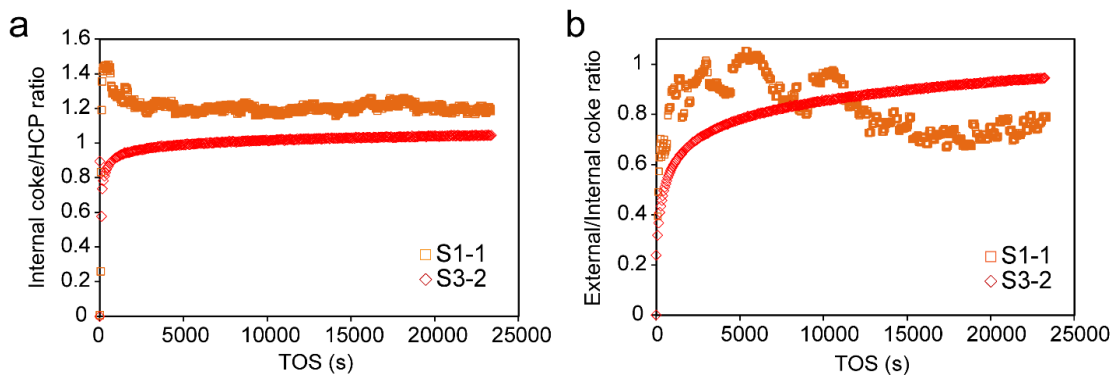


**Figure B16.** (a) Temporal changes of the intensity ratio of internal coke species (416-425 nm) to HP species 350-375 nm for Si-zoned sample S3-2. (b) Corresponding changes of the intensity ratio of external coke species (560-575 nm) to internal coke species.

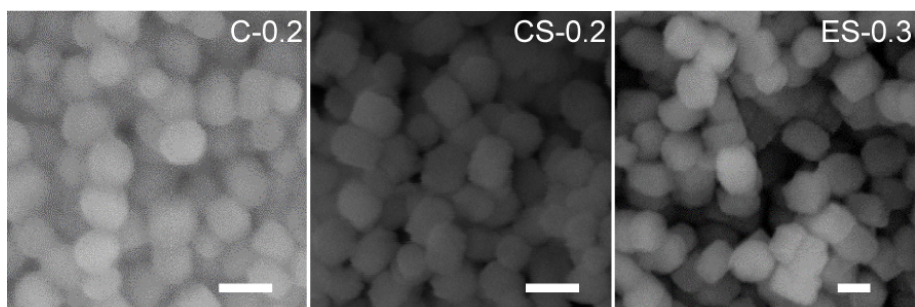


**Figure B17.** SEM images of the homogeneous ZSM-5 core (C-0.2), ZSM-5@silicalite-1 core-shell (CS-0.2), and inverse core-shell silicalite-1@ZSM-5 (ES-0.3) samples.

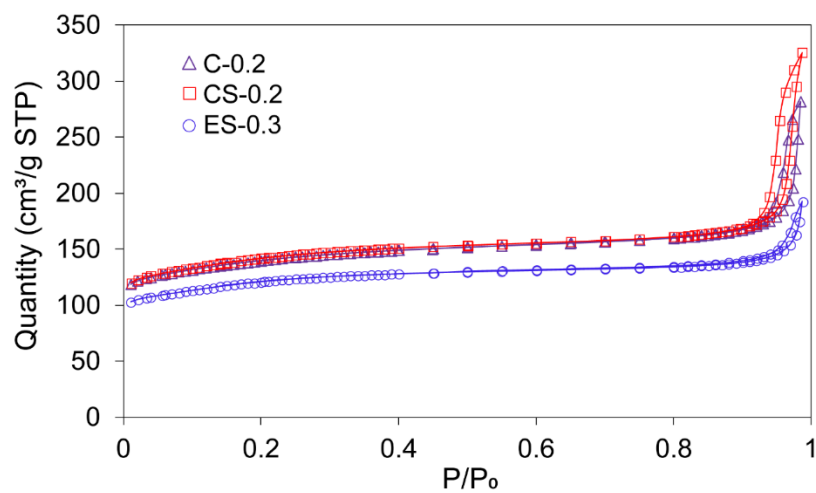


**Figure B18.** Physisorption curves plotted as quantity of N<sub>2</sub> adsorbed/desorbed versus relative pressure for samples C-0.2, CS-0.2, and ES-0.3 listed in Table 3.1 of the manuscript.

## Appendix C Supplementary Information for Chapter 4

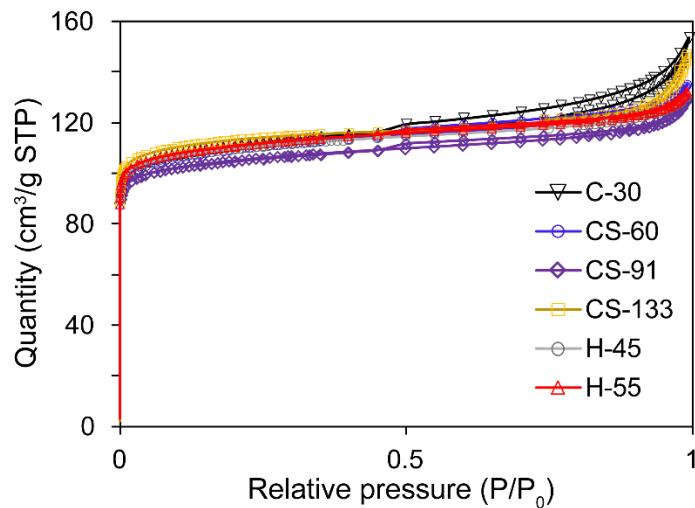


**Figure C1.** Physisorption curves plotted as quantity of N<sub>2</sub> adsorbed/desorbed versus relative pressure for all samples listed in Table 4.1.

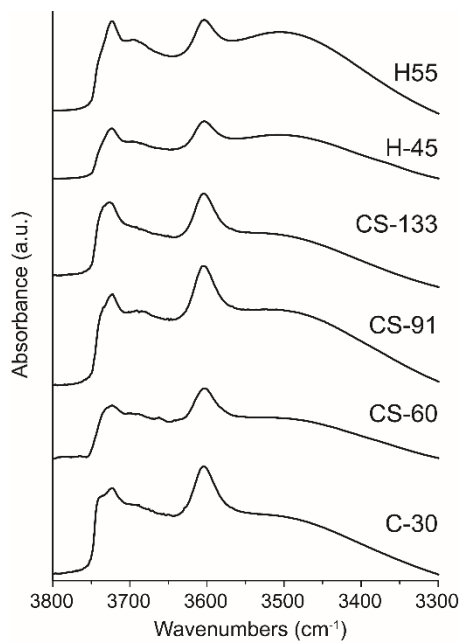


**Figure C2.** Spectra in the range of 3800-3300 cm<sup>-1</sup> for H-form samples before pyridine adsorption.

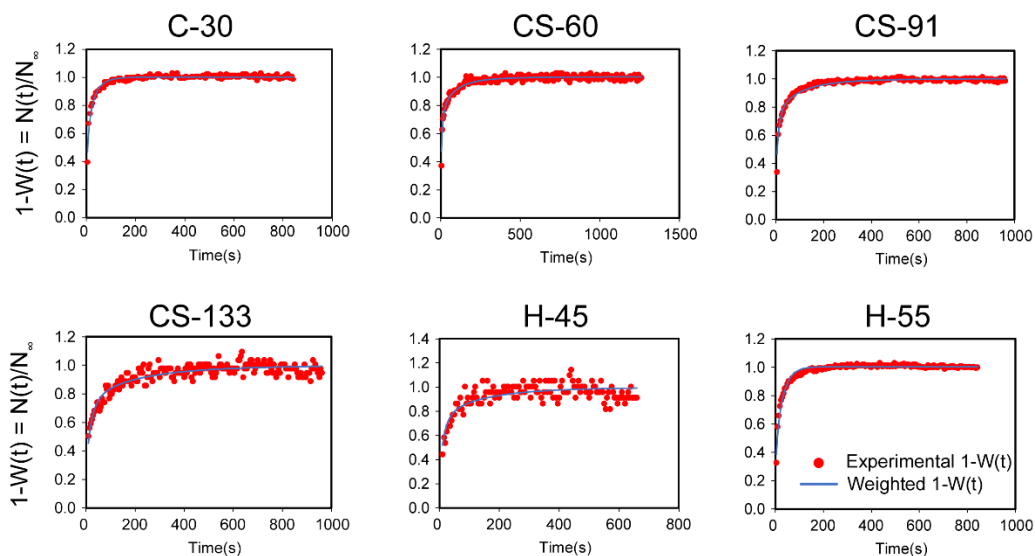


**Figure C3.** Results of transient sorption of 2,3-dimethylbutane, plotted as the normalized adsorption with respect to time. The experimental curves are shown with red circles, and the fitted curves are shown in blue.

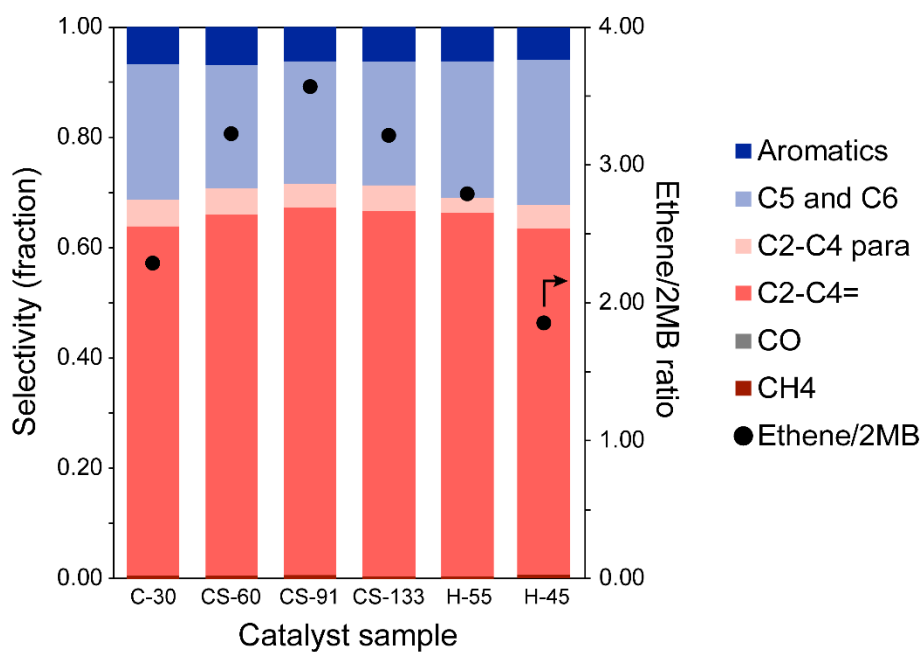


**Figure C4.** Initial effluent hydrocarbon selectivity (left axis) and ethene/2MBu (black circles, right axis) at iso-conversion (39-61%) for methanol-to-hydrocarbons reactions over H-ZSM-11 catalysts at 350 °C and  $P_{\text{MeOH}} = 11.5$  kPa.